Summer 8-8-2019

Measurements of N_2O and SF_6 Mole Fraction and N_2O Isotopic Composition between 1978 and 1997 in Archived Air Samples from Cape Meares, Oregon

Terry Clinton Rolfe
Portland State University

Measurements of N_2O and SF_6 Mole Fraction and N_2O Isotopic Composition between 1978 and 1997 in Archived Air Samples from Cape Meares, Oregon

by

Terry Clinton Rolfe

A dissertation submitted in partial fulfillment of the
requirements for the degree of

Doctor of Philosophy
in
Applied Physics

Dissertation Committee:
Andrew L. Rice, Chair
Christopher L. Butenhoff
M. Aslam. K. Khalil
Jennifer L. Morse

Portland State University
2019

Abstract

Nitrous oxide (N_2O) is the third most important greenhouse gas (GHG) behind carbon dioxide (CO_2) and methane (CH_4). Sulfur hexafluoride (SF_6) does not add significantly to climate forcing by itself due to the low concentration in the atmosphere; however, it is one of the most powerful GHG known. Measurements of atmospheric N_2O made prior to mid-1990 have larger uncertainties than later periods due to advancements made in gas chromatography (GC) methods. Few atmospheric SF_6 measurements pre-1990 exist, especially in the northern hemisphere. Archived samples may be analyzed using updated measurement techniques to reduce uncertainty in past periods. Additionally, measurements of the isotopic composition of N_2O ($^{15}N/^{14}N$ and $^{18}O/^{16}O$) can address questions regarding how specific sources contribute to the observed atmospheric composition and changes in time. This information also has been used to identify changing contributions of nitrification versus denitrification processes to the global N_2O budget, determined by the rate of change in the site preference (SP, defined as $\delta^{15}N^{\alpha} - \delta^{15}N^{\beta}$) of ^{15}N. Here, we present the findings of 159 measurements of N_2O and SF_6 mixing ratio and N_2O isotopic composition from the OHSU-PSU air archive, containing samples collected from Cape Meares, Oregon between 1978 and 1997.

Based on these analyses, N_2O mole fraction at Cape Meares in 1980 is found to be 301.5 ppb and rises to 313.5 ppb in 1996. The average growth rate over this period is 0.78 ± 0.03 ppb yr^{-1} (95% CI). Seasonal amplitude maximum and minimum is 0.34 ppb near April and -0.42 ppb near November respectively and are statistically different from one another ($p<0.005$). Measurements of N_2O were found to match well with previously

reported values for Cape Meares from AGAGE and other comparable locations, suggesting that the N_2O in archived samples has stored well.

For SF_6, the mole fraction in 1980 was found to be 1.06 ± 0.05 ppt and increased to 3.91 ± 0.07 ppt in 1996. The average growth rate over this period is 0.17 ± 0.01 ppt yr^{-1} (95% CI). Seasonality shows peak amplitude of 0.04 ppb near January and minimum amplitude of -0.03 ppt near July. There are no previous reported measurements of SF_6 from Cape Meares to compare against directly; however, comparisons against archive measurements from Cape Grim, Tasmania suggest these results are accurate.

Isotopic composition measurements of N_2O are made by cryogenically concentrating N_2O before analysis using an isotope ratio mass spectrometer operated in continuous flow (CF-IRMS). From replicate analysis of the working standard, precision in measurement of the measured isotopologues is 0.05‰, 0.10‰, and 0.28‰ for δ^{45}, δ^{46}, and δ^{31}, respectively. When calculating the desired isotopic composition, these translate to 0.05‰, 0.10‰, 0.37‰ and 0.39‰ for $\delta^{15}N_{bulk}$, $\delta^{18}O$, $\delta^{15}N^{\alpha}$, and $\delta^{15}N^{\beta}$, respectively.

For archived samples from Cape Meares, no distinguishable seasonality is found in $\delta^{15}N$ or $\delta^{18}O$ while $\delta^{15}N^{\alpha}$, $\delta^{15}N^{\beta}$, and SP show statistically significant amplitudes. $\delta^{15}N^{\alpha}$ and $\delta^{15}N^{\beta}$ show nearly opposite phases to one another, with SP matching the phase of $\delta^{15}N^{\alpha}$. These results suggest processes that contribute air enriched in N_2O mole fraction at Cape Meares in the spring also contribute enriched $\delta^{15}N^{\alpha}$ and depleted $\delta^{15}N^{\beta}$, causing a positive SP. During the fall, processes that contribute air depleted in N_2O mole fraction also contribute depleted $\delta^{15}N^{\alpha}$ and enriched $\delta^{15}N^{\beta}$, causing a negative SP.

Secular trends (except $\delta^{15}N^{\beta}$) calculated by applying a linear fit to the deseasonalized data show negative trends statistically significant at high levels of

confidence. Secular trends for $\delta^{15}N$ and $\delta^{18}O$ match well with previously reported values while secular trends for $\delta^{15}N^{\alpha}$ and $\delta^{15}N^{\beta}$ for Cape Meares are significantly different than those reported by other groups, appearing to be nearly inverted for $\delta^{15}N^{\alpha}$ and $\delta^{15}N^{\beta}$. To address this inversion, the sensitivity of the numerically calculated $\delta^{15}N^{\alpha}$ and $\delta^{15}N^{\beta}$ on the scrambling coefficient was investigated and ruled out. We also investigated the possibility of an error in the numerical algorithm used to convert measured ^{45}R, ^{46}R, and ^{31}R values into $\delta^{15}N$, $\delta^{18}O$, $\delta^{15}N^{\alpha}$, $\delta^{15}N^{\beta}$ and found this too was not responsible for the inverted results.

A 2-box model of the atmosphere was used to investigate changes in measured atmospheric composition to characterize source isotopic composition. From the results of the box model, the magnitude of the pre-industrial natural source match well with previous literature. The isotopic compositions of the natural source match well with previously reported values, as do the modeled anthropogenic $\delta^{15}N$, $\delta^{18}O$, and $\delta^{15}N^{\alpha}$. However, our modeled $\delta^{15}N^{\beta}$ is significantly enriched compared with previously reported values. Additionally, the modeled anthropogenic SP is significantly depleted than previously reported values. Assuming the laboratory measurements of intramolecular SP are globally relevant, these results suggest there have not been significant changes to the balance between contributions from nitrification and denitrification to the observed isotopic composition of N_2O during this period (1978 – 1996). However, a more sophisticated model maybe needed to investigate this hypothesis.

Dedication

For my family, friends, and loving husband

Acknowledgements

I am fortunate to have the opportunity in my life to pursue a career in a field that I am passionate about and is intellectually stimulating. My academic pursuits have been challenging and time consuming, but I cannot image my life any other way. None of this would be possible without the help and guidance of many people. Thank you to all of my mentors who have provided counseling with patience, no one more than Andrew Rice, who has been with me every step since coming to PSU. Thank you to my family and friends for their unending support. To my mom and dad for never saying no to my dreams, to my sister for challenging me and keeping me competitive, and of course, my adoring husband, who has been patiently waiting for me to finish this degree since we met…

Table of Contents

List of Tables

List of Figures

Chapter 1

Introduction

1.1 Long-lived greenhouse gases

Anthropogenic sources of greenhouse gases (GHG) have greatly increased the burden of these gases in the Earth's atmosphere and continue to increase the observed climate forcing. Nitrous oxide (N_2O) is the third most important greenhouse gas behind carbon dioxide (CO_2) and methane (CH_4). From measurements of ice core air, the pre-industrial concentration of N_2O was near 270 ppb (Khalil and Rasmussen, 1988; MacFarling Meure et al. 2006). Today the concentration of N_2O is close to 330 ppb with an increasing trend of ~0.75 ppb/year over the last 30 years (Prinn et al. 2000; Ciais et al. 2013). N_2O has a large global warming potential of 298 times that of CO_2 over a 100 year period and a global radiative forcing value estimated to be 0.17 Wm^{-2} (Myhre et al. 2013). The lifetime of N_2O is estimated to be between 118 and 132 years (Ciais et al. 2013). This means that most of it will reach the stratosphere where photooxidation of N_2O is the major source of stratospheric NO_X ("active nitrogen"), the main natural catalyst of ozone (O_3) destruction (Crutzen 1970).

Table 1.1. Concentration and radiative forcing since 1750 of CO_2, CH_4, N_2O, and SF_6 (Myhre et al. 2013).

	Concentration		**Radiative forcing (Wm^{-2})**	
Species	*2011*	*2005*	*2011*	*2005*
CO_2 (ppm)	391±0.2	379	1.82±0.19	1.66
CH_4 (ppb)	1803±2	1774	0.48±0.05	0.47
N_2O (ppb)	324±0.1	319	0.17±0.03	0.16
SF_6 (ppt)	7.28±0.03	5.64	0.0041	0.0032

N_2O is produced by natural and anthropogenic sources, mostly through microbial nitrification and denitrification processes. The imbalance between the sources and the sinks of N_2O is mostly due to the increased fertilizer use in crop production (Kroeze et al. 1999; Park et al. 2012). Models project that future climate change will amplify N_2O production, meaning a linear extrapolation of the current rate of change may under-project future concentrations (Khalil and Rasmussen 1983; Stocker et al. 2013). Therefore, to minimize uncertainty in model projections, many precise measurements of current and past atmospheric conditions from multiple locations around the globe are needed. Measurements of atmospheric N_2O made prior to mid-1990 have larger uncertainties than later periods due to advancements made in gas chromatography (GC) methods (Prinn et al. 2000; Jiang et al. 2007).

1.2 N_2O Global budget

Defining the global budget for N_2O is a challenging task. Methods used to calculate the global budget can be described as "top-down" or "bottom-up" methods. Top-down methods involve observations of atmospheric N_2O concentrations, then using the observations to constrain model source emissions. The bottom-up method quantifies N_2O sources through measurements at the source, then calculates the global emissions and concentrations by scaling up through modeling. Using either method, large errors can occur when calculating the size of the sources or sinks due to the challenge of quantifying their effects. The strongest constraint on the total source magnitude is based on observed annual trends and model calculations of N_2O lifetime (Prather et al. 2012). A N_2O budget

calculated by combining bottom-up scaling with top down constraints provides the most complete picture of the true global budget (Ciais et al. 2013).

One estimate for the total contribution from natural and anthropogenic sources as well as the size of the sink was calculated by Prather et al. (2012) using the top-down method with bottom-up scaling, shown in figure 1.1. For the year 2011, the natural sources of N_2O make up more than 60% of all N_2O sources, estimated at 9.1 ± 1.0 TgN (N_2O) yr^{-1} while the anthropogenic source is 6.7 ± 1.0 TgN (N_2O) yr^{-1}. The atmospheric sink is estimated to be 11.9 ± 0.9 TgN (N_2O) yr^{-1}. This estimate provides relatively tight constraints around the magnitude of the total sources and sink, but does not break down individual source contributions to the whole.

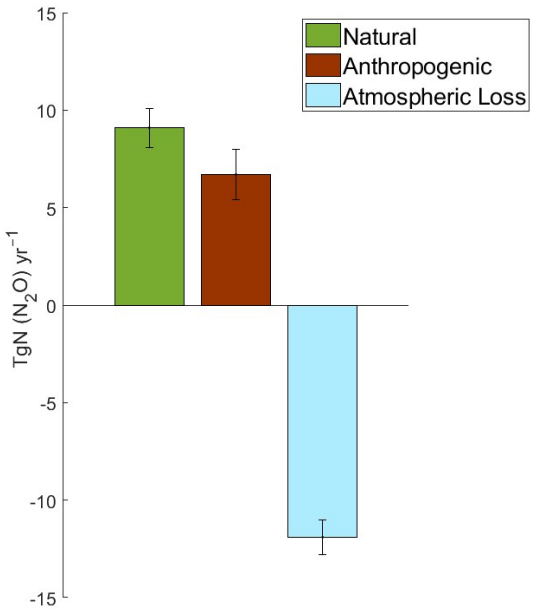

Figure 1.1. Natural, anthropogenic, and atmospheric loss of N_2O in TgN (N_2O) yr^{-1} in 2011 (Prather et al. 2012; Ciais et al. 2013). Error bars are 68% CI.

1.2.1 N_2O Sources

The magnitudes of anthropogenic and natural sources of N_2O depend on the amount of biologically available N to microbes. This is because most N_2O is produced microbially through nitrification and denitrification processes. Nitrification is the main source of N_2O under aerobic conditions where ammonium (NH_4^+) is oxidized into nitrate (NO_3^-) and produces N_2O as a by-product in the process. Denitrification reduces nitrate into nitrogen gas (N_2) and dominates under anoxic conditions, producing N_2O as an intermediate in the process. These biologically controlled production processes are dependent on factors such as oxygen concentration, temperature, N substrate availability, gas transport, soil type, soil texture, and water content (Perez et al. 2001; Goldberg et al. 2008; Park et al. 2011). These factors result in large uncertainties when calculating the magnitude of an individual source. Biological nitrogen fixation, the conversion of N_2 to ammonia (NH_3), also plays an important role in the production of N_2O for both anthropogenic and natural sources (Galloway et al. 1995). N fertilizer is produced by industrial N fixation, utilizing the Haber-Bosch process to convert unreactive N_2 to NH_3. This increases the biologically available N for microbial nitrification and denitrification and is the main contribution to anthropogenic N_2O production.

The largest natural source of N_2O is soils, producing 6.6 (3.3-9) TgN (N_2O) yr^{-1}. Natural soil production of N_2O is governed by biological nitrogen fixation, nitrification, and denitrification processes. Soils with higher nitrogen content, water content, and temperatures such as tropical soils or riparian zones are the largest contributors to natural soil N_2O production (Ciais et al. 2013).

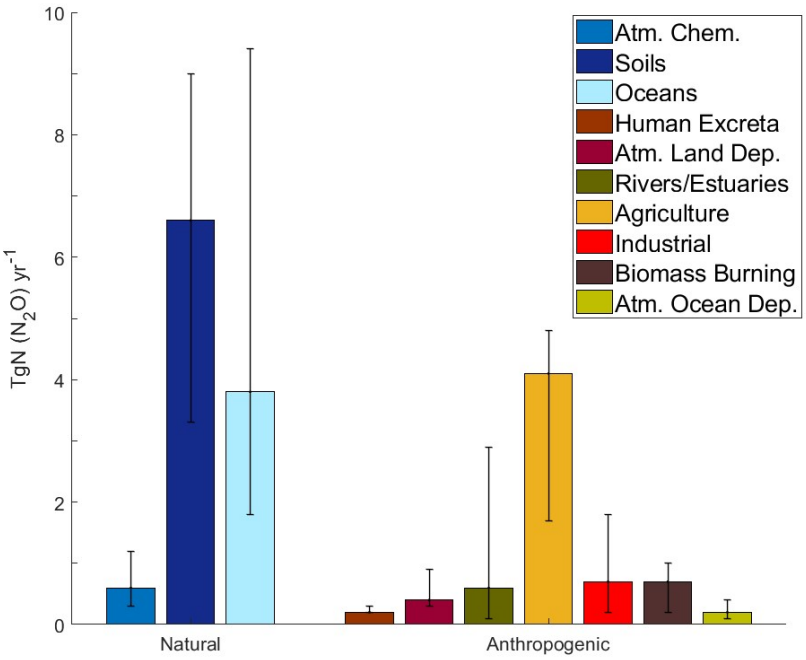

Figure 1.2. Natural and anthropogenic N_2O sources in 2011 (Ciais et al. 2013). Units are TgN (N_2O) yr^{-1}. Natural sources in shades of blue, anthropogenic in shades of yellow and red. Error bars represent best low and high estimates.

Production of N_2O in the oceans is achieved through microbial nitrification and denitrification (Popp et al. 2002; Nevison et al. 2003) producing 3.8 (1.8-9.4) TgN (N_2O) yr^{-1} (Ciais et al. 2013). Ocean N_2O is produced primarily in the top 500 m, where surface conditions promote N_2O production (Freing et al. 2012). Most of the sampling of ocean N_2O production has taken place in "hot spots" such as the Arabian Sea or the tropical Pacific, leaving much of the oceans unmeasured. The very large range in uncertainty is due to the fact that the majority of the oceans are unmonitored and the constantly changing conditions (dissolved O_2, temperature, pressure, nitrogen content of organic matter) that influence the amount of N_2O produced through microbial processes and are difficult to model with high certainty (Nevison et al. 2003).

Atmospheric chemistry amounts to 0.6 (0.3-1.2) TgN (N_2O) yr^{-1} (Ciais et al. 2013). The main reaction that contributes to natural N_2O production in the atmosphere is ammonia oxidation. While this is a small source compared to the production from soils or the oceans, it is considered to impact the global total source.

With nearly 40% of N_2O production attributed to anthropogenic origins, it is important to fully understand the impacts humans have on N_2O. By far, the largest anthropogenic source is agriculture, producing 4.1 (1.7-4.8) TgN (N_2O) yr^{-1} (Ciais et al. 2013). Food production contributes up to 80% of the observed increase in N_2O since 1860 (Galloway et al. 1995; Davidson and Kanter 2009,).

The nitrogen in fertilizers also contributes to reactive nitrogen in rivers, estuaries, and coastal systems through runoff and nitrogen leaching (Seitzinger and Kroeze 1998). While the calculated production of N_2O is small at 0.6 TgN (N_2O) yr^{-1}, the relative uncertainty is one of the largest for any single source, 0.1-2.9 TgN (N_2O) yr^{-1} (Ciais et al. 2013). This uncertainty is due to the spatial and temporal variations in land use which affects the amount of nitrogen in these systems. Recent studies suggest rivers could be more important sources of N_2O than previously thought (Rosamond et al. 2012).

Industrial and fossil fuel sources contribute 0.7 (0.2-1.8) TgN (N_2O) yr^{-1} (Ciais et al. 2013). N_2O is formed as an intermediate during the combustion processes (Ogawa and Yoshida, 2005a). The amount of N_2O produced is related to fuel characteristics, air-fuel mixes, combustion temperatures, and the use of pollution control equipment. Industrial production of adipic acid and nitric acid also contributes to the production of N_2O (Oliver et al. 1998).

Biomass burning produces 0.7 (0.2-1) TgN (N_2O) yr^{-1}. Emission of N_2O from biomass burning can occur during the combustion process or by increasing the available nitrogen in the soil after combustion. In areas where biomass burning is common, N_2O emissions from this source can be very large (Gutierrez et al. 2005).

The last anthropogenic sources that influence the global budget are atmospheric deposition and human excreta. Atmospheric N-deposition on land amounts to 0.4 (0.3-0.9) TgN (N_2O) yr^{-1} while the atmospheric deposition on ocean amounts to 0.2 (0.1-0.4) TgN (N_2O) yr^{-1} (Suntharalingam et al. 2012). N fertilizers and fossil fuel combustion increase the amount of nitrogen oxides (NO_y) and ammonia species (NH_x) in the atmosphere which eventually fall back down to the Earth's surface and provide ecosystems with an extra source of available nitrogen. Human sewage amounts to 0.2 (0.1-0.3) TgN (N_2O) yr^{-1} (Ciais et al. 2013). Facilities designed to take in human waste provide good conditions for N_2O producing bacteria, which are used as a means to break down sewage.

1.2.2 N_2O Sinks

Land and ocean sinks for N_2O are considered to be negligible on the global scale, leaving the stratosphere the only sink that impacts the global budget. Once N_2O has reached the stratosphere, it is destroyed predominantly (90%) by photo-disassociation into N_2 and O atoms (eq. 1.1). Approximately 4% of stratospheric N_2O reacts with electronically excited oxygen atoms (formed by the photolysis of ozone to form NO (eq. 1.2)) while the remaining 6% forms N_2 and O_2 (eqs. 1.3 and 1.4) (Minschwaner 1993).

(1.1) $N_2O + h\nu \rightarrow N_2 + O(^1D)$ 90% λ = 185-230 nm

(1.2) $O_3 + h\nu \rightarrow O(^1D) + O_2$ $\lambda < 320$ nm

(1.3) $O(^1D) + N_2O \rightarrow N_2 + O_2$ 6%

(1.4) $O(^1D) + N_2O \rightarrow 2\ NO$ 4%

The magnitude of these reactions is known well compared to individual source uncertainties and thus provide a means for a top-down constraint when calculating the global budget of N_2O (Nevison et al. 1999; Prather et al. 2012).

Equation 1.4 supplies the main source of NO_y in the stratosphere. The production of NO is important in stratospheric ozone chemistry, since NO reacts catalytically to destroy ozone (eqs. 1.5 and 1.6).

(1.5) $NO + O_3 \rightarrow NO_2 + O_2$

(1.6) $NO_2 + O \rightarrow NO + O_2$

The net reaction is given in equation 1.7.

(1.7) $O_3 + O \rightarrow 2\ O_2$

1.3 N_2O Distribution and trends

The global distribution of tropospheric N_2O is fairly uniform due to its long lifetime, though small variations do exist. A north-south gradient in concentration is detectable when comparing measurements from different latitudes, with 30°N and greater at the highest concentrations. The mean difference between the hemispheres is 0.8-1.0 ppb (Khalil and Rasmussen 1983; Ishijima et al. 2009). This difference can be used to calculate the emission ratio for the northern and southern hemisphere when also taking into account the inter-hemispheric exchange time (~1 year). The generally accepted emission ratio between hemispheres is ~1.5 (Hirsch et al. 2006; Ishijima et al. 2009).

Emissions in the northern hemisphere are greatest between 0-30°N driven by soil emissions in the tropics (Prinn et al. 1990; Prinn et al. 2000).

The average global trend in N_2O over the last several decades is 0.73 ± 0.03 ppb yr^{-1}. Variability in the observed trend is greatest before 1995 with values ranging between 0.3-0.9 ppb yr^{-1} (Ciais et al. 2013). This variability is linked to interannual variations in transport processes. However, fewer measurements using less precise measurement methods during this time may contribute to observed variability (Prinn et al. 2000).

The seasonality of N_2O is determined by a combination of stratosphere-troposphere exchange (STE), interhemispheric transport, and surface fluxes (Jiang et al. 2007; Ishijima et al. 2009; Nevison et al. 2011). How impactful a specific driver is to seasonality depends on location. The stratosphere has a large influence in both northern and southern hemisphere seasonality while out-gassing from the ocean surface has been linked to the observed seasonality in the mid-tropics and southern hemisphere (Jiang et al. 2007). It is important to note that interannual variability can vary strongly year to year at some locations, which makes a "mean" seasonal cycle difficult to distinguish (Nevison et al. 2011).

Seasonal phasing and magnitude are dependent on latitude. The observed seasonal magnitude at the South Pole (90°S, 102°W) is ±0.29 ppb with maximum and minimum amplitude in November and April, respectively, where as the observed magnitude at Alert, Canada (82°N, 62°W) is 1.15 ppb with maximum and minimum amplitude in March and September, respectively (Jiang et al. 2007). High latitude minimums in late-summer months are related to the influx of N_2O depleted air from the stratosphere during the spring (Liao et al. 2004; Nevison et al. 2004).

1.4 Isotopic composition of N_2O

Isotopic composition measurements of atmospheric samples have the potential to greatly reduce the uncertainty for individual source emissions as well as to inform how regional N_2O sources contribute to observed concentrations and trends. Different sources of N_2O have distinct isotopic compositions due to the fractionation effects in sources. These unique characteristics in isotopic composition can reduce the uncertainty of N_2O sources when calculating the global budget by adding further constraints.

To measure the isotopic composition of N_2O in an air sample, measurements of each isotopic species (nitrogen: ^{14}N, ^{15}N and oxygen: ^{16}O, ^{17}O, and ^{18}O) are compared against a standard reference with a known isotopic composition. The most common way to express this comparison is using the δ notation:

(1.8) $$\delta(‰) = [R_{sa}/R_{std} - 1]1000$$

Where R is the ratio of:

(1.9) $$R = {}^{15}N/{}^{14}N;\ {}^{17}O/{}^{16}O;\ {}^{18}O/{}^{16}O$$

R_{sa} represents the ratio in the sample where R_{std} represents the ratio in the standard. Atmospheric N_2 is the standard for ^{15}N abundance ($^{15}R_{std}$ = 3676.5±4.1 ppm, Junk and Svec, 1958) while VSMOW (Vienna Standard Mean Ocean Water) is used for comparing against ^{17}O and ^{18}O in this work ($^{17}R_{std}$ = 379.9±1.6 ppm, li et al. 1988, $^{18}R_{std}$ = 2005.20±0.43 ppm, Baertschi, 1978). The δ term is expressed in per mil (‰) out of convenience because the change in isotopic composition is generally very small, of order parts per thousand.

Samples that are found to have more of the heavy isotope than the standard have positive δ values and are sometimes referred to as “heavy” or “enriched”. Samples that

have less of the heavy isotope than the standard have negative δ values and are sometimes referred to as “light” or “depleted”.

Because N_2O is a linear molecule with the oxygen atom on the end, it is also possible to determine which position the ^{15}N atom is in if present in the molecule. The placement of the ^{15}N atom can be determined using isotope ratio mass spectrometry (IRMS) when measuring the correct masses. Two different notations distinguishing the difference between the terminal ($^{15}N^{14}NO$) or central position ($^{14}N^{15}NO$) are commonly used (Toyoda and Yoshida 1999; Rockmann et al. 2003). In this work, $^{15}N^{\alpha}$ represents the central position and $^{15}N^{\beta}$ represents the terminal position. The bulk ^{15}N for a sample is the linear sum of the two positions.

Another useful way to differentiate sources is by site preference (SP), defined as:

(1.10) $$SP = \delta^{15}N^{\alpha} - \delta^{15}N^{\beta}$$

Often a SP value will be reported for sources instead of $\delta^{15}N^{\alpha}$ or $\delta^{15}N^{\beta}$. Isotopic analysis can be a very powerful tool to reduce the uncertainty in source emissions of N_2O, but an understanding of the isotopic signatures of sources and isotopic fractionation accompanying sink processes affecting atmospheric N_2O is needed.

1.4.1 Source composition

Due to the many controlling factors that determine the isotopic composition, measured values of $\delta^{15}N$, $\delta^{18}O$, and SP can vary greatly, even within the sources themselves. Commonly reported values of $\delta^{15}N$, $\delta^{18}O$, and SP for N_2O sources are given in table 1.2. Large ranges exist for source types due to the difficulty in measuring source compositions and variance in conditions at a given location.

For agricultural soils, isotopically depleted values for $\delta^{15}N$ are reported ranging from -41‰ to -9.6‰ (Perez et al. 2001; Rock et al. 2007; Park et al. 2011). Natural soils are also depleted in $\delta^{15}N$, ranging from -18‰ to -5.5‰. However, agricultural soils are much more depleted than the natural soils (Bol et al. 2003; Tilsner et al. 2003; Goldberg et al. 2008; Park et al. 2011). This is because the nitrogen in fertilizers is isotopically light, increasing the amount of ^{14}N available for microbial processes. Kinetic isotope effects (KIEs) are also expected as nitrogen availability increases because microbial processes are no longer N-limited. The $\delta^{18}O$ value for agricultural soils has a range between 23.3‰ and 41.3‰. Natural soils report an even greater range for $\delta^{18}O$ between 12.1‰ and 47‰. Because nitrification and denitrification processes can both contribute significantly to soil N_2O, the range in isotopic composition is observed to be large for both $\delta^{15}N$ and $\delta^{18}O$.

Table 1.2. Published $\delta^{15}N$, $\delta^{18}O$, and SP values for different sources of N_2O. $\delta^{15}N$ is referenced against air N_2, $\delta^{18}O$ is referenced against VSMOW. If given, ± is 1σ.

	Source	Study	$\delta^{15}N$(‰)	$\delta^{18}O$(‰)	SP(‰)	$\delta^{15}N^{\alpha}$(‰)	$\delta^{15}N^{\beta}$(‰)
Anthropogenic	Ag. Soil	1	-34±12	26.3±4.4	1.5±21	-33±17.5	-34±41
		2	-41±4	23.3±2.6	9±2.9	-37±18	-46±21
		3	-9.6±18	41.3±12.3			
	Bio. Bu.	4	-1.05	23.5	0.40	-0.85	-1.25
	Coal	5	9.2±5.3	45±8.9	13.3±4.9		
	Car	6	-4.9±8.2	43.5±13.9	12.2±9.1		
	River	7	-6.7±5.7	36±24.7	14.5±14		
	Estuary	8	-5.4±0.9	30.9±1.3	15.6±3	2.4±2.4	-13±1.1
		8	-12±2	25.1±5.6	36.3±6.6	6.4±2.7	30±4.6
Natural	Soils	9	-6.4	35.6			
		10	-18±4	12.1±5.9	9.7±7.9	-12.4±6.6	-22±4.3
		11	-6±6	26±4.5	2.2±0.8	-5±6.2	-7.1±6
		12	-6±10	47±7			
		12	-10±11	27.5±17.5			
	Ocean	13	4±1	37.2±1.9	24±2		
		14	3.2±0.1	47.6±0.3	11±1.2	8.7±0.6	-2.3±0.6
Atmosphere	Trop.	15	6.5±0.6	43.7±0.9	18.7±2.2		
		16	7	44.7			
		17	7±0.2	44.5±0.3	19.5±1.2	16.8±0.8	-2.6±0.9
	Low Strat.	18	10±0.6	46.8±0.6	21±1.1	20.5±1.1	-0.5±0.2
		18	12.4	48.8	22.2	23.4	1.2
		19	16±7	52.8±6	10±7	15±10	4.7±3.6

Study: 1. Park et al. 2011; 2. Perez et al. 2001; 3. Rock et al. 2007; 4. Ogawa & Yoshida 2005b; 5. Ogawa & Yoshida 2005a; 6. Toyoda et al. 2008; 7. Toyoda et al. 2009; 8. Bol et al. 2004; 9. Tilsner et al. 2003; 10. Park et al. 2011; 11. Bol et al. 2003; 12. Goldberg et al. 2008; 13. Popp et al. 2002; 14. Yamagishi et al. 2007; 15. Yoshida & Toyoda 2000; 16. Kim & Craig 1993; 17. Park et al. 2012; 18. Toyoda et al. 2004; 19. Park et al. 2004.

Nitrification and denitrification have been shown to produce different SP for N_2O. Generally, nitrification produces a positive SP (33‰ - 37‰) while denitrification results in no SP (Sutka et al. 2006; Opdyke et al. 2009). The reasoning for this is due to the bonds formed or broken in nitrification and denitrification. Depending on the reaction pathway involved, fractionation at the nitrogen atom that is bound to the oxygen atom is observed (Yoshida and Toyoda 2000; Sutka et al. 2003; Toyoda et al. 2005).

The $\delta^{15}N$ for rivers and estuaries is also depleted, ranging from -11.8‰ to -5.4‰ (Bol et al. 2004; Toyoda et al. 2009). This is a similar range for what has been measured for natural soils; however, the SP for rivers and estuaries ranges between 14.5‰ to 36.3‰ while the SP for natural soils is between 2.2‰ and 9.7‰. This difference in SP has the potential to distinguish source contributions from rivers and estuaries from natural soils.

The isotopic signature of $\delta^{15}N$ from biomass burning is measured to be close to N_2 (0‰) at -1.05‰ (Ogawa and Yoshida 2005b). The SP is 0.4‰. Measurements of car exhaust $\delta^{15}N$ were reported to be -4.9‰ while the SP was observed to be 12.2‰. The $\delta^{15}N$ measured for coal is isotopically heavy at 9.2‰ with a SP of 13.3‰; however, the isotopic composition of coal has shown a dependency on the exact method used for combustion (Ogawa and Yoshida 2005a). Coal and automotive SP measurements show that there does appear to be some fractionation effects that occur during the combustion process. It has been theorized that there is insignificant fractionation for industrial sources of N_2O between $^{15}N^{\alpha}$ and $^{15}N^{\beta}$ positions because industrial sources are not carried out enzematically (Yoshida and Toyoda 2000).

Ocean measurements of $\delta^{15}N$ values show a slight isotopic enrichment between 3.2‰ and 3.7‰ (Popp et. al. 2002; Yamagishi et. al. 2007) while the SP ranges between 11‰ and 24‰. The ocean is one of the few sources with a positive $\delta^{15}N$ value, making its isotopic signature unique.

1.4.2 Sink effects

Measurements of stratospheric N_2O have shown an enrichment of ^{15}N (Kim and Craig 1993; Park et al. 2004; Toyoda et al. 2004). From the research done by Young and Miller (1997), it was suggested that this enrichment was due to the preferential photolysis of isotopically light N_2O ($^{14}N^{14}N^{16}O$). Further experimental verification has confirmed this explanation (Miller and Young 2000; Kaiser et al. 2003a; Kaiser et al. 2006). From the quantum mechanical view point, the heavier isotopologue shifts the zero-point energy (ZPE) lower which blue shifts the absorption cross section (σ), resulting in more energy needed to break the bonds formed with the heavier isotopologue.

To model the atmospheric chemistry and transport that takes place in the stratosphere requires knowledge about the photolysis rate constants (J) that determine how quickly reactions take place for a specific species. These isotope effects are given as either the fractionation factor (α) or the fractionation constant (ε). Equation 1.11 describes the relationship between α and J while equation 1.12 describes the relationship between ε and α.

(1.11) $\alpha = J' / J$

(1.12) $\varepsilon = 1000(\alpha - 1)$

Where J' represents the photolysis rate constant of the heavy isotopologue. If the lighter isotopologue reacts faster than the heavy isotopologue, then α will be less than 1 and ε will be negative. In this case, as the reaction proceeds, enrichment of the heavy isotopologue in the reactant takes place while the product will be depleted of the heavy isotopologue.

Modeling isotopic enrichment of the reactant in a closed system can be accomplished by using Rayleigh fractionation, which describes how the composition changes after some fraction of the original N_2O concentration:

(1.13) $$\ln(R/R_i) = (\alpha-1)\ln([N_2O]/[N_2O]_i)$$

Where $[N_2O]$ represents the mixing ratio of N_2O, R represents the ratio of heavy to light molecules, α represents the photolysis fractionation factor for the species, and subscript i denotes initial values (Kaiser et al. 2002a; Butenhoff and Khalil 2007).

Isotope effects in N_2O photolysis has been studied by many groups (Table 5.1). Results from experiments show that the value of ε depends on several factors including temperature, wavelength, and the fractionating species itself (Rockmann et al. 2000; Turatti et al. 2000; Kaiser et al. 2002b; Kaiser et al. 2003a). Between wavelengths of 190 nm and 215 nm, ε has values that follow the relationship: $\varepsilon^{\alpha} < \varepsilon^{18} < \varepsilon^{\beta}$, where ε^{α} represents the ε value for $N^{15}NO$, ε^{18} represents the ε value for $NN^{18}O$ and ε^{β} represents the ε value for ^{15}NNO. All of the ε values are negative. This relationship represents that $^{15}N^{\alpha}$ is enriched the most in the stratospheric N_2O, followed by ^{18}O and then $^{15}N^{\beta}$ (Butenhoff and Khalil 2007).

The reaction of N_2O with $O(^1D)$ (eqs. 1.3 and 1.4) has also been studied. Kaiser et al. (2002a) found that all of the ε values during the reaction with $O(^1D)$ were smaller in magnitude than for photolysis, meaning less enrichment for the heavy isotopologues. The order of the ε values also changed: $\varepsilon^{18} < \varepsilon^{\beta} < \varepsilon^{\alpha}$. While this reaction only makes up 10% of the total sink, its effects may be important because the reaction is strongest in the lower stratosphere (Butenhoff and Khalil 2007).

Anomalous oxygen isotope fractionation has been observed in samples of stratospheric N_2O. Mass-independent isotopic fraction is defined as isotopic fractionation that does not scale with the difference in mass from one isotope to another. These effects are quantified using the equation:

(1.14) $$\Delta^{17}O = \delta^{17}O - \gamma\delta^{18}O$$

Where γ represents the "three isotope exponent" for oxygen. The γ value has a small range dependent on temperature, though most often has a value of 0.516 verified experimentally (Cliff and Theimens 1997; Kaiser et al. 2004).

The $\Delta^{17}O$ anomaly is non zero for the troposphere and stratosphere and increases with altitude (Cliff and Theimens 1997). This result was unexpected due to the fact that the sources and sink processes of N_2O are mass dependent processes. While possible explanations have been proposed and reviewed (Miller and Young 2000; Estupiñán et al. 2002) the most accepted explanation is the transfer of heavy oxygen from O_3 to N_2O in the reaction with $O(^1D)$ (Butenhoff and Khalil 2007).

1.4.3 Atmospheric composition

Troposphere measurements of $\delta^{15}N$ have values close to 7‰ and SP ~19‰ (Park et al. 2004; Toyoda et al. 2004; Park et al. 2012). $\delta^{15}N$ measurements from the stratosphere are more enriched than the troposphere, ranging from 10‰ to 16.4‰. These values are also enriched compared with the sources discussed previously (Table 1.2). The troposphere has isotopically heavier $\delta^{15}N$ values compared to the sources due to sink effects that occur in the stratosphere which enrich stratospheric N_2O (^{15}N, ^{17}O, ^{18}O) and enrich the troposphere through STE.

The historical trend in troposphere isotopic N_2O has been considered in several studies. Park et al. (2012) measured the isotopic composition of 11 firn air samples collected between 1997 and 2004 from Law Dome, Antarctica 67°S, 113°E and 50 archived air samples collected between 1978 and 2005 from Cape Grim, Tasmania 41°S, 145°E. Results of these measurements show that as the N_2O mixing ratio in the atmosphere increases, the $\delta^{15}N$ decreases. This can be explained by the fact that many anthropogenic sources of N_2O have lighter $\delta^{15}N$ values than natural sources (Table 1.2).

Park et al. (2012) also evaluated how the $\delta^{18}O$ value has changed over time. From their results, as the atmospheric concentration of N_2O increases, the $\delta^{18}O$ values become lighter, though to a smaller degree than seen in the bulk isotopic composition of N_2O. This is expected since the oxygen source for both anthropogenic and natural sources is a combination of molecular O_2 and oxygen bound in water (Rahn and Whalen 2000).

Finally, seasonal cycles in the isotopic composition were also observed in southern hemisphere samples from the Cape Grim archive by Park et al. (2012). Both $\delta^{15}N$ and $\delta^{18}O$ show enrichment during the summer months and depletion during the winter. N_2O mole fraction had maximum and minimum mixing ratios during late fall and

late spring, respectively. The minimum in late spring was found to coincide with the maximum in STE bringing isotopically heavy N_2O to the surface (Nevison et al. 2005; Nevison et al. 2011).

1.5 Sulfur hexafluoride

SF_6 is an extremely potent GHG with a GWP (over 100 years compared to CO_2) of 22800. Until recently, the commonly reported lifetime of SF_6 was ~3200 years (Ravishankara et al. 1993); however, newer estimates have greatly reduced the atmospheric lifetime to 580-1475 years (Kovács et al. 2017; Ray et al. 2017). While SF_6 is one of the strongest GHG controlled under emission regulations, it also has a small global concentration (7.28 ppt in 2011), so it does not add significantly to climate forcing by itself (Myhre et al. 2013).

Sources of SF_6 are anthropogenic, with main uses being high voltage insulation, magnesium production and semiconductor manufacture (Maiss & Brenninkmeijer 1998; Olivier et al. 2005). With a very low solubility, the only known sink for SF_6 is loss to the mesosphere. Almost all of the SF_6 that has been emitted since the industrial revolution is still present in the atmosphere. Atmospheric observations of concentration are used to accurately determine global emissions. Due to its long lifetime and anthropogenic origins, SF_6 is used as a validity check for atmospheric transport models (Levin and Hesshaimer 1996; Patra et al. 2009).

Reported atmospheric measurements of SF_6 from atmospheric air before the year 1987 are rare. In the southern hemisphere, Cape Grim (Tasmania) archive measurements date back to 1978 (Levin et al. 2010). Eight northern hemisphere measurements are

reported that date between 1973 and 1990 from Trinidad Head, CA (Rigby et al. 2010). Few other measurements pre-1990 are available or reported for either hemisphere.

1.6 SF_6 Global budget

Estimating the global production of SF_6 is less complex than for N_2O due to the fact SF_6 is only produced through anthropogenic means in significant quantities. The Emissions Inventory for Global Atmospheric Research (EDGAR) has the emissions of SF_6 broken down by country and year. Figure 1.3 shows the SF_6 emissions from EDGAR V4.2 for the year 2010 in Gg grouped by continent.

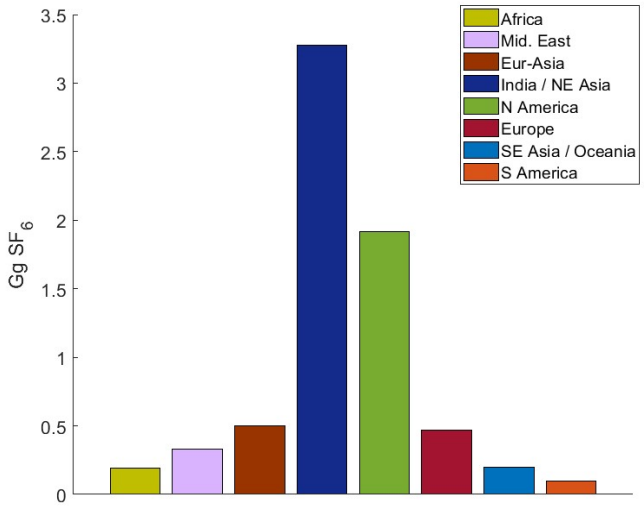

Figure 1.3. 2010 SF_6 emissions in Gg by continent (EDGAR 2013).

The three top producing countries are China (2.4 Gg), USA (1.7 Gg), and Korea (0.3 Gg), showing that the emissions of SF_6 are heavily dominated by the United States and China. The total emission of SF_6 for 2010 in EDGAR is 7 Gg.

Top-down calculations by Levin et al. (2010) estimate global production in 2008 to be 7.16 Gg yr^{-1}. This number is very close to the EDGAR database and shows how verification of global emissions using very few globally distributed atmospheric background sampling stations is possible. For GHGs with well-defined sinks, the top-down calculations are one of the strongest constraints for verifying global budgets.

1.7 SF_6 Distribution and trends

Observations of SF_6 background mixing ratio shows a latitudinal dependence in the northern hemisphere (Geller et al. 1997), with the highest mole fraction observed at mid-northern latitudes. For the year 1994, measurements from Fraserdale, Canada (50°N, 82°W) are reported to be 0.14 ppt higher than samples measured from Izaña, Tenerife (28°N, 16°W) (Maiss et al. 1996). Southern hemisphere mixing ratios are more consistent across latitudes.

The mean tropospheric SF_6 concentration reported in 1990 in the north and south hemisphere is 2.67 ppt and 2.34 ppt, respectively (Maiss et al. 1996). It is estimated that ~94% of all SF_6 emissions come from the northern hemisphere (see fig. 1.3, Maiss et al. 1996; EDGAR), which explains why northern hemisphere samples are higher in SF_6 concentration than southern hemisphere samples by 0.3-0.4 ppt (Levin et. al. 2010).

Variability in the SF_6 trend has been observed over the last 30+ years. While the exact value of the growth rate differs slightly between sample locations, several features are prominent (Levin et al. 2010; Rigby et al. 2010; Hall et al. 2011). From initial measurements in the 1970s the trend steadily increased until the mid-1990s, where it

peaked near 0.26 ppt yr^{-1}. The trend then slowly declined to ~0.20 ppt yr^{-1} until the early 2000s, when it began to increase once again.

Although small in magnitude, SF_6 has been observed to have seasonality at select locations. The driving force behind the observed seasonality in SF_6 is considered to be atmospheric transport (Patra et al. 2009). Processes such convection, boundary layer mixing, stratosphere-troposphere exchange (STE), and shifts in the ITCZ all can potentially influence the observed seasonality at a location. In general, seasonal amplitude in the northern hemisphere is ~0.05 ppt while southern hemisphere amplitude is ~0.01 ppt (Nevison et al. 2007; Patra et al. 2011). The seasonal phase depends on location and is not consistent within a hemisphere. At Cape Grim, Tasmania (41°S, 145°E), the phase in the minimum is near February and maximum near October. Barrow, AK (71°N, 157°W) and Alert, Canada (82°N, 62°W) show strong minimums in the fall, though maximums are not clearly defined (Wilson et al. 2014). Continental sites such as Niwot Ridge, CO (40°N, 106°W) show large influences from interannual variability (IAV) and have no distinguishable seasonality (Patra et al. 2009)

1.8 Dissertation overview

There many questions remaining concerning the changing contribution of individual sources to the global budget of N_2O as well as seasonality in northern hemisphere sources. There is also limited atmospheric air samples of SF_6 from the late 1970s and 1980s, especially in the northern hemisphere. The work presented in this dissertation presents a valuable contribution towards addressing these questions by examining the Oregon Health & Science University–Portland State University (OHSU-

PSU) air archive consisting of archived air samples collected from Cape Meares, Oregon (45.5°N, 124°W). Chapter 2 presents in detail the high precision methods developed at Portland State University to analyze the air archive. Mole fraction results of N_2O and SF_6 analyses are presented and discussed in chapter 3. The N_2O isotopic analysis of the OHSU-PSU air archive is presented and discussed in chapter 4. In chapter 5, a simple 2-box model of the atmosphere is used to evaluate total source contributions to the observed measurements and compared with previous literature. Finally, chapter 6 discusses what conclusions can be made from this work.

Chapter 2

Experimental Methods

This chapter discusses the measurement and analytical methods used in this research. The first section (2.1) gives information regarding the air archive samples collected from Cape Meares. The second section (2.2) discusses the measurement techniques used to analyze samples for their N_2O and SF_6 mole fraction content using gas chromatography. The third section (2.3) discusses how samples were measured for their N_2O isotopic composition using isotope ratio mass spectrometry. The fourth section (2.4) explains the analytical techniques used to process the data.

2.1 Air archive samples

Using past concentrations from the last several decades can help constrain global budget uncertainties as well as shed light on recent changes to source and sink processes. When projecting future GHG concentrations, many factors must be included such as climate feedback effects and possible changes in transport processes. Uncertainties in model results can be minimized if GHG measurements span many years, are precise, and cover many different latitudes. Past atmospheric conditions can be evaluated using either archived air samples or by analyzing ice core and firn air.

The major advantage of using ice core or firn air for measuring past atmospheric concentrations of GHG is that samples may be collected today. However, samples are difficult to obtain due to the remoteness of the locations where the samples are collected (Greenland and Antarctica). This also limits spatial resolution as polar regions may not accurately represent mixing ratios at more central latitudes. Temporal uncertainties also must be evaluated when measuring ice core and firn samples. Therefore, these samples are better represented by a mean age of the air rather then an exact date.

Archived air samples are discrete in time and space. This makes them very valuable for evaluating past atmospheric conditions at unique periods in time, but few archived samples are available today. Archive samples may also become contaminated or lost if not stored properly.

The Oregon Health & Science University–Portland State University (OHSU-PSU) air archive consists of archived air samples collected from Cape Meares, Oregon (45.5°N, 124°W) by Dr. Rasmussen (Department of Environmental and Bimolecular Systems, Oregon Graduate Institute of Science and Engineering (currently OHSU)) and Dr. Khalil

(Physics Department, Portland State University). The samples were collected by air liquefaction, where ~1000L of air (STP) is compressed to 30bar into 33L electropolished stainless steel canisters. The air archive consists of 210 samples with sample dates ranging from 1978 to 1998 (Rice et al. 2016). Of the 210 samples, 156 were analyzed in this work, with sample dates ranging from 1978 through the end of 1996.

2.2 Gas chromatography

The gas chromatography (GC) analytical system was based on the configuration used by Hall et al. (2007) and uses an Agilent 6890N gas chromatograph fitted with a micro-electron capture detector (μECD, Agilent Technologies, Santa Clara, CA). Peak separation of N_2O and SF_6 from air is achieved by two Poropak Q 80/100 mesh columns (6 ft long, 2 mm i.d. pre-column, 12 ft long, 2 mm i.d. analytical column). The carrier gas is P5 (Airgas, Portland, OR) equipped with O_2 and hydrocarbon traps (Restek, Bellefonte, PA) to improve baseline signal stability. Two six-port switching valves (V_1 and V_2) are controlled through Chemstation (V1.A, Agilent Technologies Inc., Santa Clara, CA). A schematic of the GC system is given in figure 2.1.

A 16-port multiposition valve (Valco Instrument Company Inc., Houston, TX) controlled by the GC interface is used to introduce pressurized samples into the system. A 2-way electric valve (Clippard, Cincinnati, OH) is used to halt sample introduction and prevent sample loss when not flushing the sample loop. Samples initially pass through a nafion-tube/desiccant trap (Perma Pure, Toms River, NJ), before flushing the 10ml sample loop to help remove water from samples. Once flushed, the sample loop is placed

in line with the pre-column by rotating V_1, when the P5 carrier carries the air aliquot onto the pre-column.

To rotate between back-flush and front-cut, a 4-port valve is used (V_3). In back-flush, carrier gas flushes the pre-column (in the opposite direction sample travels) to remove the build up of water and other late-eluting compounds on the column that would otherwise elute to the μECD and affect signal baseline. In front-cut, carrier gas carries sample from the sample loop to the pre-column. Once the O_2 elutes through the pre-column to vent, V_2 rotates and places the pre-column in line with the main-column allowing N_2O and SF_6 to transfer to the analytical column. Once the sample has reached the analytical column, V_1, V_2, and V_3 rotate, back-flushing the pre-column while the analytes are carried to the detector.

The oven and detector temperatures are held isothermally at 56°C and 310°C respectively. Carrier gas flow rates are 40 ml min^{-1}. The N_2O peak retention time is 6.1 minutes; the SF_6 peak retention time is 7.0 minutes. Peak integration is accomplished via Chemstation via peak height (peak area was also considered but was found to be less precise). Measurements of N_2O and SF_6 are made relative to a calibrated whole air sample on the NOAA-06A scale (NOAA Tank CB11406-A, 328.71 ppb N_2O, 8.76 ppt SF_6). Each sample is analyzed 6 times and bracketed by 6 reference gas runs used to track signal drift. A detailed description of a typical run with pressure settings and timing is as follows:

Time (min)	Description
0.00 - 1.50	System starts a run in “back-flush”. The starting pressures for Carrier 1 and Carrier 2 are 62.1 and 67.4 psi, respectively. The stream selection

multi-position valve rotates to the desired position and the solenoid (on/off) valve switches on (open). Sample flows through a water trap then to a 10 ml sample loop and finally to vent. The sample loop is flushed with sample for 1.5 minutes at 60 ml min^{-1}. Then the on/off valve switches off (closed), stopping the flow of sample.

1.50 – 1.75 Sample remains in the sample loop for 15 seconds to equilibrate with atmospheric pressure. At 1.75 minutes, Valve 3 rotates, switching from "back-flush" mode to "front-cut" mode.

1.75 - 3.00 Valve 1 rotates, allowing Carrier 2 to take the sample from the sample loop to the pre-column and then to vent.

3.00 - 3.05 Valve 2 rotates, placing the pre-column in line with the analytical column. N_2O and SF_6 in the sample is carried by Carrier 1 from the pre-column into the analytical column. Carrier 1 pressure is increased to 76 psi to maintain constant flow to the detector. Carrier 2 pressure decreased to 20 psi to reduce loss to vent. Valve 1 rotates back to its initial position.

3.05 - 4.25 Sample flows through the main column.

4.25 - 4.30 Valve 2 switches back to its initial position ("back-flush" mode). Carrier 2 begins to back-flush the pre-column. Carrier 1 pressure decreases to 67.4 psi and Carrier 2 pressure increases to 62.1 psi.

4.30 - 8.00 The sample is carried through the main column. The maximum intensity for N_2O occurs at 6.1 minutes while SF_6 has maximum intensity at 7.0 minutes. At ~8 minutes, the signal baseline has returned to normal.

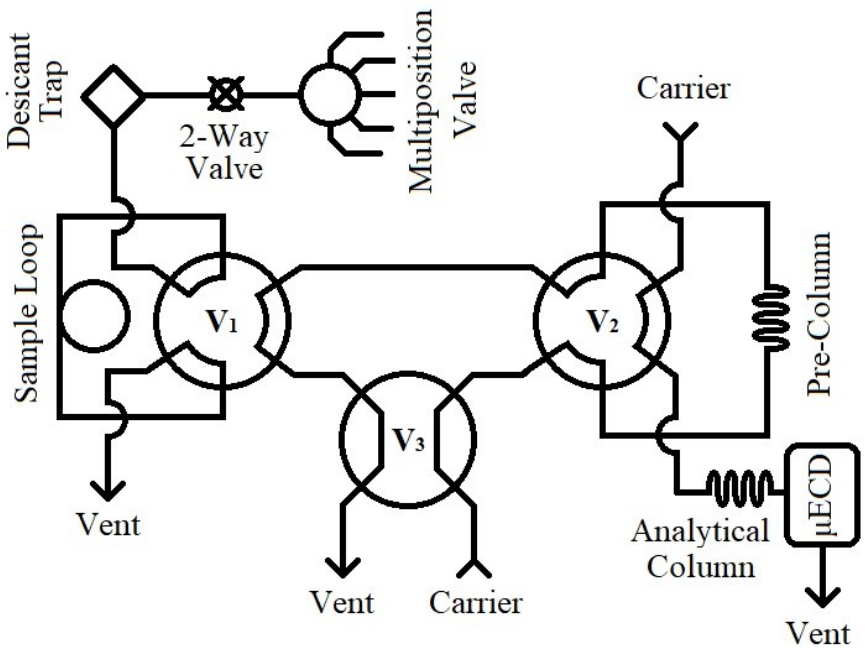

Figure 2.1. Schematic of the system for sample evaluation on GC. The system is shown in "back-flush" mode. V_1 = Valve 1, V_2 = Valve 2, V_3 = Valve 3.

Test runs were performed with and without the "heart-cut" technique. Chromatogram output without venting O_2 before reaching the detector is shown in figure 2.2a. A very large O_2 peak is seen at ~2.75 minutes. The peak at 4 minutes is the N_2O peak and no SF_6 peak is visible. Inflections before 2.5 minutes and near 5.5 minutes are due to pressure fluctuations from valve rotations. Chromatogram output using the "heart-cut" technique is shown in figure 2.2b. The large peak at 6.1 minutes is the N_2O peak followed by the SF_6 peak at 7.0 minutes. Inflections before the N_2O peak are due to pressure fluctuations due to valve rotations.

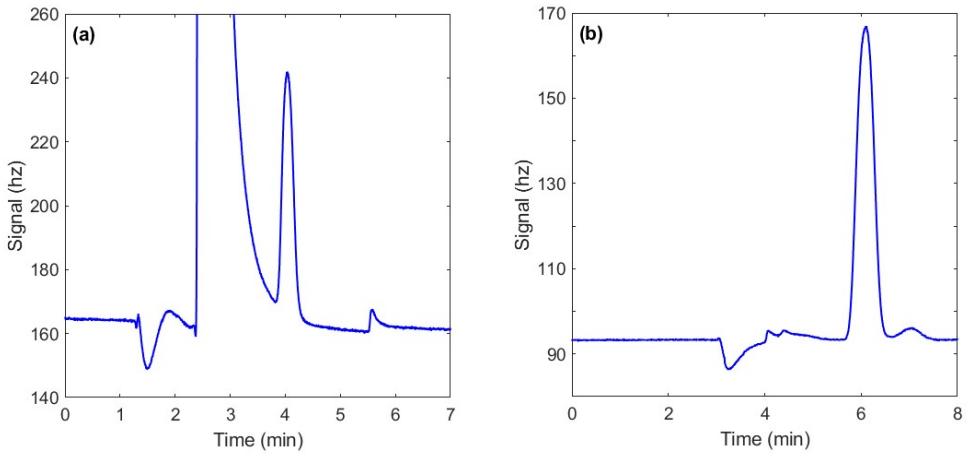

Figure 2.2. GC Chromatogram output. Chromatogram without "heart-cut" technique shown in (a). Visible peaks are O_2 peak ~ 2.75 minutes and N_2O ~4 minutes. Chromatogram in Figure (b) shows with "heart-cut" technique. Visible peaks are N_2O peak at 6.1 minutes and SF_6 peak at 7.0 minutes.

2.3 Isotope ratio mass spectrometry

Over the time period that archived samples were collected from Cape Meares (1978 – 1998), the change in atmospheric N_2O isotopic composition is small. The mixing ratio of N_2O in the atmosphere is also low (300 - 315 ppb between 1978 and 1996), making it is necessary to concentrate samples before they reach the IRMS detector array to produce a sufficient signal. Additionally, in atmospheric samples CO_2 is in excess by over 1000 times, which causes interference with N_2O in the detector due to interfering isotope masses 44/45/46, so CO_2 must be dramatically reduced. The preconcentration system shown in figure 2.3 is based on designs by Toyoda and Yoshida (1999), Kaiser et al. (2003b), Rockmann et al. (2003), and Potter et al. (2013) and preconcentrates N_2O from whole air samples before transferring to the GC-IRMS system.

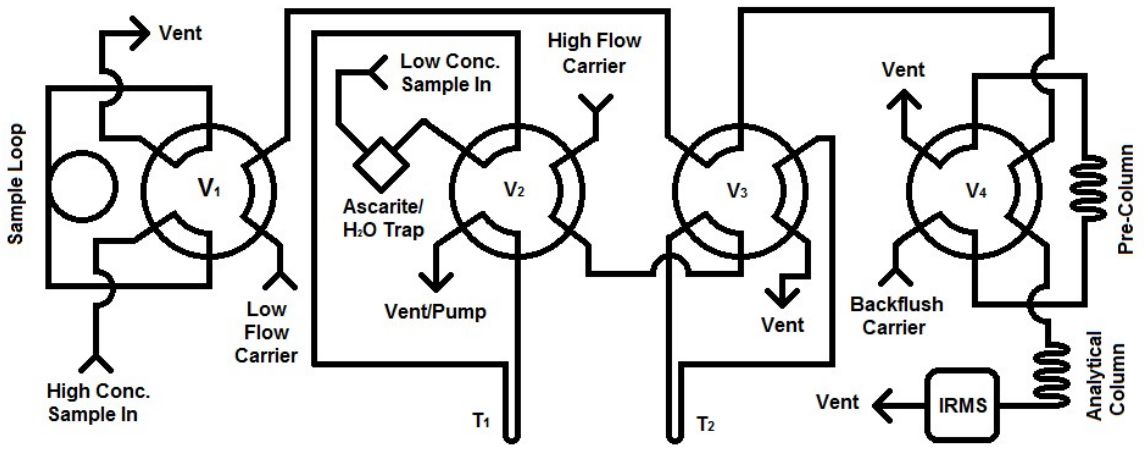

Figure 2.3. Preconcentration system and GC-IRMS schematic for N_2O isotopic analysis. V_1 = valve 1, V_2 = valve 2, V_3 = valve 3, V_4 = valve 4, T_1 = large LN cooled trap, T_2 = cryofocus LN cooled trap. Valves all shown in "off" position.

The isotopic analysis system is composed of 3 primary sections: the preconcentration section, the GC, and the IRMS. The preconcentration section was designed and fabricated at PSU and uses four 6-port switching valves (Valco Instrument Company Inc., Houston, TX), two liquid nitrogen (LN) traps, one chemical trap (70% NaOH, 30% $MgClO_4$) to remove CO_2, and one H_2O trap (steel loop and dry ice). A Thermo Scientific Trace Ultra GC contains the pre-column and the analytical column, held isothermally at 35°C in the oven. The GC (fitted with electronic flow control) is also used to regulate the He low flow carrier and is where the open-split interface is located. The final piece, the IRMS, is a Thermo Scientific Delta V Isotope Ratio Mass Spectrometer fitted with a 5-feraday cup collector system. GC-IRMS runs are controlled and recorded through Thermo Scientific Isodat v2.5.

This system is designed for the analysis of both high concentration samples (above 10 ppm) using valve 1 (V_1) as well as atmospheric concentration samples (~300

ppb) using sections connected through valves 2-4 (V_2, V_3, V_4). High concentration samples are injected using a syringe through a septa and flush a sample loop. Rotating V_1 allows low flow He carrier gas to take the sample to the main column and to the IRMS. For the work presented in this dissertation, the low concentration sections are used.

Pressurized sample canisters containing low concentration samples of N_2O are connected to a mass flow controller (OMEGA Engineering, Inc., Norwalk, CT) that regulates the flow rate at 40 ml min^{-1} through the chemical and water traps. The sample then flows into the first cold trap (T_1, -196°C) cryogenically separating N_2O and remaining condensable components from bulk air. A pump downstream of T_1 prevents the condensation of O_2 by ensuring that the pressure in T_1 stays well-below atmospheric pressure. When V_2 rotates, the sample in T_1 is warmed to 90°C by submerging in water, then cryofocused into the second cold trap, T_2 (-196°C) carried by the He high flow carrier. Once the sample has transferred from T_1 to T_2, V_2 rotates back to its initial position with T_1 held at 90°C so that residual water may be flushed out using the He high flow carrier.

The rotation of V_3 and V_4 allows the transfer of sample from T_2 to the pre-column (Supel-Q PLOT, 30m by 0.53mm, Supelco) once T_2 is submerged in water heated to 90°C. V_3 is rotated back to its initial position when the entire sample has reached the pre-column and flushed with carrier gas to remove any compounds still present in the trap. A pre-column with backflush is necessary due to heavier, late eluting compounds that can affect subsequent analyses, particularly on mass 31 (Toyoda and Yoshida 1999, Rockmann et al. 2003, Kaiser et al. 2003b).

Samples are introduced to the IRMS ion source using an open split design (figure 7). This admits a fraction (~1/3) of the eluted gas from the analytical column (HP-PLOT Q, 30m by 0.53mm, Agilent Technologies) onto the ion source through capillary tubing. The design consists of a glass sealed tube on one end with the open end admitting capillary tubings carrying reference gas, sample, and He.

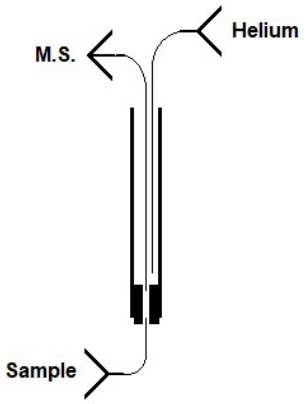

Figure 2.4. Open split interface.

The transfer capillary to the mass spectrometer will admit the different gas streams or combinations of them, to the ion source depending on the position of the capillary tubings. When the sample gas is introduced to the ion source, molecules are ionized under vacuum by bombarding them with electrons which come from a heated filament and creates positively charged ions.

A detailed description of a typical run with flow rates, temperatures, and timing is as follows:

Time (min)	Description
-1.00 - 0.00	Pressurized sample purges ascarite/H_2O traps and T_1. Flow rate is 40 ml min^{-1} controlled by the MFC. Low Flow Carrier is set at 1 ml min^{-1}. High

Flow Carrier and Backflush Carrier are set at 10 ml min^{-1}. GC oven set at 35°C.

0.00 - 9.50 T_1 is submerged in LN at -196°C. N_2O sample is trapped in T_1 while the vacuum pump prevents liquid O_2 from condensing.

9.50 - 10.00 T_2 is submerged in LN at -196°C.

10.00 - 11.50 V_2 rotates on. T_1 removed from LN and placed in a hot bath at 90°C. Sample is carried by the High Flow Carrier from T_1 and cryofocused to T_2.

11.50 - 11.75 V_4 rotates on. Low Flow Carrier increased to 3 ml min^{-1}.

11.75 - 12.00 T_1 removed from hot bath.

12.00 - 17.00 V_3 rotates on. T_2 removed from LN and placed in a hot bath at 90°C. V_1 rotates off. Sample begins transfer to the pre-column and analytical column.

17.00 Isodat run begins.

17.50 - 17.67 V_4 rotates off. Low Flow Carrier reduced to 1 ml min^{-1}. V_3 rotates off. T_2 removed from hot bath.

25.33 Isodat run ends.

A typical chromatogram output for the whole N_2O (m/z 44, 45, 46) molecule and NO (m/z 30, 31) fragment are shown in figure 2.5a and 2.5b, respectively. The sample N_2O and NO peaks ~300 seconds are sandwiched between 5 square reference peaks (UHP N_2O, Praxair, Portland, OR) (3 before, 2 after) to monitor within-run drift. Peak integration is accomplished via Thermo Scientific IRMS software (Isodat v2.5). Each

sample is analyzed 4-6 times (2-3 whole N_2O measurements, 2-3 NO fragment measurements).

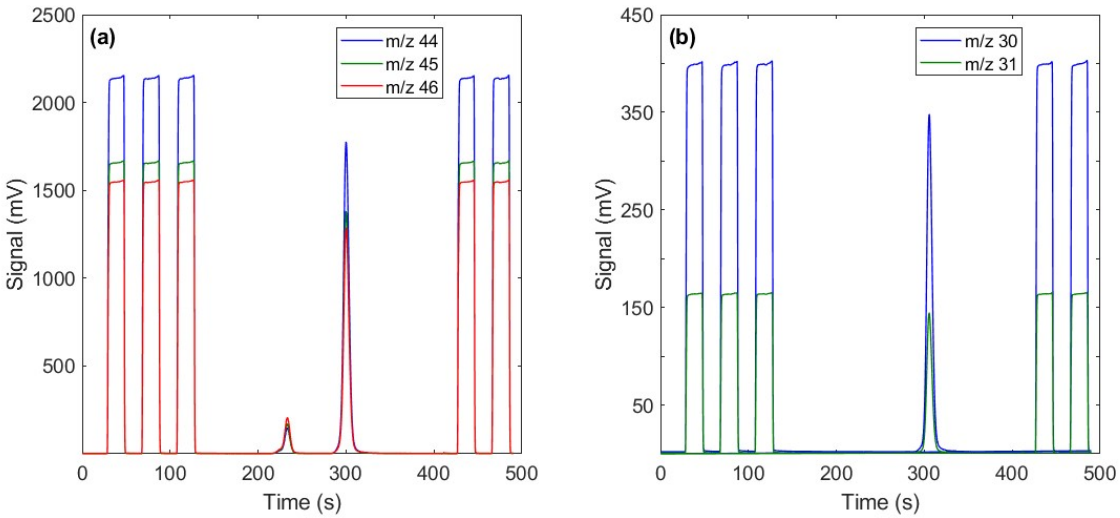

Figure 2.5. IRMS chromatograms. Whole N_2O molecule results are shown in (a). Peaks 1, 2, 3, 6, and 7 are square reference peaks, peak 4 is CO_2 and peak 5 is N_2O. NO fragment results are shown in (b). Peaks 1, 2, 3, 5, and 6 are square reference peaks while peak 4 is the NO fragment peak.

The ionized molecules are accelerated towards a magnetic field by a high voltage potential. Molecule trajectory is then forced into an arc due to the Lorentz force:

(2.1) $$F_B = z\nu B = m\nu^2/r$$

So the resulting radius of curvature r is:

(2.2) $$r = m\nu/zB$$

Where m is the mass of the molecule (kg), ν is the velocity (m/s), z is the electric charge (C), and B is the magnetic field (T). This results in heavier ions having a larger arc than smaller ions.

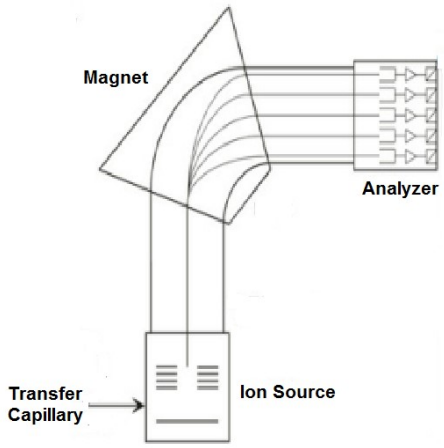

Figure 2.6. Example IRMS schematic (Rice et al. 2001).

Once passed through the magnetic field, the molecular ions reach the analyzer and are collected in an array of 3 Faraday cups (triple collector) which accumulate charge. The larger the charge and current accumulation, the more of a particular ion in a sample. To resolve the ^{15}N and ^{18}O N_2O isotopomers, five ion currents (I) are measured (N = ^{14}N and O = ^{16}O):

(2.3) $I_{44} = NNO$

(2.4) $I_{45} = {}^{15}NNO + N{}^{15}NO + NN{}^{17}O$

(2.5) $I_{46} = NN{}^{18}O + {}^{15}NN{}^{17}O + N{}^{15}N{}^{17}O + {}^{15}N{}^{15}NO$

(2.6) $I_{30} = NO$

(2.7) $I_{31} = {}^{15}NO + N{}^{17}O$

The normalized molecular ion current ratios are then calculated as:

(2.8) $^{45}R = I_{45}/I_{44} = {}^{15}R^{\alpha} + {}^{15}R^{\beta} + {}^{17}R$

(2.9) $^{46}R = I_{46}/I_{44} = {}^{18}R + ({}^{15}R^{\alpha} + {}^{15}R^{\beta})\,{}^{17}R + {}^{15}R^{\alpha}\,{}^{15}R^{\beta}$

(2.10) $^{31}R = I_{31}/I_{30} = {}^{15}R^{\alpha} + {}^{17}R$

The geometry of the Thermo Delta-V IRMS does not allow for simultaneous monitoring of all 5 desired ion configurations, so the isotopic ratio of ^{31}R is determined using subsequent samples from ^{45}R and ^{46}R. The cup configuration alters between monitoring the whole N_2O^+ molecule (m/z 44, 45, and 46) and the NO^+ fragment (m/z 30, 31, and 32) on independent IRMS runs.

The NO^+ fragment formed during the ionization process would ideally have only the nitrogen atom that was originally bound to the oxygen atom ($N^{15}NO$, or the α-portion). However, there is a known isotope "scrambling" effect that takes place within the ion source whereby some N from the β-portion (^{15}NNO) ends up in the NO^+ fragment and is measured as part of the m/z 30 and 31 ion currents. The exact percentage that is scrambled is unique to each instrument. The most commonly accepted value is roughly 8.5% of the $^{15}NO^+$ fragment will be formed from ^{15}NNO (Toyoda and Yoshida 1999; Kaiser et al. 2003b; Rockmann et al. 2003; Potter et al. 2013). The corrected equation provided by Kaiser et al. (2003b) for equation 2.10 is:

$$^{31}R = s^{15}R^{\beta} + (1-s)^{15}R^{\alpha} + {}^{17}R - \frac{s(1-s)(^{15}R^{\beta} - {}^{15}R^{\alpha})^2}{1 + s^{15}R^{\alpha} + (1-s)^{15}R^{\beta}} \quad (2.11)$$

Where *s* is the scrambling coefficient (0.00 – 1.00) and is empirically derived.

The last term in equation 2.11 comes from the fact that the double-substituted isotopomers $^{15}N^{15}NO$ contributes to the scrambled and unscrambled NO^+ fragment. However, unless working with artificially enriched ^{15}N isotopes, the correction provided by this term is negligible.

Solving for $^{15}R^{\alpha}$, $^{15}R^{\beta}$, and ^{18}O is accomplished by using equations 2.8, 2.9, and 2.11 (excluding the last term), and by taking advantage of the fixed relationship between variations of ^{17}O and ^{18}O:

(2.12) $$^{17}R/0.0003799 = (^{18}R/0.0020052)^{0.516}$$

The values 0.003799 and 0.0020052 are from the accepted natural abundance of ^{17}O and ^{18}O in the oxygen standard VSMOW. The exponent 0.516 is the "three isotope exponent" for oxygen (discussed in section 1.4.2) derived from kinetic isotope fractionation laws and has been verified experimentally (Cliff and Thiemens 1997; Kaiser and Rockmann 2003). Together, equations 2.8, 2.9, 2.11, and 2.12 are solved numerically (from ^{45}R, ^{46}R, ^{31}R) to find the four unknowns $\delta^{15}N$, $\delta^{15}N^{\alpha}$, $\delta^{15}N^{\beta}$, and $\delta^{18}O$.

2.3.1 Isotope calibration

All isotopic measurements are made relative to an internationally recognized calibration scale (N_2 in air for ^{15}N and VSMOW for ^{18}O, discussed in section 1.4). The N_2O isotopic community accepted scale for ^{15}N site preference measurements is the Tokyo Institute of Technology (TITech) scale, at least until an official site specific N_2O isotope calibration standard exists. Portland State University was very fortunate to have four electropolished stainless steel 3L canisters filled with samples at Swiss Federal Laboratories for Materials Science and Technology (EMPA) by Dr. Joachim Mohn. All of the samples were calibrated by Sakae Toyoda at TITech. Table 2.1 provides information on the EMPA standards.

Table 2.1. EMPA standard information.

EMPA Tank #	$\delta^{15}N$	1σ	$\delta^{15}N^{\alpha}$	1σ	$\delta^{15}N^{\beta}$	1σ	$\delta^{18}O$	1σ
90575	2.02	0.10	2.06	0.05	1.98	0.20	36.12	0.32
CA08214	6.85	0.06	17.11	0.12	-3.43	0.17	35.39	0.17
90454	25.58	0.14	25.73	0.24	25.44	0.36	35.86	0.22
CB08976	6.24	0.11	15.7	0.31	-3.21	0.37	35.16	0.35

The standards are ~90 ppm N_2O balanced in synthetic air at ~28 psi. To measure the EMPA standards using the same method as an archive sample, it is necessary to dilute the standards to ~300 ppb so they may be run through the preconcentration system in a manner identical to samples. This is achieved by evacuating new 3L canisters down to ~10 microns (monitored by capacitance manometers, MKS Instruments, Andover, MA) with precision of 0.1 torr. A 20 ml volume is then pressurized to ~28 psi and allowed to expand into the evacuated 3L canister. Finally, ultra-pure air (Airgas, Radnor, PA) confirmed to have N_2O below detection limits (via GC-μECD) is used to bring the final pressure of the canister to ~50 psi. Special care is taken to prevent fractionation during the dilution process by allowing equilibration to occur in each step.

The diluted 3L canisters at ~300 ppb N_2O are used to calibrate the reference gas used in all isotopic measurements as well as a working reference gas of dried air (CC2854, Breathing Air, Airgas, Portland, OR). The working reference is measured every 2 hours to monitor instrument drift. Equation 2.13 is used to calculate the deviation in measured values from accepted ("True") values:

$$\Delta(\delta^{45})_{CC2854} = {}^{True}(\delta^{45})_{CC2854} - {}^{Measured}(\delta^{45})_{CC2854} \quad (2.13)$$

where ${}^{True}(\delta^{45})_{CC2854}$ is calculated from measurements against the EMPA standards. Sample mean measured value equal to ${}^{Measured}(\delta^{45})_{sample}$ are drift corrected to the "true" value ${}^{True}(\delta^{45})_{sample}$:

(2.14) $${}^{True}(\delta^{45})_{sample} = {}^{Measured}(\delta^{45})_{sample} + \Delta(\delta^{45})_{CC2854}$$

The standard deviation of the sample is calculated as:

(2.15) $$\sigma[(\delta^{45})_{sample}] = \{(\sigma[{}^{Measured}(\delta^{45})_{sample}])^2 + (\sigma[{}^{Measured}(\delta^{45})_{CC2854}])^2\}^{0.5}$$

The same approach is used when measuring δ^{46} and δ^{31}.

2.4 Data analysis techniques

To analyze the data for statistically significant trends, LOWESS regression (smoothing) and bootstrapping are used. A description of each method and how they are applied to the data is described in the following subsections.

2.4.1 LOWESS

LOWESS regression is a locally weighted regression technique that gives more weight to data points closer to the evaluation point (Cleaveland and Devlin 1988). We define the collection date as the independent variable, x_i, and the measured value as the corresponding variable, y_i, for i = 1 to n; where n is the total number of measured data points. We then define a smoothing window span to smooth over. In MATLAB, the span has a value between 0 - 1 and is defined as q/n where $1<q<n$. As the smoothing window approaches 1, more data points are included in the smoothing and the regression becomes smoother. A smoothing window closer to 0 will show more variability.

A smoothing span defined by the ratio of data points to include works well when the data points are evenly spaced in x. This is not the case for the archived air samples as there are periods when samples are not available. So instead, the span is defined as the number of data points within a fixed window in time. For example, when calculating the seasonality, a 30 day (30/365) window is used; when calculating the annual trend, a 3 year window is used (3/total range). The spans value, between 0 - 1, depends on how many data points are within the window and can be different for every data point.

Once the span has been calculated, the next step is to define the weight (w_i) of each data point within the smoothing window. LOWESS uses a tri-cubic function:

(2.16) $$w_i = \left[1 - \left|\frac{x - x_i}{d(x)}\right|^3\right]^3$$

Where x_i are the nearest neighbors of x defined by the span and d(x) is the distance along the abscissa from x to the most distant predictor value within the span. Weights are largest for values closest to the evaluation point and have the most influence over the fit. As the distance to the evaluation point increases, the weights become smaller. Data points outside of the smoothing window are assigned 0 weight and have no influence when calculating the fit. A weighted linear regression can now be performed:

(2.17) $$wX = \frac{\Sigma w_i x_i}{\Sigma w_i}$$

(2.18) $$wY = \frac{\Sigma w_i y_i}{\Sigma w_i}$$

(2.19) $$S_{xx} = \Sigma(x_i - wX)^2$$

(2.20) $$S_{xy} = \Sigma\,(x_i - wX)\,(y_i - wY)$$

(2.21) $$Slope = \frac{S_{xy}}{S_{xx}}$$

(2.22) $$Intercept = wY - [Slope]wX$$

2.4.2 Bootstrapping

The bootstrap resample technique was introduced in 1979 (Efron, 1979). The method is used to calculate the sampling distribution of an estimator by re-sampling from the original dataset to create multiple datasets.

Bootstrapping is used after the LOWESS technique is applied to the data by re-sampling from a normal distribution at every data point where the mean equals the measured value and the standard deviation fixed as the mean standard deviation of the residuals to the LOWESS fit. This is repeated 1000 times to create 1000 randomized data sets. LOWESS is then applied to each data set and a 95% confidence interval is then determined at each data point. The technique has been applied by numerous research groups to find the uncertainty in trends derived from data (Dlugokencky et al. 2001; Rice et al. 2016).

The bootstrap technique is also used to quantify the uncertainty in $\delta^{15}N$, $\delta^{15}N^{\alpha}$, $\delta^{15}N^{\beta}$, and $\delta^{18}O$ values numerically calculated from ^{45}R, ^{46}R, and ^{31}R (Potter et al. 2013).

The procedure calculates 1000 re-sampled values from a normal distribution with mean and standard deviation equal to the measured R values for each sample.

Chapter 3

Results of Mole Fraction Analysis

This chapter discusses the characterization of the gas chromatography system and the results of archive N_2O and SF_6 mole fraction measurements. Precision and reproducibility of the GC system are discussed in 3.1 followed by an explanation of how we addressed linearity in the detector response in section 3.2. N_2O and SF_6 mole fraction results are discussed in section 3.3.

3.1 GC precision and reproducibility

The precision of the gas chromatography measurement is determined by comparing residuals from sets of 6 reference gas measurements. Histogram distributions in figure 3.1 show 180 residuals (expressed as a percent relative standard deviation) collected from 30 sets of 6 measurements for N_2O (Fig. 3.1a) and SF_6 (Fig. 3.1b) mole fraction. The black dashed lines represent normal distribution curves with mean (μ) and standard deviation (σ) equal the residual dataset. Typical 1σ precision from a set of 6 measurements for N_2O and SF_6 is 0.16% and 1.13%, respectively. This corresponds to an uncertainty of 0.52 ppb for N_2O and 0.10 ppt for SF_6 for a measured concentration of 328.71 ppb and 8.76 ppt for N_2O and SF_6, respectively.

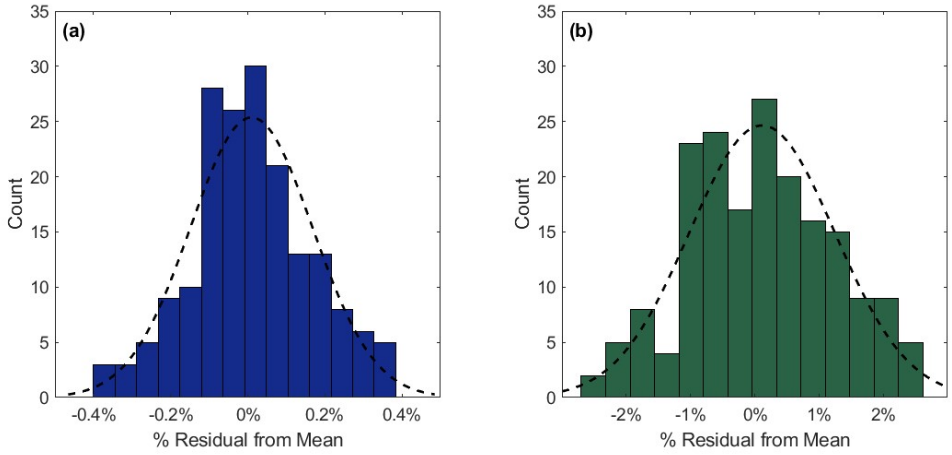

Figure 3.1. Percent Relative Distribution of 180 residuals from 30 sets of 6 measurements for N_2O (a) and SF_6 (b). Black dashed lines represent a normal distribution curve with the same mean and standard deviation as distributions. For N_2O, μ = 0.010% and 1σ = 0.16%. For SF_6, μ = 0.11% and 1σ = 1.13%.

Measurement reproducibility was evaluated by repeatedly measuring an air sample (CC2854, Breathing Air, Airgas, Radnor, PA) against the reference gas and

evaluating consistency from the standard deviation of the results. Figure 3.2 shows the results of 18 discrete measurements of N_2O (Fig. 3.2a) and SF_6 (Fig. 3.2b) from the dry air sample (CC2854) completed over two weeks. Error bars are combined uncertainty, representing the uncertainty in both the sample (n = 6) and reference gas (n = 12) measurements. The standard deviation in the N_2O and SF_6 measurements is 0.46 ppb (0.12%) and 0.11 ppt (0.8%) respectively (red dotted lines), which is ~1σ for a set of 6 standard measurements.

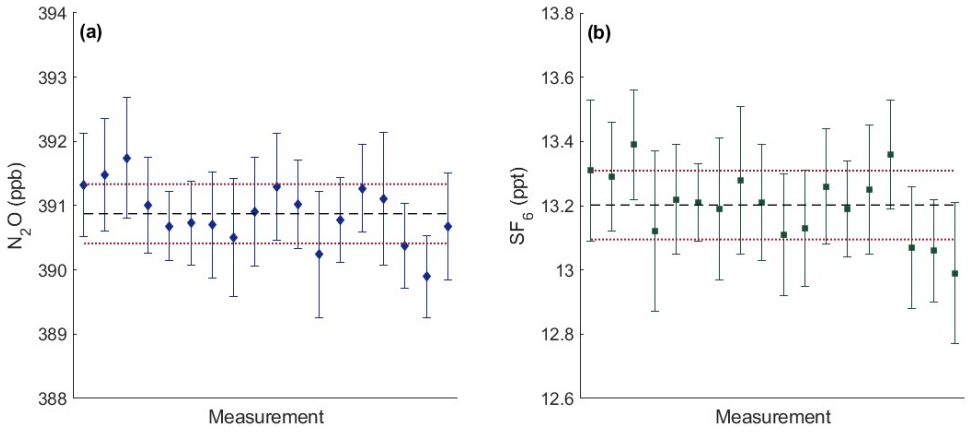

Figure 3.2. Measurement reproducibility for N_2O (a) and SF_6 (b) from 18 discrete measurements of a dry air sample made over a two week period. Error bars are combined uncertainty from sample and surrounding reference gas measurements. Black dashed and red dotted lines are mean and standard deviation, respectively. N_2O mean and standard deviation are 390.87 ppb and 0.46 ppb (0.12% RSD), respectively. SF_6 mean and standard deviation are 13.20 ppt and 0.11 ppt (0.8% RSD), respectively.

3.2 GC response linearity

To ensure accurate results in archive samples for this work, it is important to correctly characterize the detector response over the mole fraction range measured. The range in northern hemisphere N_2O mole fraction between 1978 and 1997 is between 295

and 314 ppb, or roughly an increase of 7% in 20 years (Prinn et al. 2000; Ciais et al. 2013). Northern hemisphere SF_6 mole fraction in the late 1970s is expected to be below 1 ppt based off results from Rigby et al. (2010) and rise to nearly 4 ppt in 1997. This is similar to southern hemisphere measurements from Cape Grim, Tasmania, where the range measured is from below 1 to just under 4 ppt over the same period (Levin et al. 2010; Rigby et al. 2010; Hall et al. 2011).

A series of manometric dilutions were prepared from the NOAA reference gas at Portland State University to evaluate the μECD response over historical N_2O and SF_6 mole fraction sample range. Electropolished stainless steel canisters (Summa, 3 L) were connected to a vacuum system and evacuated to <1 Pa. To characterize the N_2O response, ultra-pure air (zero grade, Airgas, Portland, OR) confirmed to have N_2O and SF_6 concentrations below detection limits was used as a dilution gas and measured monometrically using capacitance manometers (MKS Instruments, Andover, MA) with a precision of ± 13 Pa (0.1 torr). The range of N_2O concentrations produced in 3 L canisters was 32.2 - 321.4 ppb. Error introduced from the manometric process is small (maximum 1σ error of ± 0.07 ppb for N_2O) when compared to measurement uncertainty.

To characterize the SF_6 response, it is necessary to consider the interference caused by the N_2O peak in the chromatogram output. To properly account for this interference, SF_6 at low concentrations (0.6 - 6.0 ppt) must have a N_2O peak that reflects expected concentrations in archived samples (~300 ppb). Prepared dilutions of SF_6 included an aliquot of 1 ppm N_2O (± 5%) balanced with He (Scott Specialty Gases, St. Louis, MO) into the canister prior to dilution with ultra-pure air. A high precision capacitance manometer (MKS Instruments, Andover, MA) with a precision of ± 0.13 Pa

(0.001 torr) monitored the introduction of the 1 ppm N_2O. The maximum 1σ error in SF_6 introduced from the manometric process is small (0.001 ppt) compared to measurement uncertainty. However, if the 1 ppm N_2O aliquot or ultra-pure air contains SF_6 below our detection limits (~0.1 ppt), this would contribute to uncertainty in the prepared samples. All dilution samples were measured at PSU on the GC-μECD system over several weeks to account for instrument drift. Table 3.1 provides dilution sample pressures, expected and observed μECD response, and measured N_2O mole fractions with the error in measurement used to characterize the N_2O linearity. Table 3.2 provides dilution sample pressures, expected and observed μECD response, and measured SF_6 mole fractions with the error in measurement used to characterize the SF_6 linearity.

Table 3.1. Manometrically prepared standards for N_2O linearity.

Canister ID	[a.] P_{Ref} (torr)	[b.] P_{Total} (torr)	[c.] Expected N_2O Response	[d.] Measeured N_2O Response	[e.] Measured N_2O (ppb)	[f.] N_2O 1σ (ppb)
1.7	727.3	992.7	0.7327	0.7673	252.21	0.78
1.14	274.4	991.6	0.2767	0.3262	107.22	0.45
1.5	461.2	996.7	0.4627	0.5157	169.52	0.51
2.14	157.6	994.4	0.1585	0.1941	63.79	0.27
2.7	97.2	993.4	0.0978	0.1239	40.73	0.44
2.5	604.0	991.3	0.6092	0.6535	214.80	0.52
3.7	952.3	996.2	0.9559	0.9618	316.15	0.83
3.5	877.8	996.1	0.8813	0.8981	295.20	0.87
3.14	928.2	995.3	0.9326	0.9423	309.75	0.85
4.5	973.0	995.1	0.9778	0.9813	322.56	0.96
4.14	893.1	996.9	0.8959	0.9085	298.62	0.71
4.7	907.0	993.5	0.9129	0.9226	303.26	0.80
NOAA Ref	-	-	1.0000	1.0000	328.71	0.52

a. P_{Ref} is the NOAA reference gas pressure (in torr) introduced to the canister.

b. P_{Total} is the final pressure (in torr) of the canister after balancing with ultra-pure air.

c. Expected response is calculated from the P_{Ref}/P_{Final} fraction.

d. Measured N_2O response of the μECD.

e. Measured N_2O in ppb.

f. N_2O 1σ (ppb) is from combined uncertainty of sample and surrounding NOAA reference.

Table 3.2. Manometrically prepared standards for SF_6 linearity.

Canister ID	[a.] P_{Ref} (torr)	[b.] P_{Scotty} (torr)	[c.] P_{Total} (torr)	[d.] Expected SF_6 Response	[e.] Measured SF_6 Response	[f.] Measured SF_6 (ppt)	[g.] SF_6 1σ (ppt)
1.14	727.4	-	992.8	0.7327	0.7476	6.55	0.12
3.5	877.9	-	996.2	0.8812	0.8943	7.83	0.24
3.14	928.3	-	995.4	0.9326	0.9414	8.25	0.10
1.1	221.9	232.8	994.9	0.2230	0.2443	2.14	0.06
1.18	89.4	276.7	997.5	0.0896	0.1199	1.05	0.07
1.28	66.9	282.4	992.5	0.0674	0.1153	1.01	0.06
2.1	140.3	261.1	989.3	0.1418	0.1644	1.44	0.08
2.18	569.2	119.9	991.7	0.5740	0.5879	5.15	0.15
2.28	396.7	176.1	991.2	0.4002	0.4110	3.60	0.12
NOAA Ref	-	-	-	1.0000	1.0000	8.76	0.10

a. P_{Ref} is the NOAA reference gas pressure (in torr) introduced to the canister.

b. P_{Scott} is the 1 ppm N_2O balanced with He (in torr) introduced to the canister.

c. P_{Total} is the final pressure (in torr) of the canister after balancing with ultra-pure air.

d. Expected SF_6 response is calculated from the P_{Ref}/P_{Final} fraction.

e. Measured SF_6 response of the μECD.

f. Measured SF_6 in ppt.

g. SF_6 1σ (ppt) is from combined uncertainty of sample and surrounding NOAA reference.

A visual representation of the detector response linearity for N_2O over the full range of manometricly prepared standards is shown in figure 3.3, displaying measured difference from expected (measured - expected) mole fraction plotted against expected mole fraction. The black line is a 3rd degree polynomial fit. The red dashed line is a linear fit to the last 7 data points, which span the N_2O concentration range in the archive. Error bars are total measurement uncertainty. R^2 for the poly-3 fit is 0.9976.

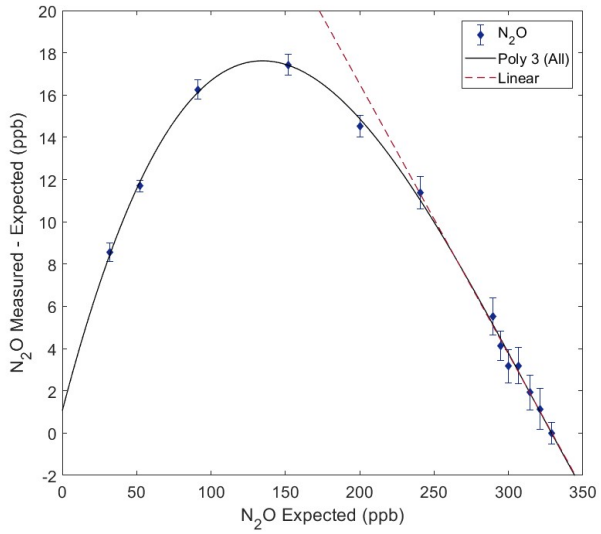

Figure 3.3. N_2O measured difference from expected over the full range of manometrically prepared standards. Black fit curve is a 3rd degree polynomial. Red dashed line is a linear fit to the standards that span the archive range. Error bars are total measurement uncertainty.

The 3rd degree polynomial equation is:

(3.1) $f(x) = a_1x^3 + a_2x^2 + a_3x + a_4$

(3.2) $a_1 = 1.36e\text{-}06 \pm 4.18e\text{-}07$ (95% CI)

(3.3) $a_2 = -1.28e\text{-}03 \pm 2.32e\text{-}04$ (95% CI)

(3.4) $a_3 = 0.2707 \pm 0.0368$ (95% CI)

(3.5) $a_4 = 1.063 \pm 1.489$ (95% CI)

The results for N_2O show that as the prepared standard concentrations become smaller, the measured difference from expected increases until the sample is ~200 ppb smaller than the reference (328.71 ppb), where the maximum deviation in measurement is 17.6 ppb. After this point, the measured deviation from expected begins to decrease. While it is not necessary to characterize the detector response over this full range for the archive measurements, the 3rd degree polynomial fit would be needed if measuring N_2O

concentrations that have a large difference (80 ppb or greater) to reference gas. Figure 3.4 displays the measured versus expected concentration for standards that better span the N_2O archive concentrations (285 – 330 ppb).

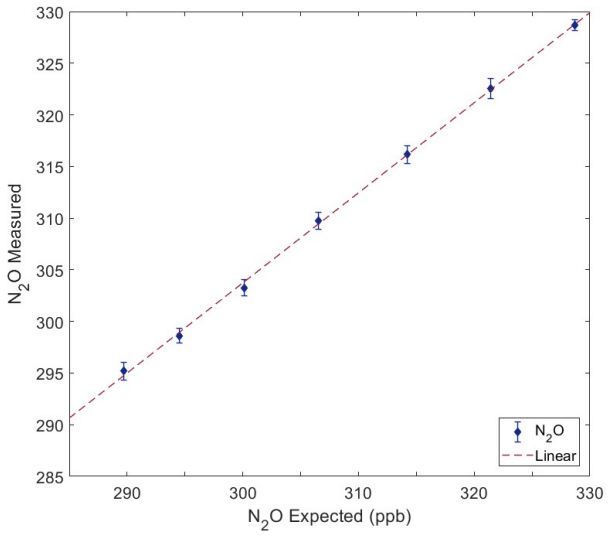

Figure 3.4. μECD N_2O response for manometrically prepared standards over the archive range. Red dashed line is a linear fit to the standards that span the archive range. Error bars are total measurement uncertainty.

The response is linear over the archive range with a slope of 0.8747 ± 0.028 (95% CI) and R^2 value of 0.999. This results in a deviation from expected of ~0.14 ppb ppb^{-1} difference from the reference when measuring samples. All N_2O samples are adjusted for a linearity correction of the form:

(3.6) $$[N_2O]_X = b_1 * [N_2O]_Y + b_2$$

(3.7) $$b_1 = 1.143 \pm 0.037 \text{ (95\% CI)}$$

(3.8) $$b_2 = -47.24 \pm 11.49 \text{ (95\% CI)}$$

Where $[N_2O]_X$ is the corrected mole fraction and $[N_2O]_Y$ is the measured mole fraction. While not explicitly stated, a similar non-linear response is reported in the data of Hall et al. (2007) with a deviation from expected of ~0.18 ppb ppb^{-1} difference from the reference when measuring N_2O.

Detector response non-linearity is also characterized for SF_6. Figure 3.5 displays the measured deviation from expected (measured - expected) mole fraction plotted against expected mole fraction. The black line is a 3rd degree polynomial fit and the red dashed line is a linear fit to the measurements. Error bars are total measurement uncertainty. The maximum difference between the Poly 3 fit and the linear fit over the range in the prepared standards is ~ 0.10 ppt.

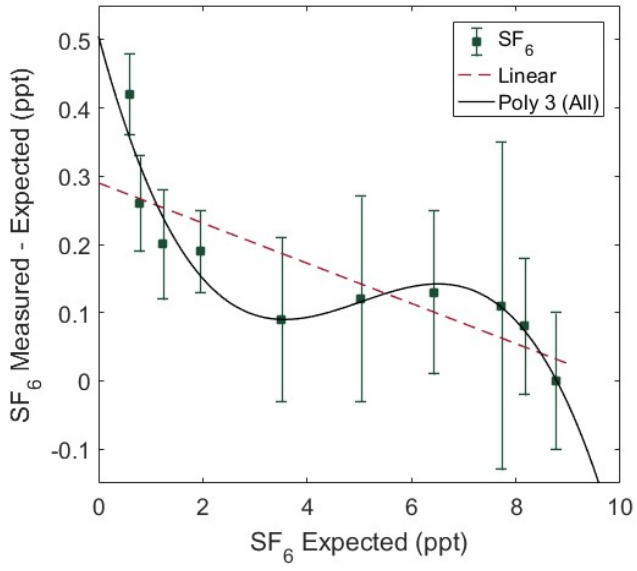

Figure 3.5. SF_6 measured difference from expected over the full range of manometrically prepared standards. Black fit curve is a 3rd degree polynomial. Red dashed line is a linear fit to the standards. Error bars are total measurement uncertainty.

The 3rd degree polynomial equation is:

(3.9) $f(x) = c_1x^3 + c_2x^2 + c_3x + c_4$

(3.10) $c_1 = -0.004096 \pm 0.002689$ (95% CI)

(3.11) $c_2 = 0.06187 \pm 0.03788$ (95% CI)

(3.12) $c_3 = -0.285 \pm 0.1481$ (95% CI)

(3.13) $c_4 = 0.5052 \pm 0.6396$ (95% CI)

The SF_6 calibration curve shows there is an immediate deviation from expected as the SF_6 concentration decreases until near 6.5 ppt (~ 2.2 ppt difference from the NOAA standard with a measurement deviation of ~ 0.14 ppt) where the deviation begins to decrease slightly. At ~ 3.7 ppt (~5 ppt difference from the NOAA standard), the deviation begins to increase again. This type of 3rd degree polynomial behavior of the detector response is not reported in previous ECD linearity characterizations (Leven et al. 2010). The shape of the curve is likely due to the peak integration methods used in the analysis of the chromatograms. While the linear fit has a relatively large (~0.1 ppt) difference compared to the 3rd degree polynomial fit when the expected concentration is at 0.6 ppt and ~ 3.0 ppt, 1σ error bars of data points overlap with the linear model. This suggests differences between the 3rd degree polynomial correction and linear correction are near measurement precision.

Figure 3.6 shows the measured concentration versus expected concentration for SF_6 in ppt for the prepared standards. The slope of the SF_6 linear fit is 0.9728 ± 0.017 (95% CI) with R^2 of 0.9995. This results in a deviation from expected of ~0.03 ppt ppt^{-1} difference from the reference gas when measuring samples. All SF_6 measurements are adjusted for a linearity correction of the form:

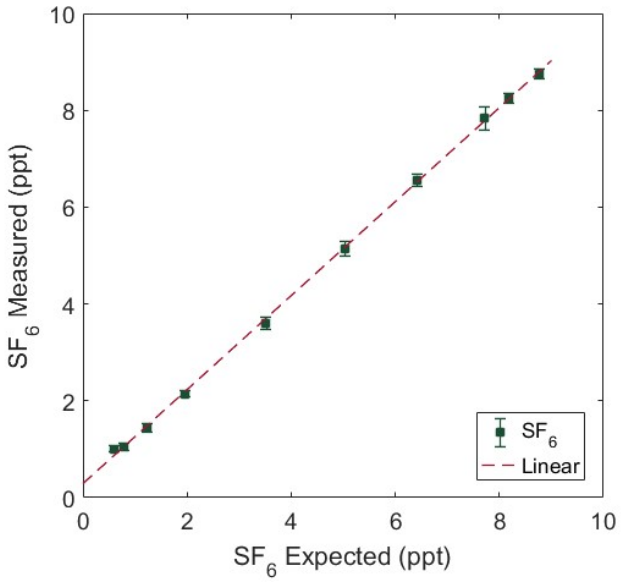

Figure 3.6. μECD SF_6 response for manometrically prepared standards. Red dashed line is a linear fit to the standards. Error bars are total measurement uncertainty.

(3.14) $[SF_6]_X = d_1 * [SF_6]_Y + d_2$

(3.15) $d_1 = 1.03 \pm 0.018$ (95% CI)

(3.16) $d_2 = -0.294 \pm 0.099$ (95% CI)

Where $[SF_6]_Y$ is the measured SF_6 mole fraction and $[SF_6]_X$ is the corrected value.

3.3 Air archive mole fraction results

The following subsections discuss the results of the mole fraction analysis from the air archive samples. Measurements of N_2O and SF_6 mole fraction from 159 samples from the Cape Meares archive (supplemental Table 1) were initially filtered for analysis using a 7 median absolute deviation (7MAD) noise filter to remove far outliers. Polynomial fits (1st degree for N_2O and 2nd degree for SF_6) were then applied to the data

sets. Residual values outside of 2σ for N_2O and 3σ for SF_6 were removed. The entire process removed 17 data points for N_2O and 4 data points for SF_6.

Seasonality is calculated from the residuals of observed data points to a LOWESS regression fit with a large smoothing window (33.3% of the data). Residuals are then plotted against their fractional date where a second LOWESS fit is applied using a 30 day smoothing window. Once the seasonality is established, the dataset is deseasonalized to remove intra-annual variability, then plotted against the collection date. A third LOWESS fit is applied using a 3-year smoothing window, which is used to find the annual trend. The trend is calculated by applying a SPLINE fit to the de-seasonalized LOWESS to interpolate a concentration for every month in a year. The first derivative of the SPLINE fit then provides a trend at monthly resolution. The process is completed for both N_2O and SF_6 datasets.

3.3.1 N_2O Seasonality

Figure 3.7 shows the seasonality observed as residuals to the secular trend for N_2O. The black line is the LOWESS fit to the residuals. Data points represent the average residual binned by month with error bars representing the standard error of the binned data within the month. The shaded region is the 95% CI in the LOWESS fit calculated from 1000 bootstrapped LOWESS fits after including observed variability in the residuals to the secular trend.

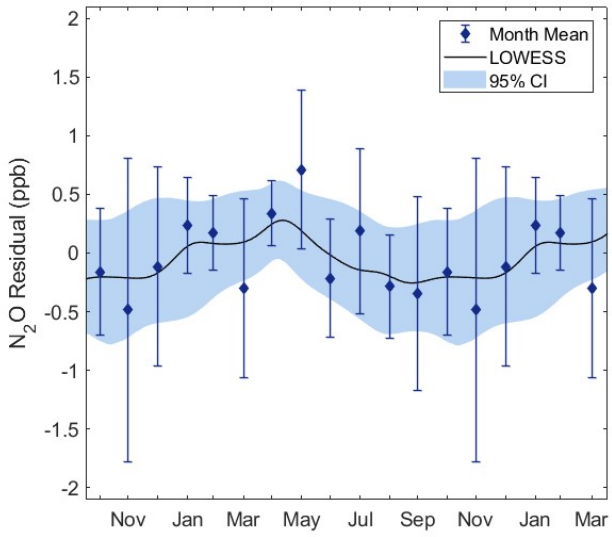

Figure 3.7. N_2O seasonality for Cape Meares, OR. Data points are mean monthly residuals with error bars equal to the standard deviation. Shaded region is 95% CI calculated from 1000 bootstrapped LOWESS regressions from observed variability.

N_2O seasonality shows peak amplitude near April of 0.34 ppb and a wide trough from September through November with a minimum of -0.42 ppb in late November. The 95% CI in the bootstrapped seasonality has the smallest range in April (± 0.3 ppb) and the largest range in November (± 0.7 ppb). Figure 3.8 shows seasonal QQ-plots of N_2O with Tables 3.1 and 3.2 providing statistical information binned by meteorological season.

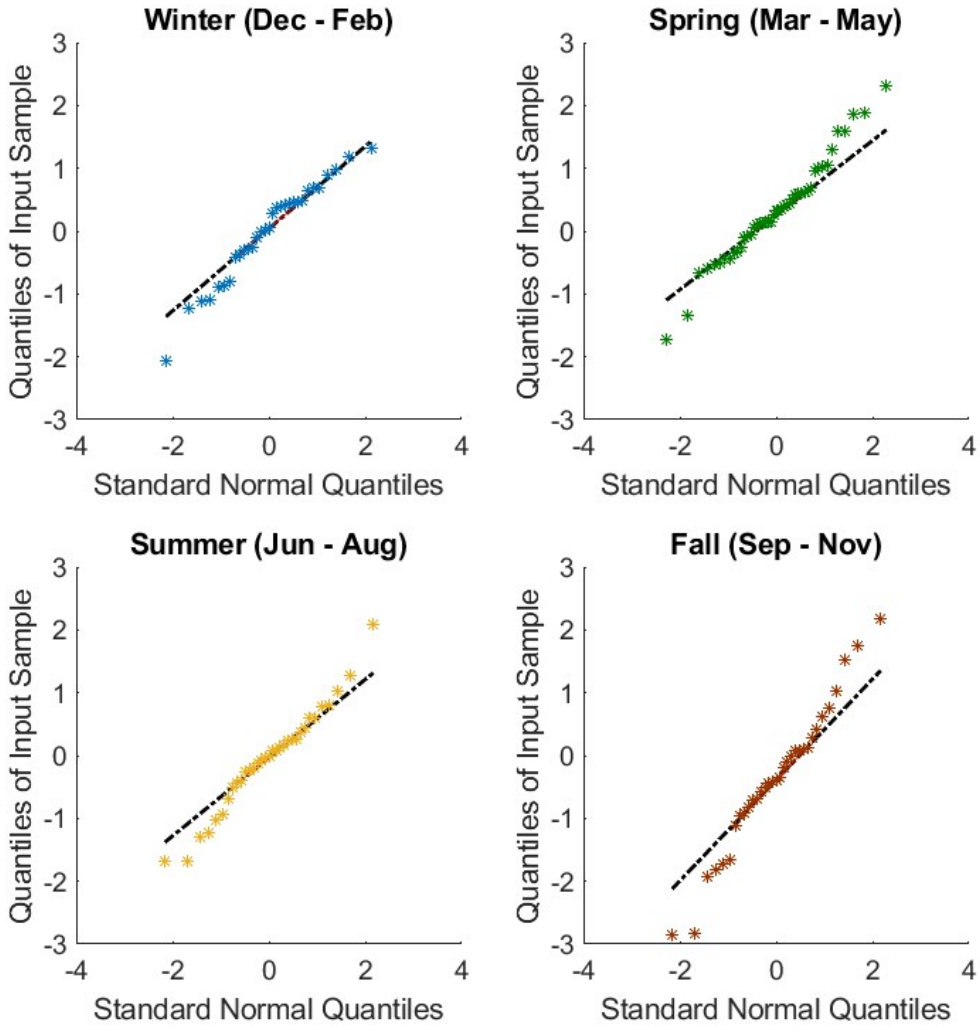

Figure 3.8. N_2O seasonal QQ-plots.

Table 3.3. N_2O seasonal statistics.

	Winter	**Spring**	**Summer**	**Fall**
Count	31	45	33	33
St. Dev. (ppb)	0.79	0.81	0.82	1.16
Mean (ppb)	0.00	0.33	-0.05	-0.37
χ^2 *p-value*	0.228	0.175	0.572	0.056

χ^2 is the chi-squared goodness of fit statistic that tests if the data comes from a normal distribution with the same mean and standard deviation.

Table 3.4. N_2O seasonal Kolmogorov-Smirnov test comparisons.

	Fall	*Summer*	*Spring*
Winter	0.199	0.428	0.528
Spring	0.003	0.126	
Summer	0.249		

Results of grouping the residual data points into seasonal bins is given in table 3.3. The standard deviation of the residuals is very similar for winter, spring, and summer at ~0.8 ppb. Fall however has a larger variation of 1.16 ppb. This is reflected in the larger 95% CI in the fall months in figure 3.7. The mean residual value in spring and fall is 0.33 ppb and -0.37 ppb, respectively. This matches well with the N_2O seasonality calculated from LOWESS regression.

The p-values in table 3.4 are Kolmogorov-Smirnov test statistics comparing the seasonal test statistics. A p-value of 0.05 suggests the two samples come from different distributions with 95% significance level. The only seasonal comparison that meets this threshold of significance is spring (peak) and fall (trough), with a p-value of 0.003. So, though there is considerable uncertainty in N_2O seasonality, the spring maximum is statistically different from the fall minimum at high levels of confidence.

Previously reported northern hemisphere seasonality in N_2O mole fraction has similar amplitude and phase compared to Cape Meares (figure 3.7) at comparable observational sites. N_2O seasonality reported at Mace Head, Ireland has a peak near April and a trough near August/September (Nevison et al. 2004; Jiang et al. 2007; Nevison et al. 2007). Trinidad Head, CA seasonality has a maximum near late May, but no local minimum near any single month (Nevison et al. 2007). The mean magnitude reported for

the northern hemisphere is ± 0.4 ppb (Liao et al. 2004), comparable with the Cape Meares record.

3.3.2 Annual N_2O mole fraction

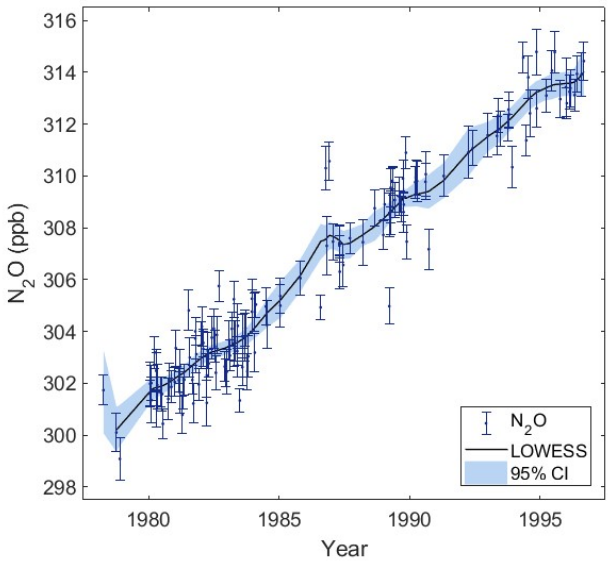

Figure 3.9. Deseasonalized measurements of N_2O mole fraction versus date of collection. Error bars are total measurement uncertainty. Solid black line is the LOWESS fit to the data using a smoothing window of 3 years. Shaded region is 95% confidence interval in the LOWESS fit calculated from bootstrapping the observed residuals 1000 times.

Figure 3.9 shows the deseasonalized N_2O mole fraction plotted against the collection date. In 1980, the N_2O mole fraction is 301.5 ± 0.6 ppb. The concentration increases roughly linearly to 313.5 ± 0.6 ppb in 1996. These observations match well with previously published measurements of N_2O from Cape Meares during the same period (Prinn et al. 1990; Prinn et al. 2000; Khalil et al. 2002).

Measurements by the Advanced Global Atmospheric Gases Experiment (AGAGE) on the SIO-98 N_2O scale and NOAA/ESRL on the NOAA-06 N_2O scale are reported from comparable sample locations. Trinidad Head, CA (41° N, 121° W), Mace Head, Ireland (53° N, 10° W), and Niwot Ridge, CO (40° N, 106° W) all measure ~313 ppb in 1996. The difference between the SIO-98 and NOAA-06 N_2O scales is negligible at the concentrations measured here (Hall et al. 2007). These measurements are within the range of Cape Meares measurements reported here and suggest that the N_2O in the archived samples has stored well.

3.3.3 N_2O Trend

The mean secular trend between 1978 and 1996 for N_2O is 0.78 ± 0.03 ppb yr^{-1} (95% CI), calculated by applying a linear fit to deseasonalized N_2O mole fraction data. The annual trend for N_2O at Cape Meares, Oregon is shown in figure 3.10. The plot is created by finding the trend in time for 1000 bootstrapped datasets. Data points represent the mean year trend with error bars equal to one standard deviation of the trend over the year.

An indistinguishable secular trend of 0.74 ± 0.02 ppb yr^{-1} is reported between 1978 and 1998 for Cape Meares (Prinn et al. 2000). The global trend of N_2O between 1985 and 1996 reported by Khalil et al. (2002) is 0.69 ± 0.03 ppb yr^{-1}, also compatible with the trend determined here for Cape Meares. The 95% confidence in the annual trend in the early 1980s is ± 0.15 ppb yr^{-1}, where a large concentration of data points is located (~50% of samples are between 1980 and 1985). After 1985, the 95% confidence in the annual trend becomes roughly ± 0.5 ppb yr^{-1}.

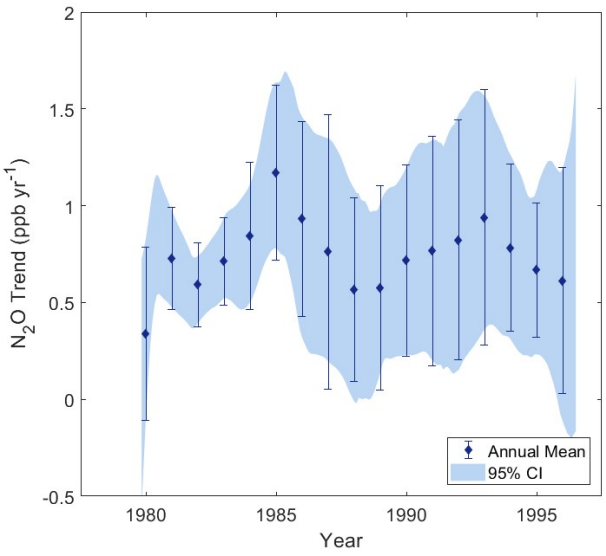

Figure 3.10. N_2O trend in time. Mean annual trend is shown with error bars representing 1σ of the trend over the year. Shaded areas represent 95% confidence interval calculated from the standard deviation of 1000 bootstrapped residual uncertainties to the observed data.

3.3.4 SF_6 Seasonality

Figure 3.11 shows the seasonality in SF_6 calculated from the Cape Meares data. The black line is the LOWESS fit to residuals from the secular trend. Data points represent the average residual binned by month with error bars representing the standard error of the binned data within the month. The shaded region is the 95% CI in the LOWESS fit calculated from 1000 bootstrapped LOWESS fits after including observed variability in the residuals to the secular trend.

SF_6 seasonality has a maximum between December and February of 0.04 ppt and a minimum near July of -0.03 ppt. The 95% CI of the LOWESS regression is smallest in

April (± 0.03 ppt) and largest in November (± 0.06 ppt). Figure 3.12 shows seasonal QQ-plots of SF_6 with tables 3.3 and 3.4 providing statistical information about each season.

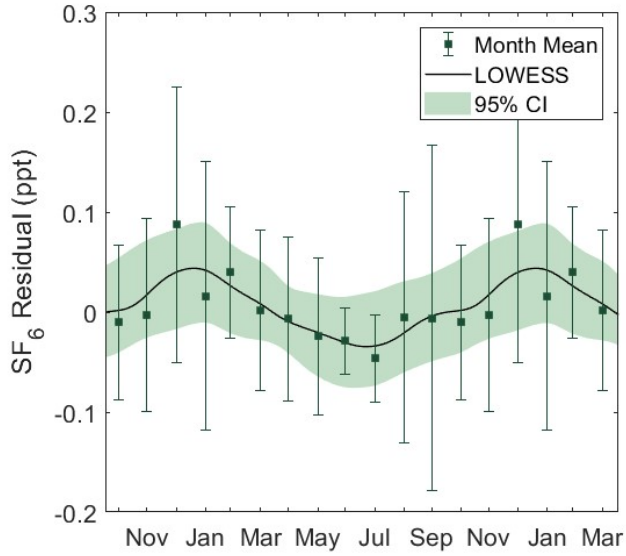

Figure 3.11. SF_6 seasonality for Cape Meares, OR. Data points are mean monthly residuals with error bars equal to the standard deviation. Shaded region is 95% CI of the LOWESS calculated from 1000 bootstrapped LOWESS fits after including measurement uncertainty.

Results of grouping the residual data points into seasonal bins is given in table 3.5. The standard deviation is largest for the winter and fall seasons and smallest during the summer season. This is reflected in the bootstrapped 95% CI in figure 20. The maximum mean residual occurs during the winter season at 0.05 ppt with the minimum during the summer at -0.04 ppt. This matches well with the LOWESS seasonality in figure 3.11.

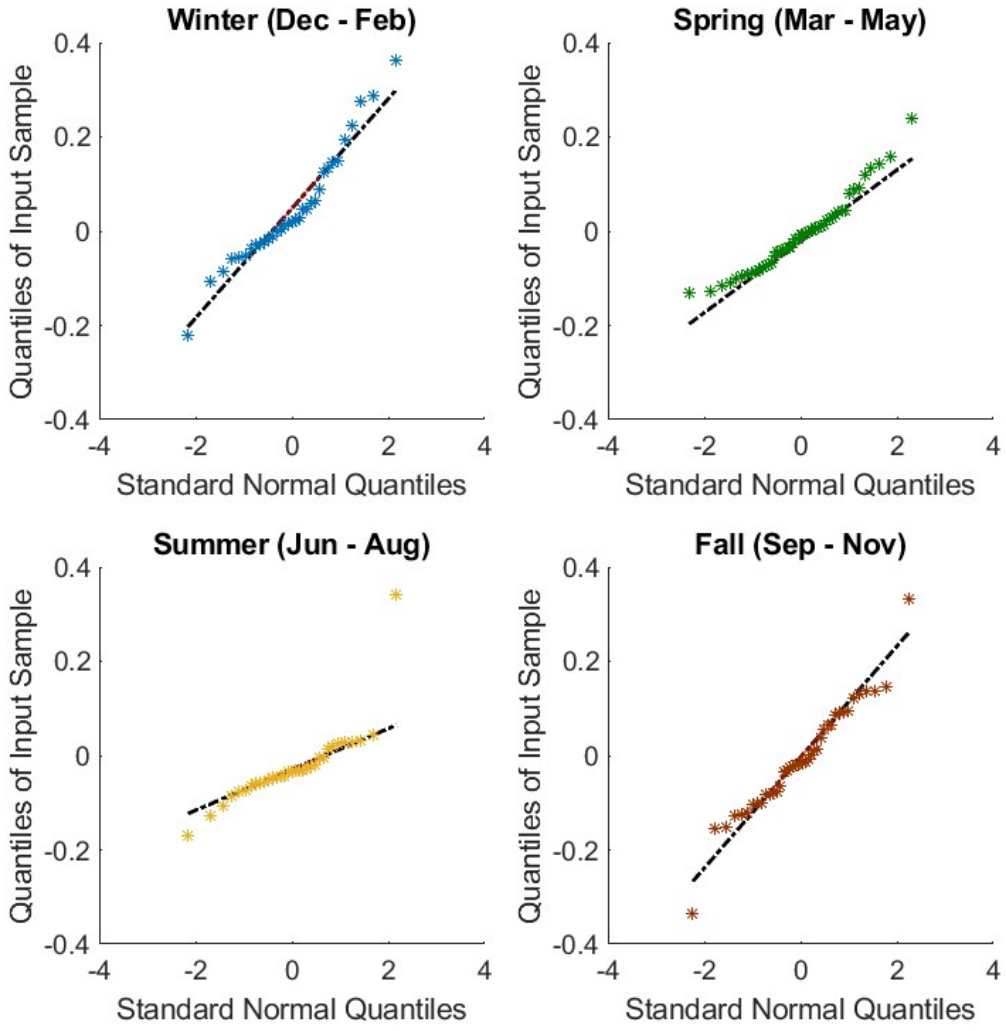

Figure 3.12. SF_6 seasonal QQ-plots.

Table 3.5. SF_6 seasonal statistics.

	Winter	**Spring**	**Summer**	**Fall**
Count	33	49	32	40
Stdev (ppt)	0.12	0.08	0.05	0.12
Mean (ppt)	0.05	-0.01	-0.04	-0.01
χ^2 *p-value*	0.062	0.405	0.059	0.152

Here, χ^2 is the chi-squared goodness of fit statistic that tests if the data comes from a normal distribution with the same mean and standard deviation.

Table 3.6. SF_6 seasonal Kolmogorov-Smirnov test comparisons.

	Fall	*Summer*	*Spring*
Winter	0.149	0.004	0.114
Spring	0.573	0.099	
Summer	0.036		

The p-values in table 3.6 are Kolmogorov-Smirnov test statistics comparing seasonal test statistics. A p-value of 0.05 suggests the two samples come from different distributions at the 95% significance level. From table 3.6, there is high statistical confidence in the difference between summer and winter SF_6 residual values. The summer and fall comparison also suggests there is a statistically significant difference between the seasons, though the means of each season are similar (-0.04 ppt in summer and -0.01 ppt in fall).

Some northern hemisphere observations of SF_6 seasonality have been reported in the literature. Barrow, AK has a minimum in September and October with a broad maximum from December to June (Patra et al. 2009). Alert, Canada shows a strong minimum in October, though a maximum is not clearly defined (Wilson et al. 2014). Continental sites such as Niwot Ridge show large influences from interannual variability (IAV) and have little distinguishable seasonality (Patra et al. 2009).

The SF_6 seasonality at Cape Grim has been reported to have amplitude of ± 0.01 ppt with a maximum in September and October and a minimum in near February (Nevison et al. 2007; Wilson et al. 2014). The seasonality phase of Cape Grim is nearly anti-phase of Cape Meares reported here, though the scale is a factor of 4 smaller at Cape Grim. Similar to N_2O, seasonal amplitude is expected to be larger in the northern

hemisphere than in the southern hemisphere due to transport (Jiang et al. 2007; Nevison et al. 2007).

3.3.5 Annual SF_6 mole fraction

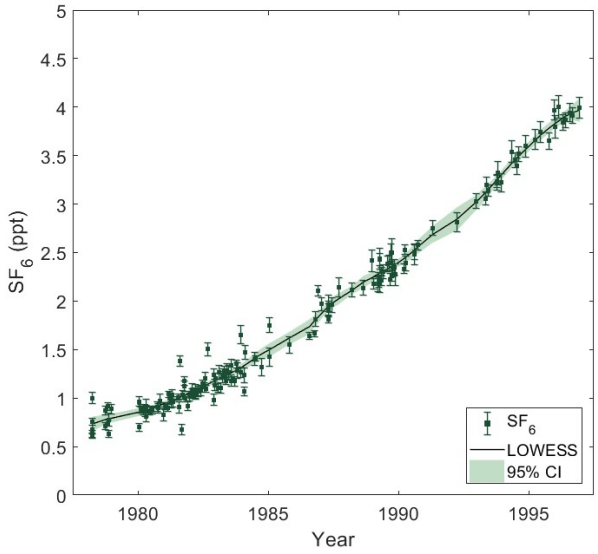

Figure 3.13. Deseasonalized measurements of SF_6 mole fraction versus date of collection. Error bars are total uncertainty. Solid black line is the LOWESS fit to the data using a smoothing window of 3 years. Shaded region is 95% confidence interval in the LOWESS fit calculated from bootstrapping observed residuals 1000 times.

Figure 3.13 shows SF_6 mole fraction plotted against the collection date of the sample for 155 samples. The SF_6 concentration is measured to be 0.85 ± 0.03 ppt (1σ) in 1980 and increases to a concentration of 3.83 ± 0.03 ppt (1σ) in 1996. Cape Meares does not have previously reported measurements of SF_6 to compare with directly.

Measurements of SF_6 from Trinidad Head, CA are reported to be ~0.85 ppt in 1980 and ~3.73 ppt in 1996 on the SIO-2005 SF_6 scale (Rigby et al. 2010). A conversion

factor of 0.9991 is used to convert from the SIO-2005 SF_6 scale to the NOAA-06 SF_6 scale (Hall et al. 2014). In 1996, values of 3.87 ppt, 3.87 ppt, and 3.78 ppt are reported for Alert, Canada (82° N, 62° W), Barrow, AK (71° N, 157° W), and Niwot Ridge, CO respectively on the NOAA-06 SF_6 scale (Hall et al. 2011). The scale difference shifts values by +0.01 ppt to -0.05 ppt when converting from NOAA-06 to NOAA-14. Cape Meares SF_6 measured values match well with these comparable sample locations.

Southern hemisphere measurements of SF_6 from archived atmospheric samples from Cape Grim, Tasmania (41° S, 145° E) and Neumayer, Antarctica (70° S, 8° W) are ~0.6 – 0.7 ppt in 1980 and ~3.4 – 3.5 ppt in 1996 on SIO-2005 and University of Heidelberg SF_6 scales (Levin et al. 2010, Rigby et al. 2010). As with the SIO-2005 SF_6 scale, the NOAA-06 and University of Heidelberg scale differences are small. To convert to the NOAA-06 SF_6 scale, values measured on the University of Heidelberg SF_6 scale are divided by a conversion factor of 0.9954 (Hall et al. 2014). Including a scale correction, Cape Meares SF_6 measurements are higher than Cape Grim and Neumayer during this period by 0.2 - 0.4 ppt. Much or all of this difference can be explained by an interhemispheric north-south difference of 0.3 – 0.4 ppt (Levin et al. 2010).

3.3.6 SF_6 Trend

The secular trend between 1978 and 1996 for SF_6 is 0.17 ± 0.01 ppt yr^{-1} (95% CI), calculated by applying a linear fit to the deseasonalized data. The annual trend for SF_6 at Cape Meares, Oregon is shown in figure 3.14. Data points represent the mean annual trend with error bars equal to one standard deviation of the trend over the year.

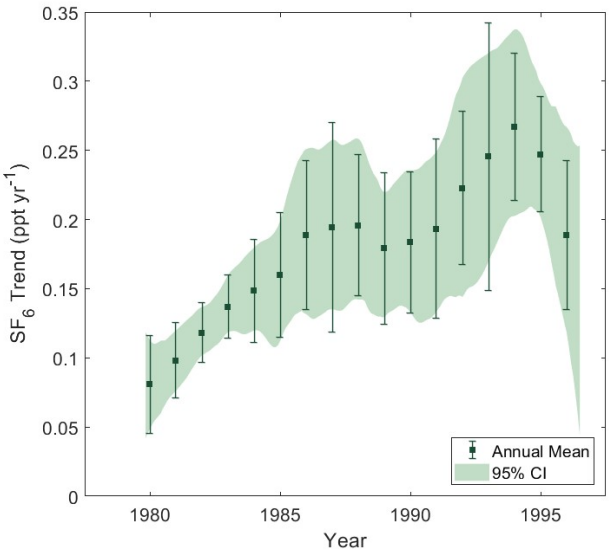

Figure 3.14. SF_6 annual trend. Mean yearly trend is shown with error bars representing 1σ of the trend over the year. Shaded areas represent 95% CI calculated from the standard deviation of 1000 bootstrapped residual uncertainties to the observed data.

The SF_6 annual trend increases from 0.08 ppt yr^{-1} in 1980 to 0.26 ppt yr^{-1} in 1994. The average rate of change in the growth rate (second derivative of mole fraction vs. time) over this period is 0.014 ppt yr^{-2}. The increase in growth rate over this period is statistically significant at high levels of confidence (95%). After 1994, we measure a decrease in the growth rate, though this decline is not statistically significant at high levels of confidence over this short time interval.

Comparable trends in SF_6 measured at other locations are available for the mid-1990s. The average global growth rate of SF_6 in 1994 was reported at 0.23 ppt yr^{-1} in the northern hemisphere (Maiss et al. 1996). Alert, Canada and Izaña, Tenerife are observed to have maximum trends of 0.26 ppt yr^{-1} in mid-1994 and at the beginning of 1995 (Levin et al. 2010), respectively, compatible with results presented here. The localized maximum

in growth rate in 1994 observed here is present in some southern hemisphere observations of SF_6 at a similar time as well; Neumayer, Antarctica shows a maximum trend in 1995-1996 of 0.25 ppt yr^{-1} (Levin et al. 2010). This finding is consistent with a peak in SF_6 emissions as reported by the European Database for Global Atmospheric Research (EDGAR, v4.2).

Another feature observed in the SF_6 trend from Cape Meares is a local maximum in the growth rate near 1987. Notably however, not all data sets agree. The growth rate reported from Neumayer, Antarctica has this feature during a similar period (Levin et al. 2010), but the trend reported at Cape Grim, Tasmania does not show this local maximum (Rigby et al. 2010). Due to the large uncertainty from the few archived samples available during that time period, this local maximum is not statistically distinguishable from surrounding years at high levels of confidence in the Cape Meares analysis and this result is merely suggestive. Additional evidence is needed to corroborate this finding.

Chapter 4

Results of Isotopic Analysis

This chapter discusses the results from method development using IRMS and from the isotopic analysis of the OHSU-PSU air archive. Measurement precision and reproducibility are presented in section 4.1 followed by an analysis of the theoretical maximum precision of the system in 4.2. The measurement dependence on sample size is presented in 4.3. Section 4.4 discusses the methods used to determine the scrambling coefficient and the results. Precision in the isotopic composition is presented and discussed in section 4.5. In section 4.6, results of the isotopic analysis of the OHSU-PSU air archive are presented.

4.1 IRMS precision and reproducibility

Measurements made on the IRMS are completed in duplicates or triplicates. Precision of measurement is determined by compiling residuals of these replicate measurements. Table 4.1 gives statistical information about the measurement precision of δ^{45}, δ^{46}, and δ^{31} of the working standard CC2854 (Breathing Air, Airgas, Radnor, PA) while histograms of measurement residuals are shown in figures 4.1 – 4.3. The results show that the residual distributions are normal with typical 1σ measurement precision of 0.05‰, 0.10‰, and 0.28‰ for δ^{45}, δ^{46}, and δ^{31}, respectively. The chi-squared statistic suggests the distributions are not statistically different from a normal distribution at high levels of confidence.

Table 4.1. IRMS measurement precision of the working standard CC2854.

Category	**δ^{45}**	**δ^{46}**	**δ^{31}**
Count	178	178	186
Mean (‰)	0.00	0.00	0.00
Stdev (‰)	0.05	0.10	0.28
χ^2 *p-value*	0.1	0.2	0.6

χ^2 is the chi-squared goodness of fit statistic that tests if the data comes from a normal distribution with the same mean and standard deviation.

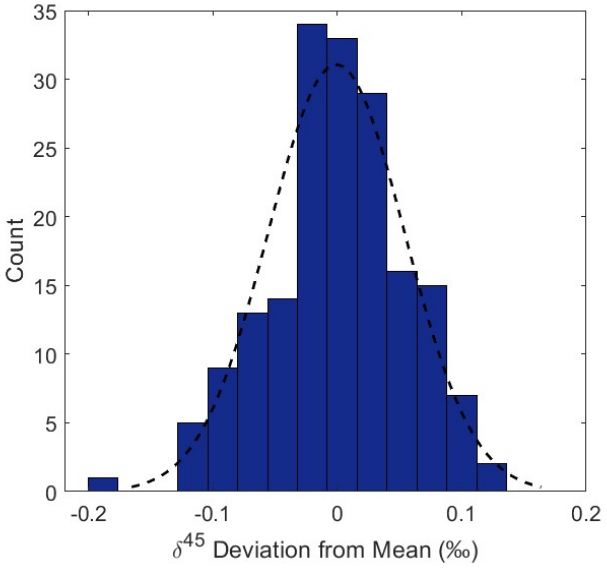

Figure 4.1. δ^{45} precision from 178 measurements of a whole air sample, 1σ = 0.05‰.

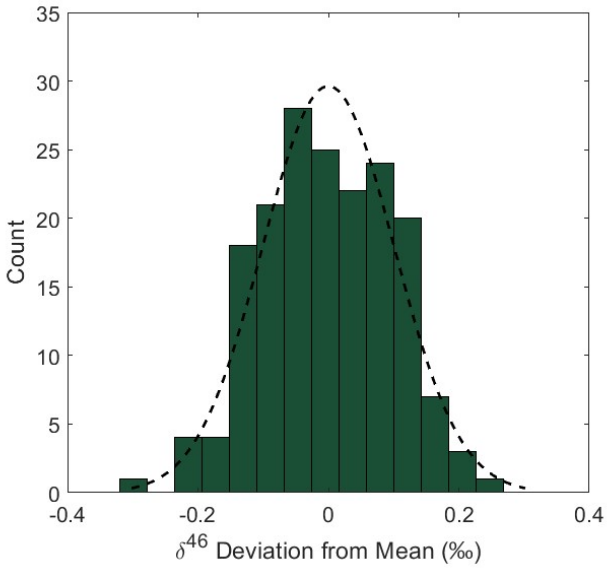

Figure 4.2. δ^{46} precision from 178 measurements of a whole air sample, 1σ = 0.10‰.

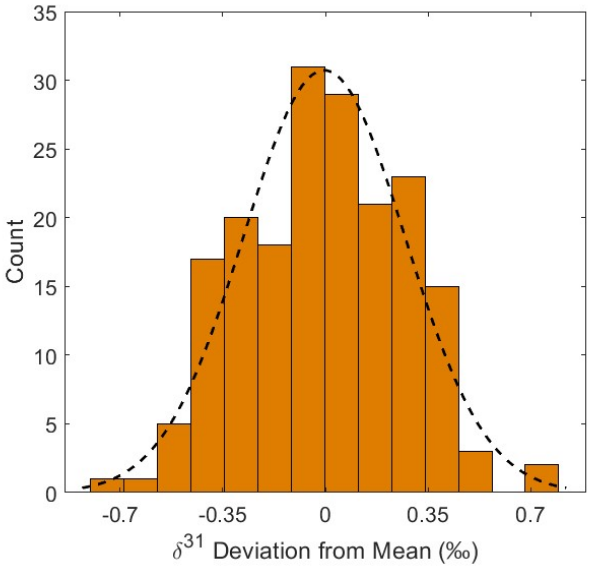

Figure 4.3. δ^{31} precision from 186 measurements of a whole air sample, $1\sigma = 0.28‰$.

Because the OHSU-PSU archive measurements are made over the course of several weeks, it is important to verify the reproducibility of measurements during the measurement process. The long-term precision, or measurement reproducibility, is calculated by evaluating the consistency of measurements from a secondary standard (CB11406-A). This standard is measured at least once every two weeks. Individual measurements of δ^{45}, δ^{46}, and δ^{31} are shown in figures 4.4 – 4.6 along with the mean (black line) and standard deviation (red dashed line) of the measured values.

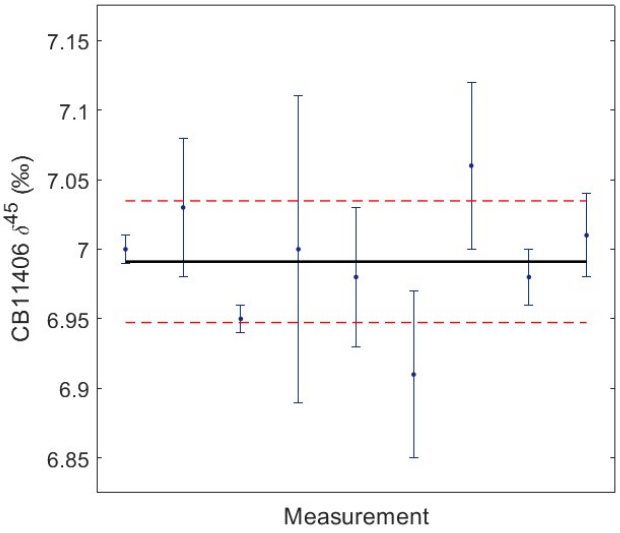

Figure 4.4. Reproducibility of δ^{45} as determined using 9 measurements of reference CB11406 with mean = 6.99‰ and 1σ = 0.04‰ (red-dashed lines).

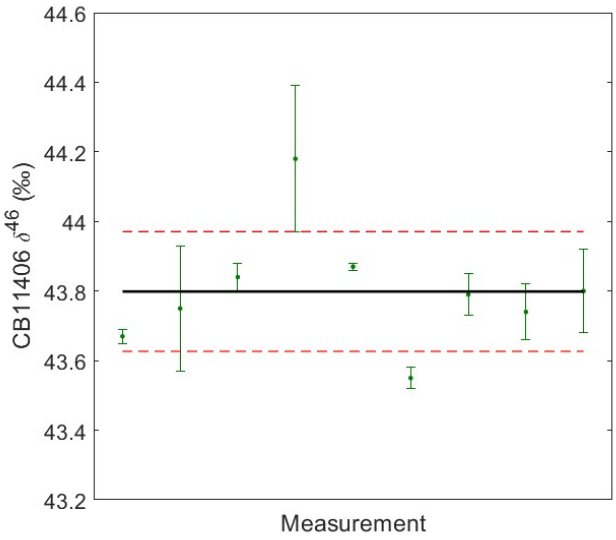

Figure 4.5. Reproducibility of δ^{46} as determined using 9 measurements of reference CB11406 with mean = 43.80‰ and 1σ = 0.17‰ (red-dashed lines).

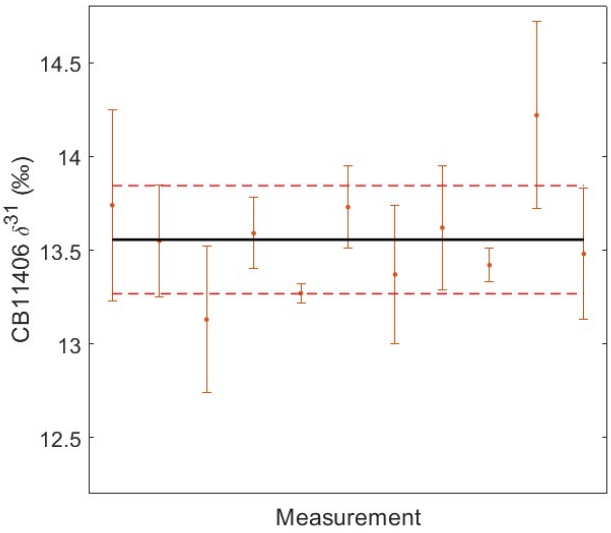

Figure 4.6. Reproducibility δ^{31} as determined using 11 measurements of reference CB11406 with mean = 13.56‰ and 1σ = 0.29‰ (red-dashed lines).

Results of the long-term 1σ reproducibility (δ^{45} = 0.04‰, δ^{46} = 0.17‰, and δ^{31} = 0.29‰) show similar standard deviations compared to individual measurement precision. Based on this analysis, we conclude that long-term measurement reproducibility is comparable to short term precision.

4.2 Shot-noise limit

The shot-noise limit is the theoretical best precision achievable for a measurement on a mass spectrometer. The value is determined through the statistics of ion collection and represents the precision assuming the ion beam is the only noise source. From Merritt and Hayes (1996), assuming the reference isotopic ratio is about the same as the sample ratio, the shot-noise limit can be written as:

(4.1) $$\sigma_\delta^2 = 2 \times 10^6 (\sigma_R / R)^2 = 2 \times 10^6 (1+R)^2 / (EMR)$$

where R = isotope ratio, E = IRMS efficiency, and M = number of molecules introduced.

The product *EM* represents the number of ions collected, which is equal to the integrated peak ion current divided by the charge of an electron (q_e = 1.6*10^{-19} C). The area of a peak, *A*, has units in volt seconds (Vs). If we divide the area by the feedback resistor of the ion channel (R_f = 3*10^8 Ω), this gives us the integrated peak ion current. We can then rewrite equation 4.1 as:

(4.2) $$\sigma_\delta^2 = 2 \times 10^6 (1+R)^2 \frac{R_f q_e}{AR} = 9.6 \times 10^{-5} \frac{(1+R)^2}{AR}$$

The shot-noise limit depends on the area of the sample peak, or the number of molecular ions detected by the system. To evaluate the sensitivity of the measurement precision to the number of molecules introduced, the working standard CC2854 was concentrated in T_1 for 4, 6, 8, and 10 minute intervals at a flow rate of 40 ml min^{-1}, concentrating 2.8 – 7.0 nmol N_2O. Measurements were repeated five times each. Table 4.2 contains the measured precision and theoretical shot-noise values calculated using eq. 4.2 for each sample size. Figures 4.7 – 4.9 show the measured precision for different sample volumes of the working standard (CC2854) with the shot-noise limit represented by the red dashed lines.

Table 4.2. Working standard CC2854 measurement precision for N_2O sample size.

T_1 Time (min)	N_2O (nmol)	δ^{45} σ	δ^{45} σ_{snl}	δ^{46} σ	δ^{46} σ_{snl}	δ^{31} σ	δ^{31} σ_{snl}
4	2.784	0.115	0.045	0.260	0.086	0.542	0.143
6	4.176	0.066	0.036	0.123	0.069	0.540	0.115
8	5.568	0.053	0.031	0.101	0.059	0.275	0.098
10	6.960	0.063	0.028	0.155	0.053	0.220	0.088

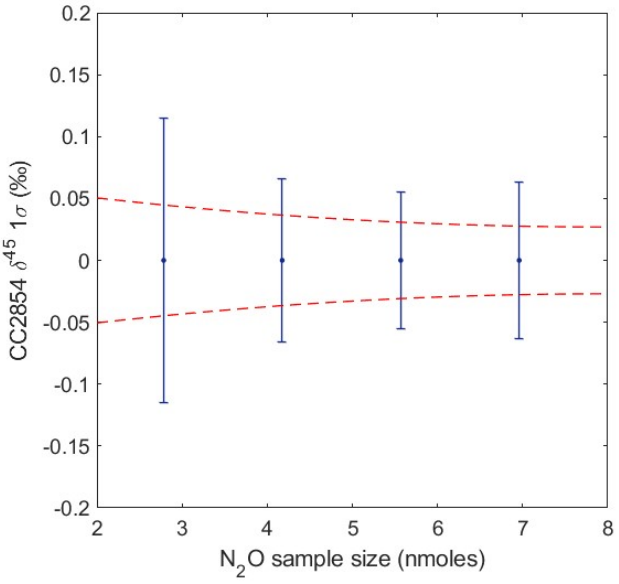

Figure 4.7. δ^{45} precision at 4 sample quantities (blue) and shot-noise limit (red).

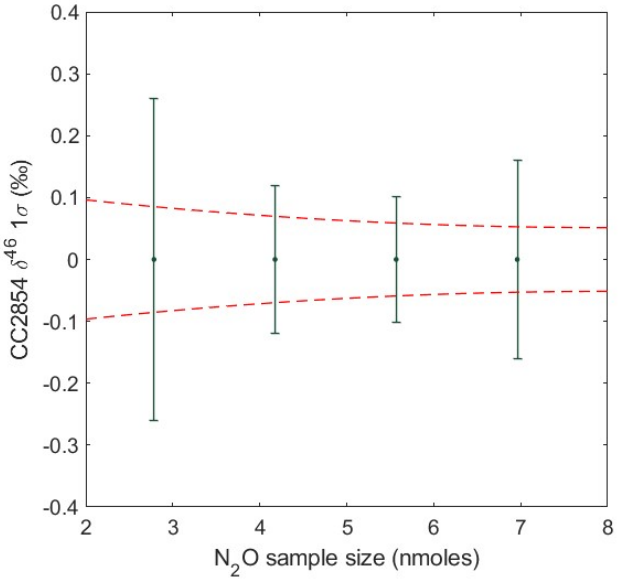

Figure 4.8. δ^{46} precision at 4 sample quantities (green) and shot-noise limit (red).

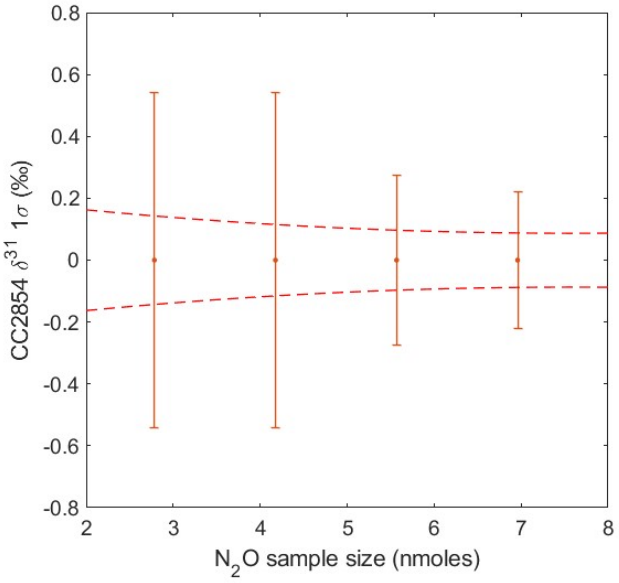

Figure 4.9. δ^{31} precision at 4 sample quantities (orange) and shot-noise limit (red).

The measurement uncertainty in δ^{45} and δ^{46} is similar for sample sizes greater than 4.2 nmoles of N_2O, with the achieved precision ~ 2x the theoretical shot-noise limit. In δ^{31}, a significant gain in precision is seen when increasing the sample size from 4.2 nmoles N_2O to 5.6 nmoles N_2O, with the achieved precision ~ 3x the theoretical shot-noise limit at 5.6 nmoles. For this reason and to minimize sample use during analysis, a N_2O sample size of ~5.6 nmoles is chosen as the sample size for all OHSU-PSU archive sample measurements.

In this work, we adapt sample processing volumes to account for sample concentration differences in order to optimize precision. The concentration of the working reference (CC2854) is ~390 ppb N_2O while the concentration of samples in the air archive range between 300 and 315 ppb N_2O. Therefore, to trap the desired nmoles of N_2O in T_1 using a constant flow rate of 40 ml min^{-1}, the working standard is trapped for 8 minutes while archive samples are trapped for 10 minutes.

4.3 IRMS sample size linearity

Sample size linearity issues have been reported when measuring the isotopic composition of N_2O (Rockmann et al. 2003). To evaluate the relationship between the measured isotopic composition of a sample and the sample size volume, different concentrations of the working standard (CC2854) spanning 2.78 – 6.98 nmol N_2O were analyzed. This corresponds to samples with N_2O mole fractions spanning 156 – 390 ppb N_2O with a flow rate of 40 ml min^{-1}. Each quantity was evaluated 5 times for statistical purposes. Results from this analysis are shown in figures 4.10 – 4.12.

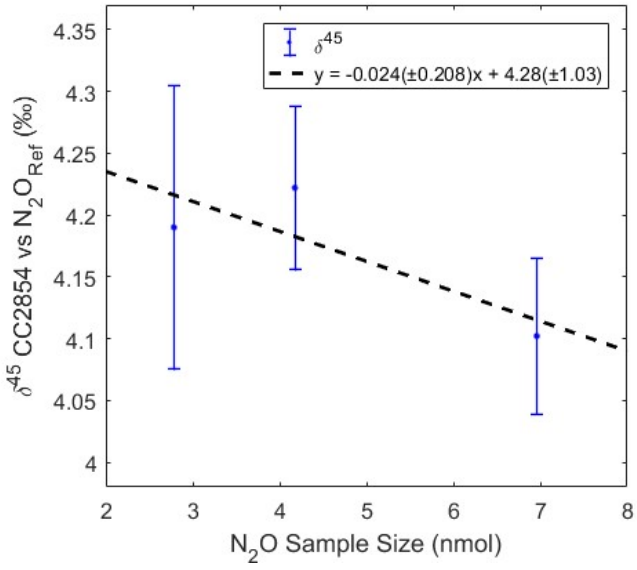

Figure 4.10. $\delta^{45}(N_2O)$ sample size linearity.

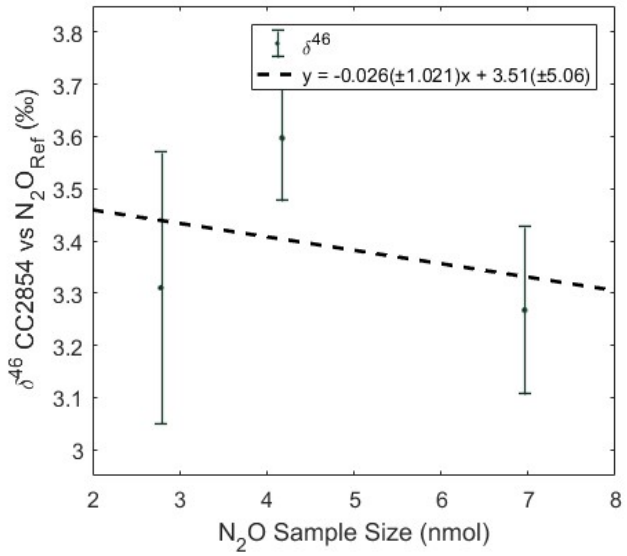

Figure 4.11. $\delta^{46}(N_2O)$ sample size linearity.

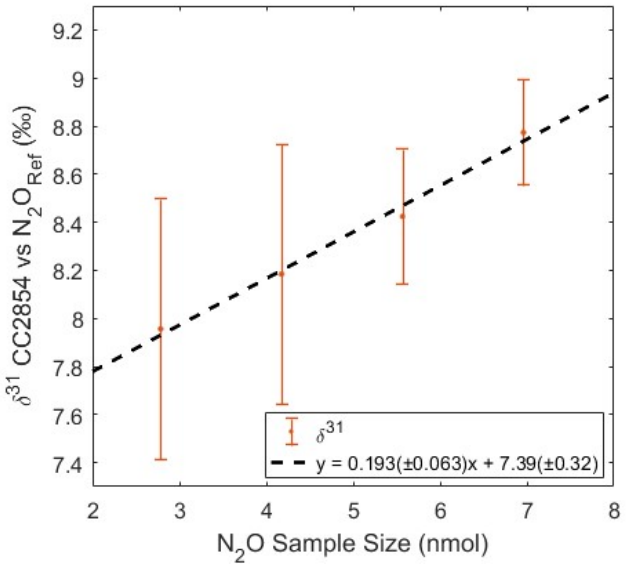

Figure 4.12. $\delta^{31}(N_2O)$ sample size linearity.

Results of the sample size linearity show that there is little deviation over the range evaluated in $\delta^{45}(N_2O)$ and $\delta^{46}(N_2O)$ within the level of measurement precision. The 95% confidence interval in the slope for both $\delta^{45}(N_2O)$ and $\delta^{46}(N_2O)$ overlap significantly

with 0.00‰ $nmol^{-1}$. Because sample N_2O mole fraction ranges from 300 – 315 ppb, concentrating samples for 10 minutes at a flow rate of 40 ml min^{-1} results in trapping 5.35 – 5.62 nmol N_2O. Applying the slope corrections for $\delta^{45}(N_2O)$ and $\delta^{46}(N_2O)$ shifts values a maximum of 0.007‰. As a result, no sample linearity correction is applied to measurements of $\delta^{45}(N_2O)$ and $\delta^{46}(N_2O)$. However, because this analysis only includes 3 datapoints, more measurements of different sample sizes may be needed to determine the effect of sample size linearity at higher levels of confidence.

The sample size linearity while measuring $\delta^{31}(N_2O)$ displays a positive linear relationship with a slope and y-intercept of 0.193 ± 0.063 and 7.39 ± 0.32, respectively. Archive samples have N_2O concentrations ranging 300 – 315 ppb. Using a 10 minute T_1 trap time with the MFC regulating the flow rate of samples at 40 ml min^{-1}, the archive sample size ranges 5.35 – 5.62 nmol N_2O. From the slope and y-intercept in this analysis, $\delta^{31}(N_2O)$ measures ~0.1‰ higher in samples with 5.711 nmol N_2O compared to samples with 5.265 nmol N_2O. Because this shift is about 1/3 the measurement precision for $\delta^{31}(N_2O)$, a linear correction is not applied to the archive measurements. If future isotopic measurements have a greater range in N_2O concentration, a linear correction will be necessary unless adjusting the T_1 concentration time to trap a consistent N_2O sample size.

4.4 Determination of the scrambling coefficient

Correctly defining the scrambling coefficient, *s* (eq. 2.11), is necessary to solve for the intramolecular isotopic composition. This is typically accomplished through measurements of the working standard after doping with pure ^{15}NNO and/or $N^{15}NO$ (purity > 99%) (Rockmann et al. 2003; Park et al. 2004; Westley et al. 2007). If there is

no scrambling during ionization, then doping the working standard with pure ^{15}NNO should result in a slope of 0 when plotting the measured ^{31}R versus ^{45}R. If doping with $N^{15}NO$ and no scrambling is expected, then the slope should be equal to 1 when plotting measured ^{31}R versus ^{45}R. Likewise, if doping with ^{15}NNO and no scrabbling were to occur, then the slope of ^{31}R versus ^{45}R will be 0.

During the summer of 2018, work completed by Rebecca Xie and Andrew Rice at Portland State University through the Research Experience for Undergraduates (REU) program investigated the scrambling coefficient within the Delta V IRMS while running in dual inlet mode. Using > 98% pure ^{15}NNO (Cambridge Isotope Labs, Tewksbury, MA), 3 calibration gases were prepared by initially adding a small amount of ^{15}NNO to evacuated canisters (130 mL) which were then each filled with pure N_2O (reference gas). The manometric dilution process was completed in a vacuum line system with 10.000 ± 0.001 torr and 1000.0 ± 0.1 torr pressure gauges (MKS Instruments, Andover, MA). Table 4.3 provides pressures of the gases added to the canisters, manometrically determined (expected) ^{45}R, IRMS (measured) ^{45}R and ^{31}R with measurement uncertainty. Uncertainty (1σ) in measurement (~2e-07) and introduced from the manometric process (~2e-06) is small compared to the magnitude of the R values.

The linear fit from plotting measured ^{45}R vs. expected ^{45}R (fig. 4.13) can be used to evaluate the accuracy and precision of the manometric process when preparing the standards. Results show the slope (1.014 ± 0.025) and y-intercept (-0.0001 ± 0.0003) have 95% confidence intervals that overlap well with 1.0 and 0.00, respectively. This suggests the manometric process is accurate and precise.

Table 4.3. Manometrically prepared standards for determination of scrambling coefficient (Xie and Rice, 2018).

Canister ID	[a.] $P_{Cambridge}$ (Torr)	[b.] P_{Final} (Torr)	[c.] ^{45}R Expected	^{45}R Measured	^{45}R 1σ Measured	^{31}R Measured	^{31}R 1σ Measured
spike 1	9.559	980.2	0.0175059	0.0176335	2.91E-07	0.0048927	2.70E-07
spike 2	4.509	774.9	0.0135727	0.0135926	2.13E-07	0.0045603	4.19E-07
spike 3	1.811	669.5	0.0104589	0.0104290	1.67E-07	0.0042972	2.61E-07
N_2O_{Ref}	-	-	0.0077539	0.0077539	1.61E-07	0.0040729	2.51E-07

a. Pressure added to 130 ml volume from ^{15}NNO.

b. Final pressure of 130 ml volume after adding N_2O_{Ref}.

c. Expected ^{45}R calculated from $P_{Cambridge}/P_{Final} + {}^{45}R_{Ref}$.

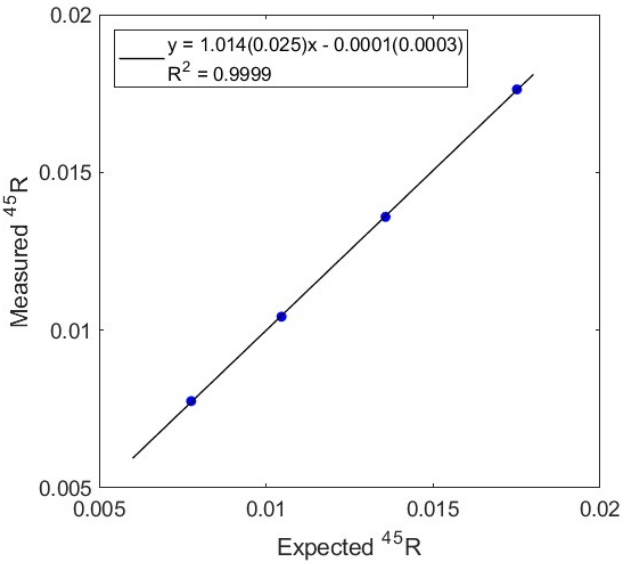

Figure 4.13. Measured ^{45}R vs. expected ^{45}R. Error bars representing 1σ are too small to appear in the plot. Values in parenthesis are 95% CI around the slope and y-intercept.

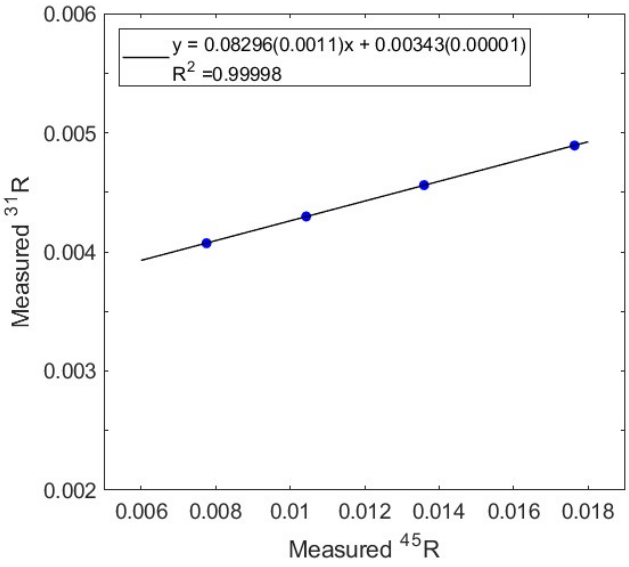

Figure 4.14. Measured ^{31}R vs. measured ^{45}R. Error bars representing 1σ are too small to appear in the plot. Values in parenthesis are 95% CI around the slope and y-intercept.

From figure 4.14, the scrambling coefficient of the IRMS can be identified. The slope from the plot of ^{31}R measured vs. ^{45}R measured has a value of 0.08296 (± 0.0011). This represents a scrambling coefficient of 8.3% within the IRMS.

The scrambling coefficient was also calculated independently through taking advantage of the fact that two of the EMPA standards calibrated on the TITech N_2O isotopic scale have SP ($\delta^{15}N^{\alpha}$ - $\delta^{15}N^{\beta}$) ~0‰ (see Table 1.3). This derivation begins with the definition of the elemental isotope ratio R when measuring the NO^+ fragment:

(4.3) $$^{31}R_{std} = ^{15}R_{N_2} + ^{17}R_{VSMOW}$$

(4.4) $$^{31}R_{EMPA} = ^{17}R_{EMPA} + ^{15}R^{\alpha}_{EMPA}$$

The values in equations 4.3 and 4.4 are treated as exact. We also define the scrambled isotope ratio using the simplified version of eq. 2.11:

(4.5) $$^{31}R^{S}_{EMPA} = ^{17}R_{EMPA} + S\left(^{15}R^{\beta}_{EMPA}\right) + (1-S)\left(^{15}R^{\alpha}_{EMPA}\right)$$

For EMPA 90575 and EMPA 90454, the scrambled ratio ($^{31}R^{S}$) is indistinguishable from the non-scrambled ratio (^{31}R). We now define the ratio of EMPA and our reference gas:

$$r^{31}R^{S}_{EMPA} = \frac{^{31}R^{S}_{EMPA}}{^{31}R_{std}} \tag{4.6}$$

$$r^{31}R^{S}_{ref} = \frac{^{31}R^{S}_{ref}}{^{31}R_{std}} \tag{4.7}$$

From here, we now define the measured peak area ratio of EMPA to our reference gas:

$$r^{31}R^{S}_{EMPA/ref} = \frac{^{31/30}A_{EMPA}}{^{31/30}A_{ref}} = \frac{^{31}R^{S}_{EMPA}}{^{31}R^{S}_{ref}} \tag{4.8}$$

Where $^{31/30}A$ represents the measured peak area ratio. Solving equation 4.8 for R_{ref} gives:

$$^{31}R^{S}_{ref} = \frac{^{31}R^{S}_{EMPA}}{r^{31}R^{S}_{EMPA/ref}} \tag{4.9}$$

Equation 4.9 is true for any EMPA standard measured, therefore, we can set $^{31}R^{S}_{ref}$ calculated from EMPA 90454 or EMPA 90575 (where $^{31}R^{S} = {}^{31}R$) equal to $^{31}R^{S}_{ref}$ calculated from EMPA CA08214 and EMPA CB08976.

$$^{31}R^{S}_{CA08214} = {}^{31}R_{90454}\frac{r^{31}R^{S}_{CA08214/ref}}{r^{31}R^{S}_{90454/ref}} \tag{4.10}$$

Where the ratio on the right-hand side of equation 4.10 is measured and $^{31}R_{90454}$ is already known. Combining equation 4.10 with equation 4.5, we can now solve for the scrambling coefficient *s*.

$$s = \frac{^{31}R_{90454}\frac{r^{31}R^{S}_{CA08214/ref}}{r^{31}R^{S}_{90454/ref}} - {}^{17}R_{CA08214} - {}^{15}R^{\alpha}_{CA08214}}{^{15}R^{\beta}_{CA08214} - {}^{15}R^{\alpha}_{CA08214}} \tag{4.11}$$

Results of this method for calculating *s* are given in table 4.4.

Table 4.4. Scrambling coefficient calculations from 2 EMPA standards.

EMPA #	*CA08214*	*CB08976*
90575	0.144	0.124
90454	0.094	0.070

The mean and standard deviation of the calculated scrambling coefficients, *s*, is 0.108 and 0.033, respectively. Uncertainty in the mean value overlaps with the commonly reported scrambling coefficient value of 0.085 (Kaiser et al. 2003; Westley et al. 2007; Potter et al. 2013) as well as the value reported from the method above of 0.083.

From the two independent methods used to find the scrambling coefficient, doping the reference gas with labeled ^{15}NNO produces a more precise and reliable value due to the large range of SP produced in synthetic mixtures. The second method is theoretically correct; however, because the EMPA standard ^{31}R values are all near the same value, the scrambling coefficient is calculated around a point rather than from a slope that spans a large range (as the first method does).

4.5 Isotopic composition precision

Solving for $\delta^{15}N$, $\delta^{18}O$, $\delta^{15}N^{\alpha}$, and $\delta^{15}N^{\beta}$ is accomplished numerically using equations 2.8, 2.9, 2.11 (ignoring the last term), and 2.12 (Appendix B). The uncertainty in each value is found through bootstrapping 1000 values generated from a normal distribution centered at the mean measured values (δ^{45}, δ^{46}, and δ^{31}) with standard deviations equal the total measurement uncertainty for the sample (equation 2.15). The

typical standard (CC2854) and sample (OHSU-PSU air archive) uncertainty for $\delta^{15}N$, $\delta^{18}O$, $\delta^{15}N^{\alpha}$, and $\delta^{15}N^{\beta}$ using a scrambling coefficient $s = 0.083$ are given in table 4.5 as well as previously reported isotopic composition precisions by other laboratories.

Table 4.5. N_2O isotopic composition 1σ uncertainty using continuous flow IRMS.

Study	$\delta^{15}N$	$\delta^{18}O$	$\delta^{15}N^{\alpha}$	$\delta^{15}N^{\beta}$
Potter et al. 2013	0.05	0.10	0.11	0.14
Rockmann and Levin 2005	0.06	0.09	0.30	0.30
Yoshida and Toyoda, 2000	0.10	0.10	0.50	0.50
Park et al. 2012	0.20	0.20	0.80	0.80
This work (Standard)	***0.05***	***0.10***	***0.37***	***0.39***
This work (Sample)	***0.07***	***0.15***	***0.57***	***0.60***

The isotopic composition precision achieved in this work is comparable with that achieved by other groups. IRMS measurement precision is impacted by external (e.g., pre-concentration process, flow rates, gas purity, room temperature) and internal (ion source, voltage, vacuum pressure, internal temperature) factors. Maintaining a rigorous attention to detail in the method is important to achieve reproducible results.

4.6 Cape Meares isotopic results

The following subsections present and discuss the results of the OHSU-PSU Air Archive N_2O bulk and intramolecular isotopic analysis. Following calculations of $\delta^{15}N$, $\delta^{18}O$, $\delta^{15}N^{\alpha}$, and $\delta^{15}N^{\beta}$, 159 sample measurements (Table A.1) were initially filtered for analysis using a 6 median absolute deviation (6MAD) noise filter to remove far outliers. Polynomial fits (1st degree) were then applied to the data sets. Residual values outside of 2σ to the polynomial fits were removed from further analysis. The entire process

removed 5 samples from $\delta^{15}N$, 15 samples from $\delta^{18}O$, 10 samples from $\delta^{15}N^{\alpha}$, 4 samples from $\delta^{15}N^{\beta}$, and 6 samples from SP.

Seasonality is calculated from the residuals of observed data points to a LOWESS regression with a large smoothing window (33.3% of the data). Residuals are then plotted against their fractional date where a second LOWESS regression is applied using a 30-day smoothing window. Once the seasonality is established, the dataset is deseasonalized to remove seasonal variability, then plotted against the collection date. A LOWESS regression is applied using a 3-year smoothing window, which is used to find the annual trend. The trend is calculated by applying a SPLINE fit to the LOWESS regression to interpolate the isotopic composition for every month in the time series. The first derivative of the SPLINE fit then provides a month to month trend.

4.6.1 Cape Meares N_2O isotopic seasonality

N_2O isotopic seasonality is shown in figure 4.13. The black line is the LOWESS fit to the residuals. Data points represent the average residual binned by month with error bars representing the standard error of the binned data within the month. The shaded region is the 95% CI in the LOWESS fit calculated from 1000 bootstrapped LOWESS fits after including observed variability of the residuals to the secular trend.

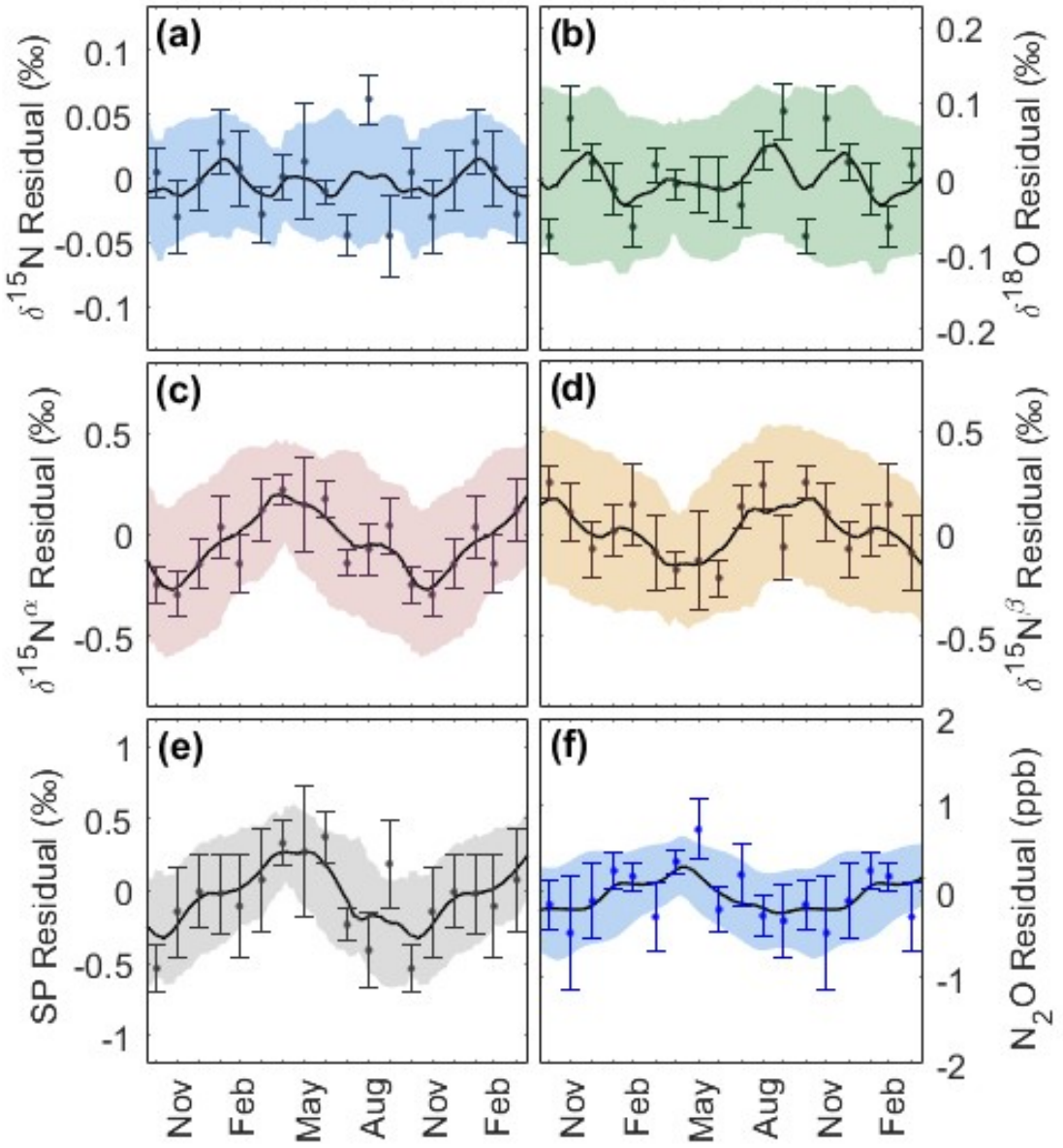

Figure 4.15. N_2O isotopic seasonality for Cape Meares. Panels show $\delta^{15}N$ (a), $\delta^{18}O$ (b), $\delta^{15}N^{\alpha}$ (c), $\delta^{15}N^{\beta}$ (d), SP (e), and N_2O mole fraction (f). Data points represent the month mean residual with error bars equal to the standard error for the month. Shaded regions are 95% CI around the LOWESS fits.

No distinguishable seasonality is found in $\delta^{15}N$ or $\delta^{18}O$ (fig. 4.15 (a) and (b)). The 95% CI around the LOWESS fit for $\delta^{15}N$ and $\delta^{18}O$ is ± 0.05‰ and ± 0.1‰, respectively.

These are slightly smaller than the average uncertainty in sample $\delta^{15}N$ and $\delta^{18}O$. A possible explanation for why no seasonality is present in $\delta^{15}N$ and $\delta^{18}O$ is that the magnitude of seasonal $\delta^{15}N$ and $\delta^{18}O$ at Cape Meares during the time the archive samples were collected is smaller than our current measurement precision. This result is unexpected due to the observed seasonality in N_2O mole fraction (fig. 4.15 (f)).

The seasonality of $\delta^{15}N^{\alpha}$ and $\delta^{15}N^{\beta}$ (fig. 4.15 (c) and (d)) show statistically significant amplitudes with nearly opposite phases. $\delta^{15}N^{\alpha}$ has a maximum amplitude of 0.2 ± 0.2‰ (1σ) near April and a minimum amplitude of -0.3 ± 0.3‰ (1σ) near November. $\delta^{15}N^{\beta}$ has a maximum amplitude of 0.2 ± 0.2‰ (1σ) near November and a minimum amplitude of -0.2 ± 0.2‰ (1σ) near April. The resulting SP also shows a statistically significant seasonality, with a maximum of 0.3 ± 0.2‰ (1σ) near April and a minimum of -0.4 ± 0.2‰ (1σ) near November.

Results of grouping residual data into meteorological seasonal bins is given in table 4.6, providing seasonal statistics. The seasonal means for $\delta^{15}N$ and $\delta^{18}O$ are ~0.00‰, again indicating that there is no significant seasonality present in the archive measurements for these values. Seasonal mean values and phasing for $\delta^{15}N^{\alpha}$, $\delta^{15}N^{\beta}$, and SP are similar to the LOWESS minimum and maximum values discussed earlier.

Table 4.6. Cape Meares isotopic N_2O seasonal statistics.

	Statistic	Winter (D, J, F)	Spring (M, A, M)	Summer (J, J, A)	Fall (S, O, N)
$\delta^{15}N$	*Count*	35	48	35	36
	Mean (‰)	0.01	0.00	0.00	-0.02
	1σ (‰)	0.08	0.09	0.06	0.10
$\delta^{18}O$	*Count*	33	45	34	32
	Mean (‰)	-0.01	0.00	0.00	0.01
	1σ (‰)	0.10	0.10	0.12	0.13
$\delta^{15}N^{\alpha}$	*Count*	32	48	32	37
	Mean (‰)	-0.07	0.20	0.00	-0.18
	1σ (‰)	0.44	0.48	0.36	0.45
$\delta^{15}N^{\beta}$	*Count*	35	49	35	36
	Mean (‰)	0.01	-0.16	0.05	0.14
	1σ (‰)	0.50	0.58	0.43	0.46
SP	*Count*	34	48	33	38
	Mean (‰)	-0.04	0.32	-0.10	-0.25
	1σ (‰)	0.94	1.01	0.79	1.00

The p-values in table 4.7 are Kolmogorov-Smirnov test statistics comparing paired seasonal statistics. The results for $\delta^{15}N$ and $\delta^{18}O$ indicate there is no statistical difference between seasons. For $\delta^{15}N^{\alpha}$, $\delta^{15}N^{\beta}$, and SP, there is high confidence that spring is statistically different from the other three seasons, meaning the spring maximum for $\delta^{15}N^{\alpha}$ and SP is statistically robust as well as the spring minimum in $\delta^{15}N^{\beta}$.

Table 4.7. Isotopic N_2O Kolmogorov-Smirnov p-value test statistics.

$\delta^{15}N$	*Fall*	*Summer*	*Spring*
Winter	0.39	0.28	0.88
Spring	0.84	0.40	
Summer	0.20		

$\delta^{18}O$	*Fall*	*Summer*	*Spring*
Winter	0.54	0.97	0.99
Spring	0.48	0.84	
Summer	0.85		

$\delta^{15}N^{\alpha}$	*Fall*	*Summer*	*Spring*
Winter	0.24	0.44	< 0.001
Spring	< 0.001	0.004	
Summer	0.02		

$\delta^{15}N^{\beta}$	*Fall*	*Summer*	*Spring*
Winter	0.32	0.64	0.09
Spring	0.007	0.009	
Summer	0.33		

SP	*Fall*	*Summer*	*Spring*
Winter	0.42	0.87	0.02
Spring	0.01	0.004	
Summer	0.28		

N_2O isotopic seasonality has not previously been reported in the northern hemisphere. Archived air samples from Cape Grim, Tasmania (41° S, 145° E) dating between 1978 and 2005 are reported to display seasonality in $\delta^{15}N$, $\delta^{18}O$, and $\delta^{15}N^{\alpha}$ with amplitudes of 0.04‰, 0.07‰, and 0.4‰, respectively (Park et al. 2012). The phase of the seasonal signal is similar for all three reported delta values with maximums observed near June (southern hemisphere winter) and minimums observed near December (southern hemisphere summer). These isotopic seasonal phases are nearly opposite that of the seasonal N_2O mole fraction, which has a maximum near December and a minimum near July. For the southern hemisphere, the conclusions from that work are that the

maximum influence of STE near May brings in N_2O depleted, isotopically enriched air from the stratosphere to the Cape Grim background while in October, the maximum in ocean ventilation produces N_2O enriched, isotopically depleted air.

Comparing N_2O isotopic seasonality for Cape Meares with observations from Cape Grim, we can conclude there are different influential processes occurring at each location. At Cape Meares during the spring, the processes that contribute air enriched in N_2O mole fraction also contribute enriched $\delta^{15}N^{\alpha}$ and depleted $\delta^{15}N^{\beta}$. During the fall, the processes that contribute air depleted in N_2O mole fraction also contribute depleted $\delta^{15}N^{\alpha}$ and enriched $\delta^{15}N^{\beta}$. The phases of $\delta^{15}N^{\alpha}$ and $\delta^{15}N^{\beta}$ destructively interfere with one another at Cape Meares, resulting in no seasonal behavior in $\delta^{15}N$ bulk.

The maximum influence of STE at Cape Meares is expected to occur during Fall, bringing in air that is enriched in isotopic composition and depleted in N_2O mole fraction (Jiang et al. 2007, Park et al. 2012). This driver of seasonality is sufficient to explain the observations of N_2O mole fraction, $\delta^{15}N^{\alpha}$, and SP, but does not explain the behavior of $\delta^{15}N$ bulk, $\delta^{18}O$, or $\delta^{15}N^{\beta}$. If STE was the only seasonal forcing process, then these isotopic compositions should also show observable seasonality matching the influence of STE.

Coastal upwelling along the Pacific Northwest coastline has a strong seasonality and has been suggested as a possible driver of N_2O seasonality (Lueker et al. 2003). Measurements of coastal upwelling along the Oregon coast by NOAA (PFEL) show that peak magnitude occur during July and a minimum during January. Coastal upwelling is expected to bring in isotopically depleted, N_2O enriched air (Nevison et al. 2005, Park et

al. 2012). However, N_2O concentrations are decreasing in the summer months at Cape Meares, reaching a minimum in fall, inconsistent with an upwelling-driven effect.

Comparing the expected influence of STE and ocean upwelling at Cape Meares suggests that the dominant driving influence of N_2O at Cape Meares is STE. However, STE alone is not enough to explain the observed seasonality in $\delta^{15}N$ bulk, $\delta^{18}O$, or $\delta^{15}N^{\beta}$. Two conclusions that can be made from these observations are:

1) Coastal upwelling must be less influential on the seasonality compared to STE at Cape Meares because the concentration of N_2O is decreasing during the summer into the fall months.
2) At least one other seasonal forcing process or source must be present at Cape Meares to explain the lack of seasonality in $\delta^{15}N$ bulk and $\delta^{18}O$ while maintaining a robust observed seasonality in $\delta^{15}N^{\alpha}$, $\delta^{15}N^{\beta}$, and SP.

Further investigations of specific seasonal forcing processes at Cape Meares would be helpful to quantify the relative importance of different seasonal sources and transport effects.

4.6.2 Cape Meares N_2O isotopic composition 1978 - 1997

Deseasonalized measurements of the N_2O isotopic composition from Cape Meares archived samples are shown in figure 4.16 in panels (a) – (e) along with N_2O mole fraction shown in panel (f). In 1980, the isotopic composition of $\delta^{15}N$, $\delta^{18}O$, $\delta^{15}N^{\alpha}$, $\delta^{15}N^{\beta}$, and SP measure 7.61 ± 0.03‰, 44.64 ± 0.03‰, 16.4 ± 0.1‰, -1.0± 0.1‰, and 17.6 ± 0.2‰, respectively, with ± representing 1σ uncertainty. In 1996, the isotopic composition of $\delta^{15}N$, $\delta^{18}O$, $\delta^{15}N^{\alpha}$, $\delta^{15}N^{\beta}$, and SP measure 6.99 ± 0.02‰, 44.34 ± 0.03‰,

15.3 ± 0.1‰, -1.3 ± 0.1‰, and 16.5 ± 0.2‰, respectively, with ± representing 1σ uncertainty.

Measurements from the OHSU-PSU Air Archive compare well to most previously reported values from northern and southern hemispheres measurements. Ishijima et al. (2007) measured firn air samples from Greenland (75°N, 42°W; collected in 2001) and Antarctica (77.3°S, 39.7°E and 69.2°S, 41.1°E; collected in 1998). Prokopiou et al. (2017) also measured firn air samples from Greenland (77°N, 51°W; collected in 2008 and 2009) and Antarctica (75°S, 65°E and 75°S, 123°E; collected in 1998 and 1999, respectively). Rockmann and Levin (2005) analyzed 23 archived air samples collected from Neumayer, Antarctica (71°S, 8°W) between 1990 and 2002. Park et al. (2012) analyzed 50 whole air samples collected at Cape Grim, Tasmania (41°S, 145°E) between 1978 and 2005. Data from these studies was digitized from plots in their respective publications to evaluate over the same time period as the Cape Meares data set. Table 4.8 gives N_2O isotopic measurements on the TITech scale for the years 1980 and 1996 measured from northern and southern hemisphere firn air and air archive measurements after applying linear fits to each dataset. Figure 4.17 shows a visual comparison of the datasets.

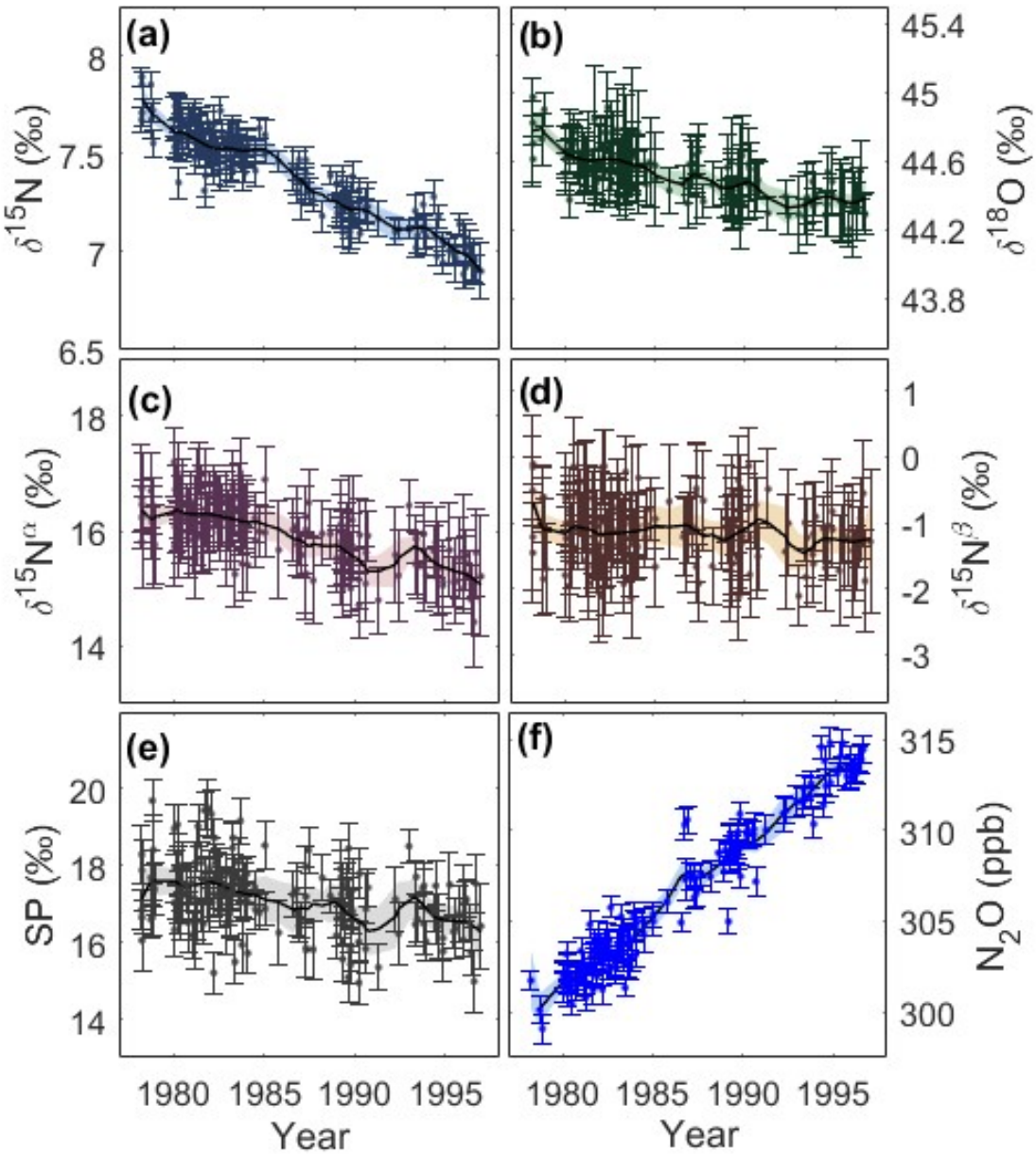

Figure 4.16. Deseasonalized isotopic N_2O measurements from Cape Meares, Oregon. Panels show $\delta^{15}N$ (a), $\delta^{18}O$ (b), $\delta^{15}N^{\alpha}$ (c), $\delta^{15}N^{\beta}$ (d), SP (e), and N_2O mole fraction (f). Error bars are total uncertainty. Solid black lines are LOWESS fits to the data using a 3-year smoothing window. The shaded regions are 95% confidence interval in the LOWESS fit calculated from 1000 bootstrapped fits.

Table 4.8. Literature atmospheric N_2O isotopic measurements.

Study	Sample Type (Hemisphere)	$\delta^{15}N$ (‰)		$\delta^{18}O$ (‰)		$\delta^{15}N^{\alpha}$ (‰)		$\delta^{15}N^{\beta}$ (‰)	
		1980	1996	1980	1996	1980	1996	1980	1996
1.	firn (N&S)	7.9	7.2	44.8	44.5	n/a	n/a	n/a	n/a
2.	firn (N&S)	7.4	6.9	44.9	44.7	16.3	15.9	-1.5	-2.2
3.	archive (S)	n/a	7.0	n/a	44.8	n/a	16.0	n/a	-2.0
4.	archive (S)	7.2	6.6	44.8	44.5	16.9	16.5	-2.4	-3.0
5.	archive (N)	7.6	7.0	44.7	44.4	16.4	15.3	-1.0	-1.3

Study: 1. Ishijima et al. 2007; 2. Prokopiou et al. 2017; 3. Rockmann and Levin 2005; 4. Park et al. 2012; 5. Cape Meares, Oregon (this work).

Cape Meares measurements of $\delta^{15}N$ are similar to comparable measured values with the exception of $\delta^{15}N$ measurements from the Cape Grim air archive by Park et al. (2012), which measures ~0.4‰ lower than Cape Meares. This is likely due to instrument calibration differences between laboratories as isotopic measurements from the same period are expected to be heavier in the southern hemisphere by 0.0‰ - 0.1‰ (Ishijima et al. 2007).

Measurements of $\delta^{18}O$ at Cape Meares are on average ~0.1‰ lower when compared to measurements by the other groups, with the exception of Rockmann and Levin (2005). While spatial differences could contribute to this offset, the uncertainty in measurement of $\delta^{18}O$ is also 0.1‰. Therefore, the difference is not statistically robust at high levels of confidence.

The intramolecular isotopic composition of $\delta^{15}N^{\alpha}$ at Cape Meares matches well with mean $\delta^{15}N^{\alpha}$ firn air for 1980 measured by Prokopiou et al. (2017, red); however, in 1996, $\delta^{15}N^{\alpha}$ at Cape Meares is depleted compared to Prokopiou et al. (2017) and measurements from Neumayer, Antarctica (Rockmann and Levin, 2005) by ~0.6‰. Although the Cape Grim air archive (blue, Park et al. 2012) shows considerable

variability in $\delta^{15}N^{\alpha}$, Cape Meares data is depleted in $\delta^{15}N^{\alpha}$ by 0.5‰ in 1980 and 1.2‰ in 1996 relative to the Cape Grim measurements.

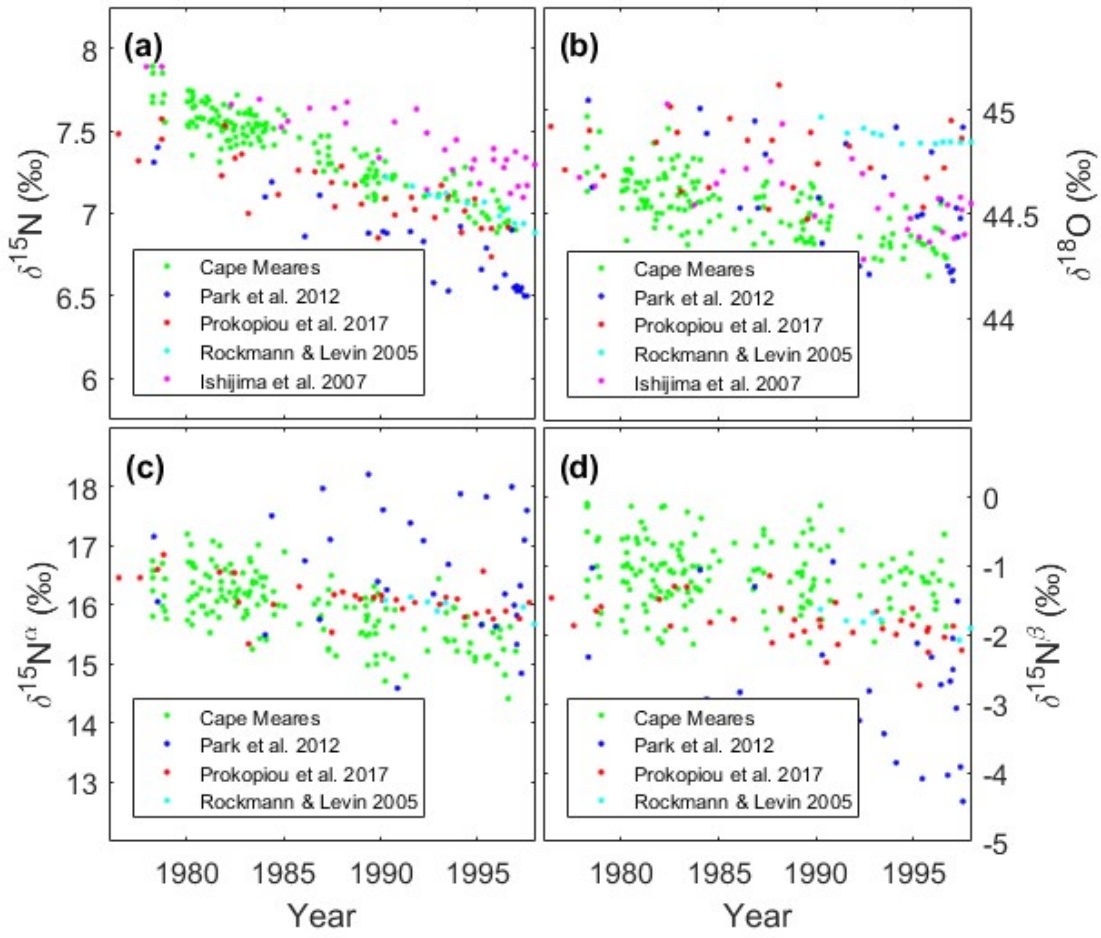

Figure 4.17. Isotopic N_2O measurement comparison plots. Panels show $\delta^{15}N$ (a), $\delta^{18}O$ (b), $\delta^{15}N^{\alpha}$ (c), and $\delta^{15}N^{\beta}$ (d). Data from Park et al. 2012 (blue), Prokopiou et al. 2017 (red), Rockmann and Levin, 2005 (cyan), and Ishijima et al. 2007 (pink) is digitized from plots in their respective publications.

By contrast, the composition of $\delta^{15}N^{\beta}$ at Cape Meares remains nearly constant between 1980 and 1996, only changing from -1.0‰ to -1.3‰. With sample variability of ~0.6‰, the uncertainty overlaps with both Prokopiou et al. (2017) and Rockmann and

Levin (2005). Mean values from Cape Grim from Park et al. (2012) are significantly more depleted by -2.4‰ and -3.0‰ in 1980 and 1996, respectively.

4.6.3 Cape Meares N_2O isotopic secular trend 1978 - 1997

Annual trends for N_2O isotopic composition are shown in figure 4.18. The 95% confidence intervals are created by determining the temporal trend in time for 1000 bootstrapped datasets (fig. 4.18 shaded regions). Data points represent the mean annual trend with error bars equal to one standard deviation of the trend over the year. Aside from $\delta^{15}N$, annual trends calculated for an individual year are indistinguishable from 0‰ yr^{-1} for isotopic composition. This is due in part to the larger measurement uncertainty and noise in the intramolecular isotopic composition data.

Isotopic secular trends with 95% confidence intervals between 1978 and 1996 at Cape Meares, Oregon are given in table 4.9 calculated by applying a linear fit to the raw and deseasonalized data. Secular trends for all isotopic compositions are statistically different from 0‰ yr^{-1} with the exception of $\delta^{15}N^{\beta}$. From table 1.2, most anthropogenic sources of N_2O are isotopically depleted relative to the atmosphere. The decreasing isotopic composition of the troposphere reflects the increased influence of anthropogenic sources of N_2O to the atmosphere.

Table 4.10 gives secular trends for N_2O isotopic composition reported in the literature as well as the date range the trend is calculated over. The secular trends for $\delta^{15}N$ and $\delta^{18}O$ at Cape Meares compare well to previously reported values, though the temporal spans the trends are calculated over are different. However, the secular trend in $\delta^{15}N^{\alpha}$ and $\delta^{15}N^{\beta}$ at Cape Meares are significantly different compared to previously

reported values. The $\delta^{15}N^{\alpha}$ and $\delta^{15}N^{\beta}$ trends reported by Rockmann and Levin (2005), from Neumayer, Antarctica archived air samples are close to the $\delta^{15}N^{\beta}$ and $\delta^{15}N^{\alpha}$ trends found here for Cape Meares, respectively. In other words, observations at Cape Meares are nearly opposite of what Rockmann and Levin (2005) report for intramolecular trends from Neumayer, Antarctica.

Table 4.9. N_2O isotopic secular trends (‰ yr^{-1}) for Cape Meares, Oregon.

δ Value	Raw Data	R^2	Deseasonalized	R^2
$\delta^{15}N$	-0.041 ± 0.003	0.86	-0.041 ± 0.003	0.86
$\delta^{18}O$	-0.019 ± 0.004	0.45	-0.020 ± 0.003	0.48
$\delta^{15}N^{\alpha}$	-0.070 ± 0.014	0.40	-0.067 ± 0.013	0.43
$\delta^{15}N^{\beta}$	-0.010 ± 0.015	0.01	-0.013 ± 0.014	0.02
SP	-0.072 ± 0.029	0.14	-0.064 ± 0.028	0.14

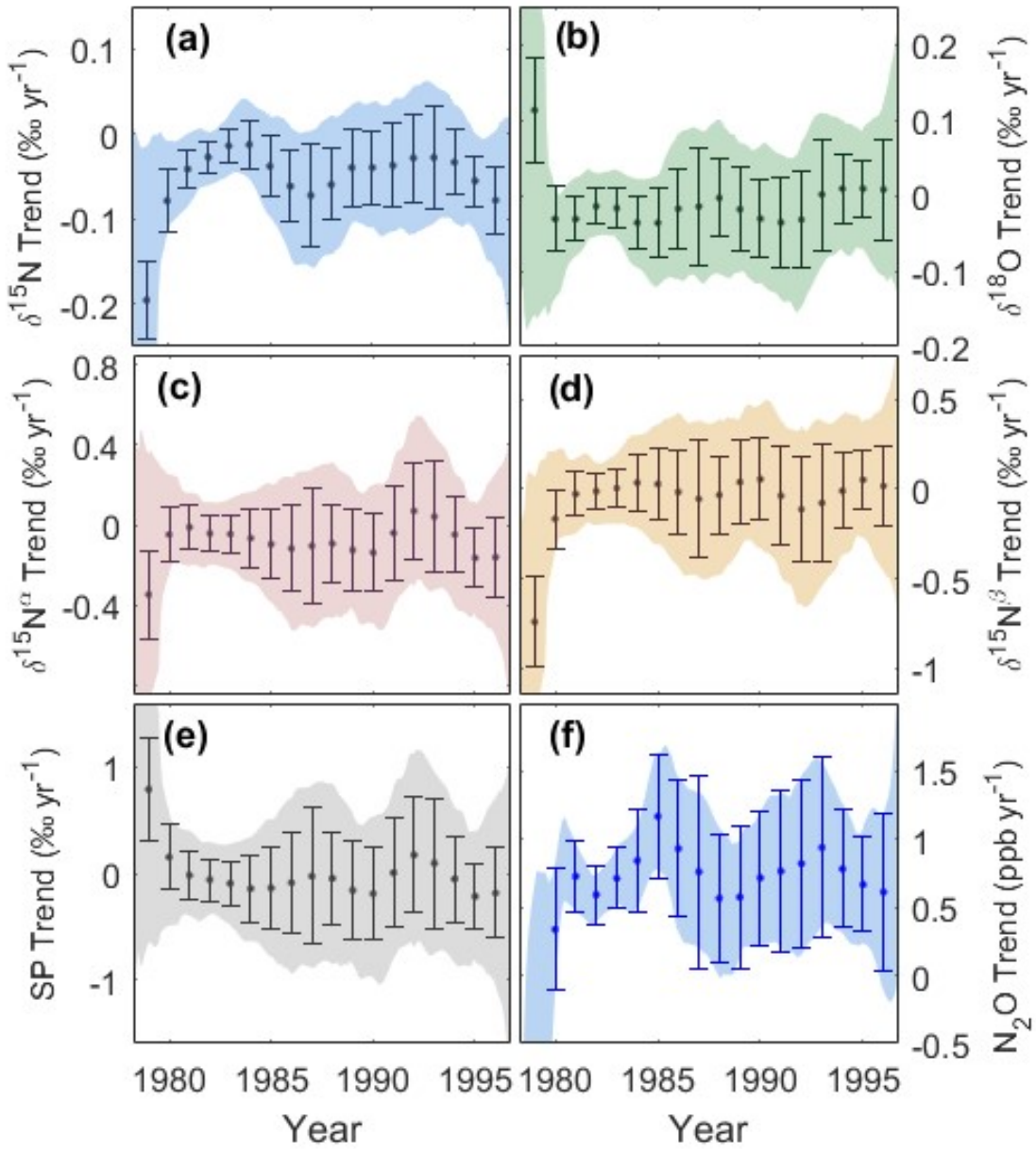

Figure 4.18. Isotopic N_2O annual trends from Cape Meares, Oregon. Panels show $\delta^{15}N$ (a), $\delta^{18}O$ (b), $\delta^{15}N^{\alpha}$ (c), $\delta^{15}N^{\beta}$ (d), SP (e), and N_2O mole fraction (f). Error bars are annual trend standard deviation. The shaded regions are 95% confidence interval calculated from 1000 bootstrapped fits.

Table 4.10. Literature atmospheric N_2O isotopic secular trends with 95% CI.

Study	Date Range	$\delta^{15}N$ (‰ yr^{-1})	$\delta^{18}O$ (‰ yr^{-1})	$\delta^{15}N^{\alpha}$ (‰ yr^{-1})	$\delta^{15}N^{\beta}$ (‰ yr^{-1})
1.	1994-1998	-0.042 ± 0.004	-0.026 ± 0.005	-0.042 ± 0.007	-0.044 ± 0.005
2.	1952-2001	-0.039 ± 0.003	-0.022 ± 0.003	n/a	n/a
3.	1940-2008	-0.032 ± 0.004	-0.014 ± 0.008	-0.019 ± 0.015	-0.041 ± 0.020
4.	1990-2002	-0.040 ± 0.003	-0.021 ± 0.003	-0.014 ± 0.016	-0.063 ± 0.014
5.	1978-2005	-0.035 ± 0.002	-0.022 ± 0.004	-0.026 ± 0.013	-0.046 ± 0.015
6.	1978-1996	-0.041 ± 0.003	-0.020 ± 0.003	-0.067 ± 0.013	-0.013 ± 0.014

Study: 1. Rockmann et al. 2003; 2. Ishijima et al. 2007; 3. Prokopiou et al. 2017; 4. Rockmann and Levin 2005; 5. Park et al. 2012; 6. Cape Meares, Oregon (this work).

4.6.4 Sources of error

We tested the sensitivity of $\delta^{15}N^{\alpha}$ and $\delta^{15}N^{\beta}$ under several different scenarios which might explain the difference in trend in intramolecular compositions when comparing to other groups. One possibility is error in the scrambling coefficient (s = 8.3 ± 0.01) used in the numerically solved isotope ratios. The value of the scrambling coefficient helps contributes to the final $\delta^{15}N^{\alpha}$ and $\delta^{15}N^{\beta}$ values of each sample. To evaluate the sensitivity of the intramolecular isotopic composition on the scrambling coefficient, $\delta^{15}N^{\alpha}$ and $\delta^{15}N^{\beta}$ values were solved for using different values of s (0.04 – 0.18). The results of the scrambling sensitivity shown in table 4.11 give mean isotopic values and secular trends for different scrambling coefficients using the raw values (non-deseasonalized).

As the scrambling coefficient increases from 0.04 to 0.18, the mean $\delta^{15}N^{\alpha}$ value becomes enriched (15.1 - 18.5‰) while the mean $\delta^{15}N^{\beta}$ becomes depleted (-0.3‰ - -3.7‰). The secular trend in $\delta^{15}N^{\alpha}$ becomes more negative as the scrambling coefficient increases while the secular trend in $\delta^{15}N^{\beta}$ becomes more positive. However, even

adjusting the mean scrambling coefficient by a significant amount still produces secular trends for $\delta^{15}N^{\alpha}$ and $\delta^{15}N^{\beta}$ within their original respective 95% confidence intervals (table 4.7 and 4.11). This indicates that uncertainty of the scrambling coefficient is not responsible for the intramolecular trend differences to previously reported measurements.

Table 4.11. Intramolecular isotopic dependence on the scrambling coefficient.

	Category	s = 0.04	s = 0.08	s = 0.11	s = 0.14	s = 0.18
$\delta^{15}N^{\alpha}$	Mean (‰)	15.1	15.9	16.5	17.3	18.5
	Trend (‰ yr^{-1})	-0.065	-0.068	-0.070	-0.073	-0.077
$\delta^{15}N^{\beta}$	Mean (‰)	-0.3	-1.1	-1.7	-2.5	-3.7
	Trend (‰ yr^{-1})	-0.015	-0.012	-0.010	-0.007	-0.003

A second possibility could be the incorrect application of the numerical solving algorithm (Appendix B) used to convert the measured isotope ratios (^{45}R, ^{46}R, ^{31}R) to the desired isotopic composition ratios (^{15}R, ^{18}O, $^{15}R^{\alpha}$, $^{15}R^{\beta}$). To validate the numerical method, we used the reported scrambling coefficient (8.5%) and the measured isotope ratios (δ^{45}, δ^{46}, and δ^{31}) reported in Rockmann and Levin, 2005 (found through digitizing plotted data). We then applied our numerical solver sub-routine used with the Cape Meares dataset to calculate the intramolecular isotopic composition ratios reported in Rockmann and Levin (2005). The difference between resulting calculated $\delta^{15}N^{\alpha}$ and $\delta^{15}N^{\beta}$ values and those reported in Rockmann and Levin (2005) is less than 0.05‰ (error introduced through the data digitization process). This experiment effectively excludes error in the numerical solving algorithm from observed trends in $\delta^{15}N^{\alpha}$ and $\delta^{15}N^{\beta}$.

Directly comparing the measured isotopic composition values reported in Rockmann and Levin (2005) to the Cape Meares measurements reveals a large difference

in trend δ^{31} while δ^{45} and δ^{46} are similar (table 4.12). After ruling out scrambling within the ion source and sample size linearity (section 4.3) as possible reasons for the measured difference, we conclude the datasets represent different trends.

Table 4.12. Measured isotopic composition trends.

Study	Date Range	δ^{31} (N_2O) (‰ yr^{-1})	δ^{45} (N_2O) (‰ yr^{-1})	δ^{46} (N_2O) (‰ yr^{-1})
1.	1990-2002	-0.016 ± 0.011	-0.039 ± 0.004	-0.020 ± 0.004
2.	1978-1996	-0.060 ± 0.011	-0.041 ± 0.003	-0.020 ± 0.005

Study: 1. Rockmann and Levin, 2005; 2. Cape Meares, Oregon (this work).

A final way to definitively rule-out analytical differences between laboratories is to have several samples measured at another laboratory capable of high precision intramolecular N_2O isotopic measurements.

Chapter 5

N_2O Box Modeling

This chapter uses the results of the N_2O isotopic composition to infer how N_2O source changes have occurred over the years spanning samples measured for the OHSU-PSU Air Archive (1978-1996). To accomplish this, we apply a box modeling approach of atmospheric N_2O sources and sinks. Section 5.1 introduces the mathematics and physics of the box model and derives the equations used. Section 5.2 discusses the results and what conclusions may be made based on this modeling approach.

5.1 N_2O Box model method

Combining the measured concentration and isotopic composition of N_2O with simple modeling can be used to estimate the magnitude of source categories and their changes in time as well as infer contributions between nitrification and denitrification processes. Analysis of 1-box and 2-box models of the atmosphere have been used by several groups incorporating N_2O isotopic composition (Rahn and Wahlen, 2000; Sowers et al. 2002; Park et al. 2004; Rockmann and Levin, 2005; Park et al. 2012; Prokopiou et al. 2017). In this work, a 2-box model of the atmosphere is used with one box representing the troposphere and the second box representing the stratosphere.

The atmospheric budget for N_2O can be expressed using three main terms: the source, *S*; the sink, *L*; and the exchange of air between the troposphere and stratosphere, F_x. Mass conservation is preserved by defining the total number of molecules in the atmosphere as $M = 1.77\times10^8$ Tmol (Trenberth and Guillemot, 1994). Equations representing the change in N_2O concentration in each box are written as:

$$\frac{d}{dt}[N_2O]_T = \frac{S}{M_T}\times 10^9 - \frac{F_x}{M_T}([N_2O]_T - [N_2O]_S) \quad (5.1)$$

$$\frac{d}{dt}[N_2O]_S = \frac{F_x}{M_S}([N_2O]_T - [N_2O]_S) - \frac{(M_T[N_2O]_T + M_S[N_2O]_S)}{M_S\tau} \quad (5.2)$$

Where N_2O concentrations (in ppb) are represented by $[N_2O]$ with subscripts T and S indicate the troposphere and stratosphere, respectively. M_T and M_S represent the portion of the atmosphere in the troposphere and stratosphere (taken to be $0.85\times M$ and $0.15\times M$), respectively (Rockmann et al. 2003).

All N_2O sources, *S*, are in the troposphere as far as the global budget is concerned. Following the modeling method in Sowers et al. (2002), we can break the sources into 3 categories: ocean, terrestrial, and anthropogenic. While several groups combine the ocean and terrestrial sources into a single natural source category (Rockmann and Levin, 2005; Park et al. 2012; Prokopiou et al. 2017), these two natural sources have distinct isotopic compositions. If the natural sources are assumed constant in time, then splitting the natural source into separate categories offers no analytical insight. For simplicity, we will assume the natural sources remain constant.

The exchange of air between the troposphere and stratosphere is represented by F_x in equations 5.1 and 5.2. Estimates of the troposphere-stratosphere flux range between 1.4-2.8×10^{11} Tg yr^{-1} (Warneck, 1988; Holton et al. 1995; Appenzeller et al. 1996), or 0.22 Tmol s^{-1} (Rockmann et al. 2003). The only sink that affects the global budget takes place as loss in the stratosphere and is represented in the last term of equation 5.2. The atmospheric lifetime of N_2O (assumed constant at 123 years) is represented by τ.

Equations 5.1 and 5.2 are used to solve for the pre-industrial natural source terms by fixing the expected natural ocean source at 4.0 TgN yr^{-1} (Sowers et al. 2002) and solving the equations for the natural terrestrial source assuming the expected pre-industrial N_2O troposphere concentration of ~272 ppb (Sowers et al. 2002; Park et al. 2012; Ciais et al. 2013). This results in a natural terrestrial source of 6.6 TgN yr^{-1} and a total pre-industrial natural source of 10.6 TgN yr^{-1}. While our total pre-industrial source is higher than the estimated natural source of 9.0 ± 1.1 TgN yr^{-1} by Prather et al. (2012), our natural terrestrial source is identical to the value reported in the IPCC 2013 of 6.6 TgN yr^{-1} (Ciais et al. 2013).

The anthropogenic term is included starting in the year 1850 and is modeled as an exponential of the form:

(5.3) $$S_{Anth} = ae^{bt}$$

Where *a* and *b* are model fit parameters adjusted to fit the N_2O mole fraction observed at Cape Meares, Oregon after including firn air and ice core measurements used to match pre-industrial atmospheric concentrations (Macfarling-Meure et al. 2006; Ciais et al. 2013). The parameters are optimized using chi-square minimization. Chi-square minimization is found using:

(5.4) $$\chi^2 = \sum_{i=1}^{n} \frac{(O_i - E_i)^2}{\sigma_i^2}$$

Where O_i and E_i are the observed (measured) and expected (model) N_2O concentrations, respectively, and σ_i is the observed variance.

To estimate the uncertainty around the model, a confidence interval is found by applying the Chi-square minimization technique to the high and low bootstrapped LOWESS model values calculated in section 3.3.2. This provides a reliable range for the model that fits within the observed variability in the data.

Once the troposphere and stratosphere N_2O concentrations have been found, the equations are adjusted to solve for the different isotopic species. Equation 5.5 relates the bulk concentration, $[N_2O]$, to that of a specific species, $[N_2O]^*$, where *R* is the heavy to light isotopic ratio of the species in the atmosphere. Equation 5.6 relates the mean lifetime of the molecule, τ, to that of a specific isotopic species through the reaction time constant α.

(5.5) $$[N_2O]^* = [N_2O]R$$

$$\tau^* = \frac{\tau}{\alpha^*} \tag{5.6}$$

Using equations 5.5 and 5.6, we can now rewrite equations 5.1 and 5.2 as:

$$\frac{d}{dt}[N_2O]_T R_T = \frac{S}{M_T} R_{source} + \frac{F_x}{M_T}([N_2O]_S R_S - [N_2O]_T R_T) \tag{5.7}$$

$$\frac{d}{dt}[N_2O]_S R_S = \frac{F_x}{M_T}([N_2O]_S R_S - [N_2O]_T R_T) \ldots - \frac{\alpha}{M_S \tau}(M_T[N_2O]_T R_T + M_S[N_2O]_S R_S) \tag{5.8}$$

From here, the left-hand side of equations 5.7 and 5.8 are expanded using the calculus chain-rule:

$$\frac{d}{dt}[N_2O]R = [N_2O]\frac{d}{dt}R + R\frac{d}{dt}[N_2O] \tag{5.9}$$

For the troposphere, the last term in equation 5.9 is simply equation 5.1 times R_T while for the stratosphere, the last term in equation 5.9 is equal to equation 5.2 times R_S. Once we make these substitutions, we can solve for how R change in time:

$$\frac{d}{dt}R_S = \frac{F_x[N_2O]_T}{M_S[N_2O]_S}(R_T - R_S) + \frac{R_S}{[N_2O]_S M_S \tau}(M_T[N_2O]_T + M_S[N_2O]_S) - \frac{\alpha}{[N_2O]_S M_S \tau}(M_T[N_2O]_T R_T + M_S[N_2O]_S R_S) \tag{5.10}$$

$$\frac{d}{dt}R_S = \frac{F_x[N_2O]_T}{M_S[N_2O]_S}(R_T - R_S) + \frac{R_S}{[N_2O]_S M_S \tau}(M_T[N_2O]_T + M_S[N_2O]_S) - \frac{\alpha}{[N_2O]_S M_S \tau}(M_T[N_2O]_T R_T + M_S[N_2O]_S R_S) \tag{5.11}$$

The equations in 5.10 and 5.11 are coupled differential equations that can be solved together to model how the composition of different isotopomers of N_2O change in time. If we assume that the natural terrestrial and ocean source isotopic composition

remain constant in time, we can relate observed changes in the tropospheric composition, R_T, to the anthropogenic source magnitude and changes in the mean anthropogenic source composition, R_{Anth}.

5.2 N_2O Box model results

Box model results of the N_2O concentration at Cape Meares, Oregon are shown in figure 5.1. Firn air and ice core measurements are used to match pre-industrial atmospheric concentrations (Macfarling-Meure et al. 2006, Ciais et al. 2013). The model is optimized around three sets of data: the observations from Cape Meares, the model output of Prokopiou et al. 2017 prior to 1978 (40 data points), and measurements of firn air from Park et al. 2012 prior to 1978 (5 data points). This is done to provide a best match during the period of 1978 to 1997 while also preserving a realistic growth rate. This allows for some data-modeling mismatch in the spin-up period prior to 1950 compared to long-term data from Ciais et al. 2013 (fig. 5.1 (a), IPCC N_2O). The result is the model under-estimates the atmospheric concentration of N_2O between 1875 and 1950. This mismatch improves as the model approaches the period of study. Because we are only using the ice core and firn air measurements as our model initialization, the model results post 1950 should be sufficient to simulate the period of optimization (1978 to 1997).

From figure 5.1 (b), the box model is similar to that of the LOWESS fit (section 3.3.2). For the year 1980, the box model provides a N_2O concentration of 301.6 ± 0.3 ppb, while the LOWESS fit is 301.5 ± 0.3 ppb. For the year 1996, the box model N_2O concentration is 312.0 ± 0.5 ppb, while the LOWESS fit is 313.5 ± 0.3 ppb.

The total anthropogenic source calculated by the model for the years 1980 and 1996 is 3.8 ± 0.1 and 5.3 ± 0.1 TgN yr^{-1}, respectively. Figure 5.2 shows the total anthropogenic source calculated from the 2-box model as well as the total anthropogenic source calculated from EDGAR v4.3.2 (2017) (see Table A.4 in appendix). EDGAR gives a significantly larger global anthropogenic source for all years of interest (1978 to 1996), with a difference of 2.2 – 2.9 TgN yr^{-1}. This large difference is partly due to the optimization of our 2-box model around the observations from Cape Meares as well as the mismatch to data in the spin up period from firn air results (fig. 5.1a).

When modeling the isotopic composition of atmospheric N_2O, it is important to use the correct fractionation factor (α) that governs the rate of stratospheric loss for each isotopomer. Table 5.1 lists various fractionation factors reported by various studies as well as the values used in this study.

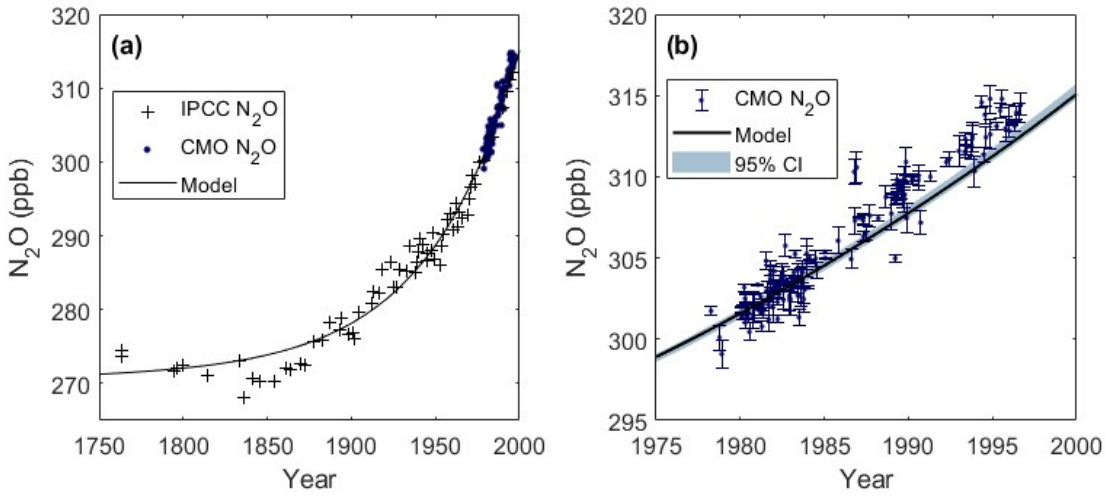

Figure 5.1. Box model results of atmospheric N_2O. Panel (a) shows the initial atmospheric conditions from ice core and firn air samples from Law Dome, Antarctica. Panel (b) displays the observation record at Cape Meares, Oregon.

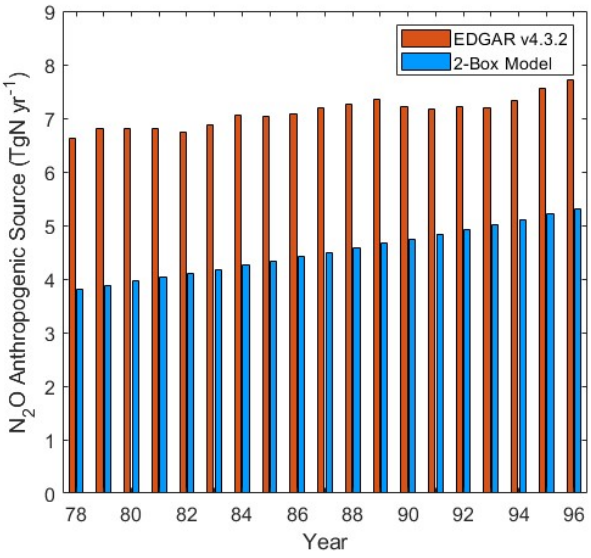

Figure 5.2. Global N_2O anthropogenic source (TgN yr^{-1}) between the years 1978 and 1996 calculated by EDGAR v4.3.2 (2017) and the 2-box model used in this study.

Table 5.1. Reported fractionation factors in the literature.

Study	α - ^{15}N	α - $^{15}N^{\alpha}$	α - $^{15}N^{\beta}$	α - ^{18}O
Rahn and Wahlen, 2000	0.9855	-	-	0.9871
Rockmann et al. 2003	0.9829	0.9787	0.9871	0.9860
Park et al. 2004	0.9851	0.9775	0.9929	0.9867
Toyoda et al. 2001, < 24.1 km	0.9841	0.9771	0.9912	0.9885
Toyoda et al. 2001, > 24.1 km	0.9714	0.9591	0.9845	0.9754
Kaiser et al. 2002, $O(^1D)$	0.9944	0.9978	0.9911	0.9876
Prokopiou et al. 2017	0.9838	0.9770	0.9906	0.9866
This Study	*0.9838*	*0.9770*	*0.9906*	*0.9866*

The isotopic compositions of the natural sources are kept constant over the run time of the model. Therefore, it is important that the pre-industrial atmospheric composition in the model reflects that of the observed composition from ice core measurements. Natural isotopic compositions reported in the literature are listed in table

1.2. The mean and standard deviations of the terrestrial and ocean sources are given in table 5.2. The values used in the model are presented in table 5.2 as well. The model's total natural source is calculated from the weighted sum of the ocean and terrestrial source, with 4.0 out of 10.6 TgN yr^{-1} contributed from the ocean and 6.6 out of 10.6 TgN yr^{-1} contributed from the terrestrial source.

A comparison of the total natural source used by two previous studies is given in table 5.3. The values used for the total natural sources of $\delta^{18}O$ and $\delta^{15}N^{\alpha}$ are comparable to those used by Prokopiou et al. (2017) and Park et al. (2012), $\delta^{15}N$ and $\delta^{15}N^{\beta}$ are roughly 1‰ enriched.

Table 5.2. Natural source isotopic compositions given in the literature and used in the model. Uncertainty represents 1σ of the reported values for the source category. The Total Natural source is flux weighted.

	From Table 1.2		Model Values		
Category (Natural)	**Ocean (‰)**	**Terrestrial (‰)**	**Ocean (‰)**	**Terrestrial (‰)**	**Total Nat. (‰)**
$\delta^{15}N$	3.6 ± 0.6	-9.2 ± 5.2	4.0	-12.3	-6.1
$\delta^{18}O$	42.4 ± 7.4	30 ± 13	31.9	31.9	31.9
$\delta^{15}N^{\alpha}$	8.7	-8.7 ± 5.2	3.0	-8.1	-3.9
$\delta^{15}N^{\beta}$	-2.3	-14.6 ± 10.5	5.0	-17.4	-8.9

Table 5.3. Natural source isotopic compositions reported by other groups and this study.

Category (Natural)	**Prokopiou et al. 2017**	**Park et al. 2012**	**This Study**
$\delta^{15}N$ (‰)	-5.2 ± 0.2	-5.3 ± 0.2	-6.1
$\delta^{18}O$ (‰)	33.1 ± 0.2	32 ± 0.2	31.9
$\delta^{15}N^{\alpha}$ (‰)	-1.9 ± 1.0	-3.3 ± 1.0	-3.9
$\delta^{15}N^{\beta}$ (‰)	-8.3 ± 1.1	-7.5 ± 1.1	-8.9

The modeled atmospheric compositions for the different isotopes of N_2O are shown in figure 5.3. A comparison of the box model results to that of the LOWESS fits calculated from the observed measurements from Cape Meares is provided in table 5.4.

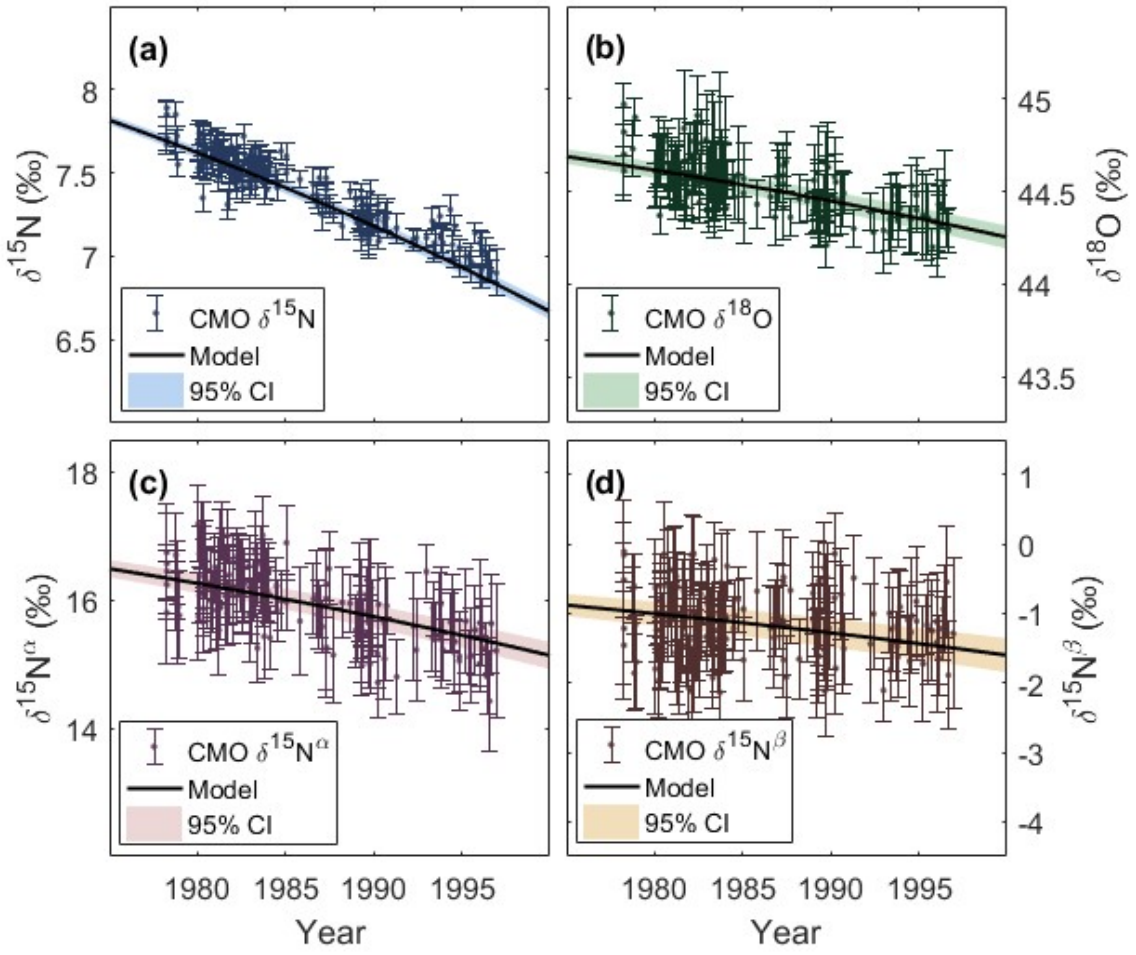

Figure 5.3. Box model results of the isotopic composition of atmospheric N_2O. Panels show $\delta^{15}N$ (a), $\delta^{18}O$ (b), $\delta^{15}N^{\alpha}$ (c), and $\delta^{15}N^{\beta}$ (d). Shaded regions represent the best fit of the box model to the 95% confidence interval estimates of the bootstrap fit calculations to the measured data.

The box model results closely reflect that of the LOWESS regression to the measured data for $\delta^{15}N$, $\delta^{18}O$, $\delta^{15}N^{\alpha}$, and $\delta^{15}N^{\beta}$ (fig. 4.16 and Table 5.4). This helps confirm that the model is working as intended by producing a good match with observations and trends. The close match between box model results and observations (LOWESS regression) also indicates the chi-square function is finding the best fit to the data based on model input parameters.

Table 5.4. Atmospheric isotopic composition for the years 1980 and 1996 calculated from box modeling and LOWESS fitting to observed atmospheric conditions at Cape Meares, Oregon. Box model uncertainty represents the model fit to the 95% confidence interval around the LOWESS fit.

Category		1980 (‰)	1996 (‰)
$\delta^{15}N$ (‰)	Box Model	7.59 ± 0.03	6.96 ± 0.04
	LOWESS	7.61 ± 0.03	6.99 ± 0.02
$\delta^{18}O$ (‰)	Box Model	44.61 ± 0.05	44.35 ± 0.06
	LOWESS	44.64 ± 0.03	44.36 ± 0.03
$\delta^{15}N^{\alpha}$ (‰)	Box Model	16.2 ± 0.2	15.4 ± 0.2
	LOWESS	16.3 ± 0.1	15.3 ± 0.1
$\delta^{15}N^{\beta}$ (‰)	Box Model	-1.0 ± 0.2	-1.4 ± 0.3
	LOWESS	-1.0 ± 0.1	-1.3 ± 0.1

The flux weighted isotopic composition of the anthropogenic source found through chi-square minimization of the model to the observed measurements is given in table 5.5 as well as values reported in Park et al. (2012) and Prokopiou et al. (2017) for comparison. The model results of anthropogenic source $\delta^{15}N$, $\delta^{18}O$, and $\delta^{15}N^{\alpha}$ for Cape Meares match reasonably well with results from Prokopiou et al. (2017) and Park et al. (2012). However, our modeled anthropogenic source $\delta^{15}N^{\beta}$ is 6.6‰ and 12.2‰ enriched compared with Park et al. (2012) and Prokopiou et al. (2017), respectively.

The simple box models used by Park et al. (2012) and Prokopiou et al. (2017) assume a constant isotopic composition for both the anthropogenic and natural sources over the entire time span (as does this model). While this makes the calculations more simplistic, it does not accurately capture variability from individual source categories over the period of interest. If the measurements of intramolecular isotopic composition presented here are correct, these results suggest that increases in N_2O sources may not be linear despite the observed linear increase in N_2O mole fraction.

Table 5.5. Anthropogenic source isotopic compositions reported by other groups and this study.

Category (Anthropogenic)	Prokopiou et al. 2017	Park et al. 2012	This Study
$\delta^{15}N$ (‰)	-18.2 ± 2.6	-15.6 ± 1.2	-15.0 ± 0.3
$\delta^{18}O$ (‰)	27.2 ± 2.6	32.0 ± 1.3	33.3 ± 0.4
$\delta^{15}N^{\alpha}$ (‰)	-8.1 ± 1.7	-7.6 ± 6.2	-12.8 ± 1.5
$\delta^{15}N^{\beta}$ (‰)	-26.1 ± 8.4	-20.5 ± 7.1	-13.9 ± 1.7

Finally, we can calculate the SP of both the flux weighted natural and anthropogenic sources from the model and compare to previously published values. Table 5.6 gives the SP of the natural and anthropogenic sources from Prokopiou et al. (2017), Park et al. (2012), and this study. Box modeling of Cape Meares results shows the natural and anthropogenic sources to have a SP of 4.9‰ and 1.1 ± 2.3‰ respectively. The natural source SP from our box model is similar to that of Prokopiou et al. (2017) and Park et al. (2012) while the anthropogenic source SP is significantly depleted (16.9 – 12.0‰). This result is similar to that of the secular trends discussed in section 4.5.3. A positive secular trend indicates the anthropogenic SP is greater than the natural SP where a negative secular trend indicates the anthropogenic SP is less than the natural SP. From

table 4.9, the deseasonalized secular trend of SP at Cape Meares is -0.064 ± 0.028‰. While the model represents the Cape Meares dataset well, this result is very different than observed previously. It should also be noted that the modeling time periods used in Prokopiou et al. 2017 (1940 – 2008) and Park et al. 2012 (1940 – 2005) are different than the model used for Cape Meares (optimized between 1978 – 1997). This time difference may explain some of the difference between results.

Table 5.6. SP for natural and anthropogenic sources reported by other groups and this study.

Category	Prokopiou et al. 2017	Park et al. 2012	This Study
SP (Nat. ‰)	6.4 ± 1.5	4.2 ± 1.5	4.9
SP (Anth. ‰)	18.0 ± 8.6	13.1 ± 9.4	1.1 ± 2.3

The results from the box modeling presented here are uncertain as the model used does not represent changes in time to individual source categories (i.e. changing contributions from fossil fuels, biomass burning, agriculture, etc.). While improvements can be made to the model, the results suggest the SP of the anthropogenic source is similar to that of the natural source. This result is important to our understanding of contributions from nitrification and denitrification processes to the observed atmospheric N_2O composition. If laboratory measurements of SP are globally relevant, a small positive trend in SP is associated with an increasing influence from nitrification processes (Sutka et al. 2006; Park et al. 2012; Prokopiou et al 2017). These results would suggest there has not been significant changes to the balance between contributions from nitrification and denitrification to the observed isotopic composition of N_2O at Cape Meares during the 1978 – 1996 period.

Chapter 6

Conclusions

Presented here are 159 samples from the OHSU-PSU Air Archive from Cape Meares, Oregon (45.5° N, 124.0° W) measured for N_2O and SF_6 mole fraction (using GC-μECD) and N_2O intramolecular isotopic composition (using continuous flow IRMS) spanning April 1978 to December 1996.

The GC-μECD system designed through this work is fully automated, capable of running multiple pressurized samples per run. Measurement precision of N_2O and SF_6 is 0.16% and 1.1% respectively. Sample concentrations were corrected for detector response non-linearity when measured against our reference gas. The linearity correction was found to be 0.14 ppb ppb^{-1} and 0.03 ppt ppt^{-1} for N_2O and SF_6, respectively.

Analysis of archived air samples finds the mole fraction of N_2O in 1980 to be 301.5 ± 0.3 ppb (1σ) and rises to 313.5 ± 0.3 ppb (1σ) in 1996. The average growth rate over this period is 0.78 ± 0.03 ppb yr^{-1} (95% CI). Seasonality shows peak amplitude of 0.3 ppb near April and minimum amplitude of -0.4 ppb near November and is statistically robust. Our measurements of N_2O were found to match well with previously reported values for Cape Meares and other comparable northern hemisphere mid-latitude locations.

For SF_6, the concentration in 1980 is found to be 0.85 ± 0.03 ppt (1σ), increasing to 3.83 ± 0.03 ppt (1σ) in 1996. The average growth rate over this period is 0.17 ± 0.01 ppt yr^{-1} (95% CI). Seasonality shows peak amplitude of 0.04 ppb near January and minimum amplitude of -0.03 ppt near July. There are no previous reported measurements of SF_6 from Cape Meares to compare against directly. SF_6 measurements compare well to

other northern hemisphere measurements from Levin et al. (2010), Rigby et al. (2010), and Hall et al. (2011) over similar time periods when including spatial variability. From these N_2O and SF_6 measurements, we can conclude the sample integrity is robust within the OHSU-PSU Air Archive from Cape Meares, Oregon. Resulting dataset of SF_6, in particular, contributes to a better characterization of historic SF_6 growth rate and its atmospheric variability over this period of dramatic growth.

A GC-IRMS in combination with a preconcentration system was designed and used to evaluate the intramolecular composition of N_2O for this work. In the isotopic analysis, repeated measurements of a working standard (CC2854) results show that the residual distributions of the measured isotopologues are normal with typical 1σ measurement precision of 0.05‰, 0.10‰, and 0.28‰ for δ^{45}, δ^{46}, and δ^{31}, respectively. For the sample size range used, the achieved measurement precision is ~2x (δ^{45} and δ^{46}) and ~3x (δ^{31}) the theoretically maximum achievable precision of the instrument. There was no sample size linearity correction needed over the sample size range used.

The typical isotopic composition precisions (1σ) for a standard are 0.05‰, 0.10‰, 0.37‰, and 0.39‰ for $\delta^{15}N$, $\delta^{18}O$, $\delta^{15}N^{\alpha}$, and $\delta^{15}N^{\beta}$, respectively. Typical measurement precisions for OHSU-PSU archive samples are 0.07‰, 0.15‰, 0.57‰, and 0.60‰ for $\delta^{15}N$, $\delta^{18}O$, $\delta^{15}N^{\alpha}$, and $\delta^{15}N^{\beta}$, respectively. Isotopic results from the Cape Meares archive add significantly to timeseries data during the 1980 and 1990 time periods.

No distinguishable seasonality is found in $\delta^{15}N$ or $\delta^{18}O$ while $\delta^{15}N^{\alpha}$ and $\delta^{15}N^{\beta}$ show statistically significant amplitudes with nearly opposite phases to one another. $\delta^{15}N^{\alpha}$ has a maximum amplitude of 0.2 ± 0.2‰ (1σ) near April and a minimum amplitude

of -0.3 ± 0.3‰ (1σ) near November. $\delta^{15}N^{\beta}$ has a maximum amplitude of 0.2 ± 0.2‰ (1σ) near November and a minimum amplitude of -0.2 ± 0.2‰ (1σ) near April. The SP also shows a statistically significant seasonality, with a maximum of 0.3 ± 0.2‰ (1σ) near April and a minimum of -0.4 ± 0.2‰ (1σ) near November. These results suggest that at Cape Meares during the spring, processes that contribute air enriched in N_2O mole fraction also contribute enriched $\delta^{15}N^{\alpha}$ and depleted $\delta^{15}N^{\beta}$, causing a positive SP. During the fall, possesses that contribute air depleted in N_2O mole fraction also contribute depleted $\delta^{15}N^{\alpha}$ and enriched $\delta^{15}N^{\beta}$, causing a negative SP.

All annual trends, besides $\delta^{15}N$, are indistinguishable from 0‰ yr^{-1} for isotopic compositions. This is due in part to the larger measurement uncertainty in the intramolecular isotopic compositions. All secular trends, besides $\delta^{15}N^{\beta}$, calculated by applying a linear fit to the deseasonalized data show negative trends statistically different from 0. The secular trend values for $\delta^{15}N$, $\delta^{18}O$, $\delta^{15}N^{\alpha}$, $\delta^{15}N^{\beta}$, and SP are -0.041 ± 0.003‰ yr^{-1}, -0.020 ± 0.003‰ yr^{-1}, -0.067 ± 0.013‰ yr^{-1}, -0.013 ± 0.014‰ yr^{-1}, and -0.064 ± 0.028‰ yr^{-1}, respectively. Secular trends for $\delta^{15}N$ and $\delta^{18}O$ match well with previously reported values (Rockmann et al. 2003; Rockmann and Levin 2005; Ishijima et al. 2007; Park et al. 2012; Prokopiou et al. 2017). Secular trends for $\delta^{15}N^{\alpha}$ and $\delta^{15}N^{\beta}$ for Cape Meares are significantly different than those reported by other groups, appearing to be nearly inverted for $\delta^{15}N^{\alpha}$ and $\delta^{15}N^{\beta}$ compared with one group.

To address this difference compared to previous published results, the sensitivity of the numerically calculated $\delta^{15}N^{\alpha}$ and $\delta^{15}N^{\beta}$ on the scrambling coefficient was investigated and found to not be a possible cause. We also investigated the possibility of an error in the numerical algorithm used to convert measured ^{45}R, ^{46}R, and ^{31}R values

into $\delta^{15}N$, $\delta^{18}O$, $\delta^{15}N^{\alpha}$, $\delta^{15}N^{\beta}$. To validate the numerical method, we used the reported scrambling coefficient (8.5%) and the measured isotope ratios reported in Rockmann and Levin (2005) (found through digitizing plotted data). The difference between the script calculated and Rockmann and Levin (2005) reported $\delta^{15}N^{\alpha}$ and $\delta^{15}N^{\beta}$ values is less than 0.05‰, matching within variability in the data digitization process. This excludes error in the numerical solving algorithm as a possible reason for the observed difference.

Directly comparing the measured isotopic composition values reported in Rockmann and Levin (2005) to the Cape Meares measurements reveals a difference in trend in $^{31}\delta$ while $^{45}\delta$ and $^{46}\delta$ are similar (table 4.12). After ruling out scrambling within the ion source and sample size linearity (section 4.3) as possible reasons for the measured difference, we conclude the datasets represent different trends. One possibility to further confirm this result is to have several samples measured at another laboratory capable of high precision intramolecular N_2O isotopic measurements, of which there are only a handful of laboratories in the world.

Finally, a 2-box model of the atmosphere was used to investigate changes in measured atmospheric composition to characterize source isotopic composition. For simplicity, the natural source was assumed to remain constant in magnitude and isotopic composition since the pre-industrial age. We also assumed the anthropogenic source had a constant isotopic composition over the span of the model. While these assumptions do not accurately reflect how the average source can change in composition over time, the results are still useful to determine a broad characterization of source isotopic composition and compare with previously published values.

From the results of the box model, the magnitude of the pre-industrial natural source is 10.6 TgN yr^{-1} (4.0 TgN yr^{-1} from ocean, 6.6 TgN yr^{-1} from terrestrial) while the anthropogenic source in 1996 contributes 5.3 ± 0.1 TgN yr^{-1}. These values are within the ranges of expected source magnitudes given by the IPCC (Ciais et al. 2013) and suggest the model represents reasonable estimates.

The isotopic compositions of the natural source for $\delta^{15}N$, $\delta^{18}O$, $\delta^{15}N^{\alpha}$, $\delta^{15}N^{\beta}$ that best match expected atmospheric compositions was found to be -6.1‰, 31.9‰, -3.9‰, -8.9‰, respectively. These are similar to natural source compositions previously reported (Park et al. 2012; Prokopiou et al. 2017). The isotopic compositions of the anthropogenic source for $\delta^{15}N$, $\delta^{18}O$, $\delta^{15}N^{\alpha}$, $\delta^{15}N^{\beta}$ was found to be -15.0 ± 0.3‰, 33.3 ± 0.4‰, -12.8 ± 1.5‰, and -13.9 ± 1.7‰, respectively. The modeled anthropogenic $\delta^{15}N$, $\delta^{18}O$, $\delta^{15}N^{\alpha}$ match reasonably well with results from Prokopiou et al. (2017) and Park et al. (2012). However, our modeled $\delta^{15}N^{\beta}$ is significantly enriched compared to the previously reported values.

Box modeling at Cape Meares shows the natural and anthropogenic sources to have a SP of 4.9‰ and 1.1 ± 2.3‰, respectively. While the natural source SP resembles the results from Prokopiou et al. (2017) and Park et al. (2012), the anthropogenic SP is significantly depleted. Assuming the laboratory measurements of intramolecular SP are globally relevant, these results suggest there were not significant changes to the balance between contributions from nitrification and denitrification to the observed isotopic composition of N_2O during the period of interest (1978 – 1996).

References

Baertschi, P. (1976), Absolute O-18 content of standard mean ocean water, Earth Planet. Sci. Lett., 31(3), 341-344.

Bol, R., S. Toyoda, S. Yamulki, J. Hawkins, L. Cardenas, and N. Yoshida (2003), Dual isotope and isotopomer ratios of N_2O emitted from a temperate grassland soil after fertiliser application. Rapid Commun. Mass Spectrom., 17(22), 2550-2556.

Bol, R., T. Rockmann, M. Blackwell, and S. Yamulki (2004), Influence of flooding on $d^{15}N$, $d^{18}O$, $1d^{15}N$ and $2d^{15}N$ signatures of N_2O released from estuarine soils—A laboratory experiment using tidal flooding chambers. Rapid Commun. Mass Spectrom., 18(14), 1561-1568.

Butenhoff, C. and M. A. K. Khalil (2007), Stratospheric Sinks of Nitrous Oxide [Chapter 14]. In Reay, D. et al. Greenhouse Gas Sinks. 207-224. Cambridge, MA: CABI

Ciais, P., et al. (2013), Carbon and other biogeochemical cycles, in Climate Change 2013: The Physical Science Basis. Contribution of Working Group I to the Fifth Assessment Report of the Intergovernmental Panel on Climate Change, edited by T. F. Stocker et al., pp. 465–570, Cambridge Univ. Press, Cambridge, U. K. and New York, NY, USA.

Cliff, S. and M. Thiemens (1997), The 18O/16O and 17O/16O ratios in atmospheric nitrous oxide: a mass-independent anomaly. Science, 278(5344), 1774-1776.

Crutzen, P. J. (1970), Influence of nitrogen oxides on atmospheric ozone content. Q. J. R. Meteorol. Soc., 96(408), 320–325, doi: 10.1002/qj.49709640815

Cleveland, W. S. and S. J. Devlin (1988), Locally Weighted Regression: an approach to regression analysis by local fitting. Journal of the American Statistical Association, 83(403), 596-610.

Davidson, E., and D. Kanter (2009), The contribution of manure and fertilizer nitrogen to atmospheric nitrous oxide since 1860. Nature Geoscience, 2(9), 659.

EDGAR (2013), Emission Database for Global Atmospheric Research (EDGAR): European Commission, Joint Research Centre (JRC)/Netherlands Environmental Assessment Agency (PBL), release version 4.2. http://edgar.jrc.ec.europa.eu

EDGAR (2017), Emission Database for Global Atmospheric Research (EDGAR): European Commission, Joint Research Centre (JRC)/Netherlands Environmental Assessment Agency (PBL), release version 4.3.2. http://edgar.jrc.ec.europa.eu

Estupiñán, E., J. Nicovich, J. Li, D. Cunnold, and P. Wine (2002), Investigation of N2O production from 266 and 532 nm laser flash photolysis of O3/N2/O2 mixtures, J. Phys. Chem. A, 106(24), 5880 – 5890.

Freing, A., D. Wallace, and H. Bange (2012), Global oceanic production of nitrous oxide. Phil. Trans. R. Soc. B, 367(1593), 1245–1255.

Galloway, J., W. Schlesinger, H. Levy, A. Michaels, J. Schnoor, et. al. (1995), Nitrogen fixation: anthropogenic enhancement - environmental response. Global Biochemical Cycles, 9(2), 235-252.

Geller, L., J. Elkins, J. Lobert, A. Clarke, D. Hurst, J. Butler, and R. Myers (1997), Tropospheric SF6: Observed latitudinal distribution and trends, derived emissions and interhemispheric exchange time. Geophys. Res. Lett.,24(6), 675-678.

Goldberg, S., K. Knorr, and G. Gebauer (2008), N_2O concentration and isotope signature along profiles provide deeper insight into the fate of N_2O in soils. Isotopes in Environmental and Health Studies, 44(4), 377-391, doi: 10.1080/10256010802507433

Gutierrez, M., D. Baxter, C. Hunter, and K. Svoboda (2005), Nitrous oxide (N2O) emissions from waste and biomass to energy plants. Waste Management and Research, 23, 133–147.

Hall, B. D., G. S. Dutton, and J. W. Elkins (2007), The NOAA nitrous oxide standard scale for atmospheric observations. J. Geophys. Res., 112, D09305, doi:10.1029/2006JD007954

Hall, B. D., G. S. Dutton, D. J. Mondeel, J. D. Nance, M. Rigby, J. H. Butler, et al. (2011), Improving measurements of SF6 for the study of atmospheric transport and emissions. Atmos. Meas. Tech., 4(11), 2441-2451, doi:10.5194/amt-4-2441-2011

Hirsch, A., A. Michalak, L. Bruhwiler, W. Peters, E. Dlugokencky, and P. Tans (2006), Inverse modeling estimates of the global nitrous oxide surface flux from 1998–2001. Global Biogeochemical Cycles, 20, GB1008.

Ishijima, K., Sugawara, S., Kawamura, K., Hashida, G., Morimoto, S., Murayama, S., Aoki, S., and Nakazawa, T. (2007), Temporal variations of the atmospheric nitrous oxide concentration and its δ 15 N and δ 18 O for the latter half of the 20th century reconstructed from firn air analyses. Journal of Geophysical Research: Atmospheres, 112(D3), 10.1029/2006JD007208.

Ishijima K., T. Nakazawa, and S. Aoki (2009), Variations of atmospheric nitrous oxide concentration in the northern and western Pacific. Tellus, 61B, 408–415.

Jiang, X., W. L. Ku, R.-L. Shia, Q. Li, J. W. Elkins, R. G. Prinn, and Y. L. Yung (2007), Seasonal cycle of N2O: Analysis of data. Global Biogeochem. Cy., 21, GB1006, doi:l0.1029/2006GB002691

Junk, G. and H. J. Svec (1958), The absolute abundance of the nitrogen isotopes in the atmosphere and compressed gas from various sources, Geochim. Cosmochim. Acta., 14 (3), 234-243.

Kim, J. and H. Craig (1993), Nitrogen-15 and oxygen-18 characteristics of nitrous oxide: A global perspective. Science, 262(5141), 1855-1857.

Kaiser, J., C. Brenninkmeijer, and T. Rockmann (2002a), Intramolecular 15N and 18O fractionation in the reaction of N2O with O(1D) and its implications for the stratospheric N2O isotope signature. J. Geophys. Res., 107(D14), 4214.

Kaiser, J., T. Rockmann, and C. Brenninkmeijer (2002b), Temperature dependence of isotope fractionation in N2O photolysis. Physical Chemistry Chemical Physics, 4(18), 4220-4230.

Kaiser, J., T. Rockmann, C. Brenninkmeijer, and P. Crutzen (2003a), Wavelength dependence of isotope fractionation in N_2O photolysis. Atmos. Chem. Phys., 3, 303-313.

Kaiser, J., T. Rockmann, and C. Brenninkmeijer (2003b), Complete and accurate mass-spectrometric isotope analysis of tropospheric nitrous oxide. J. Geophys. Res., 108(D15), 4476.

Kaiser, J., T. Rockmann, and C. Brenninkmeijer (2004), Contribution of mass-dependent fractionation to the oxygen isotope anomaly of atmospheric nitrous oxide. J. Geophys. Res., 109, D03305.

Kaiser, J., A. Engel, R. Borchers, and T. Rockmann (2006), Probing stratospheric transport and chemistry with new balloon and aircraft observations of the meridional and vertical N_2O isotope distribution. Atmos. Chem. and Phys., 6, 3535-3556.

Khalil, M. A. K., and R. A. Rasmussen (1983), Increase and seasonal cycles of nitrous oxide in the earth's atmosphere. Tellus, 35B, 161-169.

Khalil, M. A. K., and R. A. Rasmussen 1988), Nitrous oxide: trends and global mass balance over the last 3000 years. Annals of Glaciology, 10, 73-79, doi: 10.1017/S0260305500004201

Khalil, M. A. K., R. A. Rasmussen, and M. J. Shearer (2002), Atmospheric nitrous oxide: patterns of global change during recent decades and centuries. Chemosphere, 47, 807–821.

Kovács, T., Feng, W., Totterdill, A., Plane, J. M. C., Dhomse, S., Gómez-Martín, J. C., Stiller, G. P., Haenel, F. J., Smith, C., Forster, P. M., García, R. R., Marsh, D. R., and Chipperfield, M. P. (2017), Determination of the atmospheric lifetime and global warming potential of sulfur hexafluoride using a three-dimensional model, Atmos. Chem. Phys., 17, 883-898, https://doi.org/10.5194/acp-17-883-2017.

Kroeze, C., A. Mosier, and L. Bouwman (1999), Closing the global N2O budget: A retrospective analysis 1500–1994. Global Biogeochemical Cycles, 13(1), 1-8, doi: 10.1029/1998GB900020

Levin, I. and V. Hesshaimer (1996), Refining of atmospheric transport model entries by the globally observed passive tracer distributions of 85krypton and sulfur hexafluoride (SF6). J. Geophys. Res. Atmospheres, 101(D11), 16745-16755, doi: 10.1029/96JD01058

Levin, I., T. Naegler, R. Heinz, D. Osusko1, E. Cuevas, A. Engel et al. (2010), The global SF6 source inferred from long-term high precision atmospheric measurements and its comparison with emission inventories. Atmos. Chem. and Phys., 10, 2655–2662.

Li, W-J, B. Ni, D. Jin, and T.-L. Chang (1988), Measurement of the absolute abundance of O17 in VSMOW, Chin. Sci. Bull., 33, 1610-1613.

Liao, T., C. Camp, and Y. Yung (2004), The seasonal cycle of N2O. Geophys. Res. Lett., 31, L17108, doi: 10.1029/2004GL020345

Lueker, T., S. Walker, M. Vollmer, R. Keeling, C. Nevison, R. Weiss, and H. Garcia (2003), Coastal upwelling air-sea fluxes revealed in atmospheric observations of O2/N2, CO2, and N2O. Geophys. Res. Lett., 30(6), 1292, doi: 10.1029/2002GL016615

Maiss, M., L. P. Steele, R. Francey, P. Fraser, R. Langenfelds, N. Trivett, and I. Levin (1996), Sulfur hexafluoride – a powerful new atmospheric tracer. Atmos. Environ., 30(10), 1621–1629, doi: 10.1016/1352-2310(95)00425-4

Maiss, M. and C. Brenninkmeijer (1998), Atmospheric SF6: Trends, sources, and prospects. Environ. Sci. Technol., 32(20), 3077– 3086.

Macfarling-Meure, C., D. Etheridge, C. Trudinger, P. Steele, R. Langenfelds, T. Van Ommen, et al. (2006), Law Dome CO2 , CH4 and N2O ice core records extended to 2000 years BP. Geophys. Res. Lett., 33(14), doi: 10.1029/2006GL026152

Miller, C. and Y. Yung (2000), Photo-induced isotopic fractionation. J. Geophys. Res., Atmospheres, 105(D23), 29039-29051.

Minschwaner, K., R. Salawitch, and M. McElroy (1993), Absorption of solar radiation by O2: Implications for O3 and lifetimes of N2O, CFCl3, and CF2Cl2, J. Geophys. Res., 98(D6), 10543-10561.

Myhre, G. et al. (2013), Anthropogenic and Natural Radiative Forcing, in Climate Change 2013: The Physical Science Basis. Contribution of Working Group I to the Fifth Assessment Report of the Intergovernmental Panel on Climate Change, edited by T. F. Stocker et al., pp 659-740, Cambridge Univ. Press, Cambridge, U. K. and New York, NY, USA.

Nevison, C., E. Keim, S. Solomon, D. Fahey, J. Elkins, M. Loewenstein, and J. Podolske (1999), Constraints on N2O sinks inferred from observed tracer correlations in the lower stratosphere. Global Biogeochemical Cycles, 13(3), 737-742.

Nevison, C., J. Butler, and J. Elkins (2003), Global distribution of N2O and the ΔN2O-AOU yield in the subsurface ocean. Global Biogeochemical Cycles, 17(4), 1119.

Nevison, C., D. Kinninson, and R. Weiss (2004), Stratospheric influences on the tropospheric seasonal cycles of nitrous oxide and chlorofluorocarbons. Geophys. Res. Lett., 31(20), doi: 10.1029/2004GL020398

Nevison, C., R. Keeling, R. Weiss, B. Popp, X. Jin, P. Fraser, L. Porter, and P. Hess (2005). Southern Ocean ventilation inferred from seasonal cycles of atmospheric N2O and O2/N2 at Cape Grim, Tasmania. Tellus B: Chemical and Physical Meteorology, 57(3), 218-229.

Nevison, C., N. Mahowald, R. Weiss, and R. Prinn (2007), Interannual and seasonal variability in atmospheric N2O. Global Biogeochem. Cycles, 21(3), doi: 10.1029/2006GB002755

Nevison, C., E. Dlugokenecky, G. Dutton, J. Elkins, P. Fraser, B. Hall, et al. (2011), Exploring causes of interannual variability in the seasonal cycles of tropospheric nitrous oxide. Atmos. Chem. Phys. 11, 3713–3730.

Ogawa, M., and N. Yoshida (2005a), Intramolecular distribution of stable nitrogen and oxygen isotopes of nitrous oxide emitted during coal combustion. Chemosphere, 61, 877-887.

Ogawa, M., and N. Yoshida (2005b), Nitrous oxide emission from the burning of agricultural residue. Atmospheric Environment, 39, 3421-3429.

Olivier, J., A. Bouwman, K. Van Der Hoek, & J. Berdowski (1998), Global air emission inventories for anthropogenic sources of NOx, NH3 and N2O in 1990. Environmental Pollution, 102, 135-148.

Olivier, J., J. Van Aardenne, F. Dentener, V. Pagliari, L. Ganzeveld, and J. Peters (2005), Recent trends in global greenhouse gas emissions:regional trends 1970–2000 and spatial distribution of key sources in 2000. Environ. Sci., 2(2-3), 81-99, doi: 10.1080/15693430500400345

Opdyke, M., N. Ostrom, and P. Ostrom (2009), Evidence for the predominance of denitrification as a source of N2O in temperate agricultural soils based on isotopologue measurements. Global Biogeochem. Cycles, 23, GB4018.

Park, S., E. Atlas, and K. Boering (2004), Measurements of N2O isotopologues in the stratosphere: Influence of transport on the apparent enrichment factors and the isotopologue fluxes to the troposphere. J. Geophys. Res., 109, 462-464.

Park, S., T. Pérez, K. Boering, S. Trumbore, J. Gil, S. Marquina, and S. Tyler (2011), Can N2O stable isotopes and isotopomers be useful tools to characterize sources and microbial pathways of N2O production and consumption in tropical soils? Global Biogeochemical Cycles, 25(1), doi: 0.1029/2009GB003615

Park, S., P. Croteau, K. Boering, D. Etheridge, D. Ferretti, P. Fraser, K. Kim, et al. (2012), Trends and seasonal cycles in the isotopic composition of nitrous oxide since 1940. Nature Geoscience, 5, 261-265, doi: 10.1038/NGEO1421

Patra, P., M. Takigawa, G. S. Dutton, K. Uhse, K. Ishijima, B. R. Lintner, et al. (2009), Transport mechanisms for synoptic, seasonal and interannual SF6 variations and "age" of air in troposphere. Atmos. Chem. and Phys., 9, 1209–1225.

Patra, P., S. Houweling, M. Krol, P. Bousquet, D. Belikov, D. Bergmann, et al. (2011), TransCom model simulations of CH4 and related species: Linking transport, surface flux and chemical loss with CH4 variability in the troposphere and lower stratosphere. Atmos. Chem. and Phys.,11(24), 12813-12837.

Perez, T., S. Trumbore, S. Tyler, P. Matson, I. Ortiz-Monasterio, T. Rahn, and D. Griffith (2001), Identifying the agricultural imprint on the global N2O budget using stable isotopes. J. Geophys. Res., 106, 9869-9878.

PFEL, Pacific Fisheries Environmental Laboratory, NOAA. Retrieved from: https://www.pfeg.noaa.gov/products/PFEL/modeled/indices/upwelling/NA/upwell_menu_NA.html

Popp, B., M. Westley, S. Toyoda, T. Miwa, J. Dore, N. Yoshida, et al. (2002), Nitrogen and oxygen isotopomeric constraints on the origins and sea-to-air flux of N2O in the oligotrophic subtropical North Pacific gyre. Global Biogeochemical Cycles, 16, doi: 2001GB001806

Potter, K. E., Ono, S., and Prinn, R. G. (2013), Fully automated, high-precision instrumentation for the isotopic analysis of tropospheric N2O using continuous flow isotope ratio mass spectrometry. Rapid Commun. Mass Spectrom, 27, 1723-1738.

Prather, M., C. Holmes, and J. Hsu (2012), Reactive green house gas scenarios: Systematic exploration of uncertainties and the role of atmospheric chemistry. Geophys. Res. Lett., 39, L09803, doi: 10.1029/2012GL051440

Prather, M., J. Hsu, N. DeLuca, C. Jackman, L. Oman, A. Douglass, A., et al. (2015), Measuring and modeling the lifetime of nitrous oxide including its variability. J. Geophys. Res. Atmospheres, 120(11), 5693-5705, doi: 10.1002/ 2015JD023267

Prinn, R., D. Cunnold, R. Rasmussen, P. Simmonds, F. Alyea, A. Crawford, et al. (1990), Atmospheric emissions and trends of nitrous oxide deduced from 10 years of ALE-GAGE data. J. Geophys. Res., 95, 18369-18.

Prinn, R., R. Weiss, P. Fraser, P. Simmonds, D. Cunnold, F. Alyea, et. al. (2000), A history of chemically and radiatively important gases in air deducted from ALE/GAGE/AGAGE. J. Geophys. Res., 105: 17751-17792, doi: 10.1029/2000JD900141

Prokopiou, M., P. Martinerie, C. J. Sapart, E. Witrant, G. Monteil, K. Ishijima, S. Bernard, J. Kaiser, I. Levin, T. Blunier, D. Etheridge, E. J. Dlugokencky, R. Van De

Wal, S. W. Roderik, and T. Röckmann (2017). Constraining N2O emissions since 1940 using firn air isotope measurements in both hemispheres. Atmospheric Chemistry And Physics, 17(7), 4539-4564.

Rahn, T. and M. Wahlen (2000), A reassessment of the global isotopic budget of atmospheric nitrous oxide. Global Biogeochemical Cycles, 14(2) 537-543.

Ray, E., Moore, F. L., Elkins, J. W., Rosenlof, K. H., Laube, J. C., Röckmann, T., Marsh, D. R., and Andrews. A. E. (2017), Quantification of the SF6 Lifetime Based on Mesospheric Loss Measured in the Stratospheric Polar Vortex, J. Geophys. Res.-Atmos., 122(8), 4626-4638, doi:10.1002/2016JD026198.

Ravishankara, A., S. Solomon, A. Turnipseed, and R. Warren (1993), The atmospheric lifetimes of long-lived halogenated species. Science, 259, 194–199.

Rigby, M., J. Muhle, B. Miller, R. Prinn, P. Krummel, L. Steele, et al. (2010), History of atmospheric SF6 from 1973 to 2008. Atmos. Chem. and Phys., 10, 10305–10320.

Rock, L., B. Ellert, B. Mayer, and A. Norman (2007), Isotopic composition of tropospheric and soil N_2O from successive depths of agricultural plots with contrasting crops and nitrogen amendments. J. Geophys. Res., 112, D18303.

Rockmann, T., C. Brenninkmeijer, M. Wollenhaupt, J. Crowley, and P. Crutzen (2000), Measurement of the isotopic fractionation of 15N14N16O, 14N15N16O and 14N14N18O in the UV photolysis of nitrous oxide. Geophys. Res. Lett., 27(9), 1399-1402.

Rockmann, T., J. Kaiser, C. Brenninkmeijer, and W. Brand (2003), Gas chromatography/isotope-ratio mass spectrometry method for high-precision position-dependent 15N and 18O measurements of atmospheric nitrous oxide. Rapid Commun. Mass Spectrom., 17, 1897-1908.

Röckmann, T., & Levin, I. (2005). High-precision determination of the changing isotopic composition of atmospheric N 2 O from 1990 to 2002. Journal of Geophysical Research: Atmospheres, 110(D21).

Rosamond, M., S. Thuss, and S. Schiff (2012), Dependence of riverine nitrous oxide emissions on dissolved oxygen levels. Nature Geoscience, 5, 715-718.

Seitzinger, S., and C. Kroeze (1998), Global distribution of nitrous oxide production and N inputs in freshwater and coastal marine ecosystem. Global Biogeochemical Cycles, 12(1), 93-113.

Stocker, B., R. Roth, F. Joos, R. Spahni, M. Steinacher, S. Zeahle, et. al. (2013), Multiple greenhouse-gas feedbacks from the land biosphere under future climate change scenarios. Nature Climate Change, 3(7), 666-672, doi: 10.1038/nclimate1864

Sowers, T., Rodebaugh, A., Yoshida, N., & Toyoda, S. (2002). Extending records of the isotopic composition of atmospheric N 2 O back to 1800 A.D. from air trapped in snow at the South Pole and the Greenland Ice Sheet Project II ice core. Global Biogeochemical Cycles, 16(4), 76-1-76-10.

Suntharalingam, P., E. Buitenhuis, C. Le Quéré, F. Dentener, C. Nevison, J. H. Butler, H. W. Bange, and G. Forster (2012), Quantifying the Impact of Anthropogenic Nitrogen Deposition on Oceanic Nitrous Oxide. Geophys. Res. Lett., 39(7), doi: 10.1029/2011GL050778

Sutka, R., N. Ostrom, P. Ostrom, H. Gandhi, and J. Breznak (2003), Nitrogen isotopomer site preference of N2O produced by Nitrosomonas europaea and Methylococcus capsulatus Bath. Rapid Commun. in Mass Spectrom., 17(7), 738-745.

Sutka, R., N. Ostrom, P. Ostrom, J. Breznak, H. Gandhi, A. Pitt, and F. Li (2006), Distinguishing nitrous oxide production from nitrification, and denitrification on the basis of isotopomer abundances. Appl. Exp. Microbiol., 72(1), 638-644.

Tilsner, J., N. Wrage, J. Lauf, and G. Gebauer (2003), Emission of gaseous nitrogen oxides from an extensively managed grassland in NE Bavaria, Germany: II. Stable isotope natural abundance of N2O. Biogeochemistry, 63, 249-267.

Toyoda, S., and N. Yoshida (1999), Determination of nitrogen isotopomers of nitrous oxide on a modified isotope ratio mass spectrometer. Anal. Chem., 71(20), 4711-4718.

Toyoda S., N. Yoshida, T. Urabe, Y. Nakayama, T. Suzuki, K. Tsuji, et al. (2004), Temporal and latitudinal distributions of stratospheric N_2O isotopomers. J. Geophys. Res., 109, D08308, doi: 10.1029/2003JD004316

Toyoda, S., H. Mutobe, H. Yamagishi, N. Yoshida, and Y. Tanji (2005), Fractionation of N2O isotopomers during production by denitrifier. Soil Biology and Biochemistry, 37(8), 1535-1545.

Toyoda, S., S. Yamamoto, S. Anai, H. Nara, N. Yoshida, K. Kashiwakura, and K. Akiyama (2008), Isotopomeric characterization of N_2O produced, consumed, and emitted by automobiles. Rapid Commun. Mass Spectrom., 22(5), 603-612.

Toyoda, S., H. Iwai, K. Koba, and N. Yoshida (2009), Isotopomeric analysis of N_2O dissolved in a river in the Tokyo metropolitan area. Rapid Commun. Mass Spectrom. 23(6), 809-821.

Trenberth, K. E. and C. J. Guillemot (1994), The total mass of the atmosphere, J. Geophys. Res., 99, 23079-23088.

Turatti, F., D. Griffiths, S. Wilson, M Esler, T. Rahn, H. Zhang, and G. Blake (2000), Positionally dependent 15N factors in the UV photolysis of N2O determined by high resolution FTIR spectroscopy. Geophys. Res. Lett., 27(16), 2489-2492.

Westley, M., B. Popp, and T. Rust (2007). The calibration of the intramolecular nitrogen isotope distribution in nitrous oxide measured by isotope ratio mass spectrometry. Rapid Communications in Mass Spectrometry, 21(3), 391-405.

Wilson, C., M. Chipperfield, M. Gloor, and F. Chevallier (2014), Development of a variational flux inversion system (INVICAT v1.0) using the TOMCAT chemical transport model. Geoscientific Model Development, 7(5), 2485-2500.

Yamagishi, H., M. Westley, B. Popp, S. Toyoda, N. Yoshida, S. Watanabe, et al. (2007), Role of nitrification and denitrification on the nitrous oxide cycle in the eastern tropical North Pacific and Gulf of California. J. Geophys. Res. – Biogeosci., 112, G02015.

Yoshida, N. and S. Toyoda (2000), Constraining the atmospheric N_2O budget from intramolecular site preference in N_2O isotopomers. Nature, 405, 330–334.

Yung, Y. and C. Miller (1997), Isotopic fractionation of stratospheric nitrous oxide, Science, 278, 1778–1780.

Appendix A

Tables

Table A.1. Linearity corrected, OHSU-PSU air archive N_2O and SF_6 mole fraction measurements. N_2O relative to NOAA-2006A N_2O scale. SF_6 relative to NOAA-2014 SF_6 scale.

Sample	*Collected*	*SF_6 (ppt)*	*SF_6 1σ (ppt)*	*N_2O (ppb)*	*N_2O 1σ (ppb)*
O-031	04/03/78	0.608	0.04	303.26	0.89
O-029	04/04/78	0.752	0.05	303.55	0.66
O-026	04/06/78	0.668	0.06	303.68	0.77
O-017	04/07/78	0.992	0.07	301.93	0.57
O-020	04/07/78	0.623	0.04	340.01	0.99
O-021	10/05/78	0.873	0.05	299.90	0.74
O-022	10/05/78	0.711	0.05	305.07	0.58
O-041	11/03/78	0.918	0.05	611.82	1.14
O-044	11/03/78	0.747	0.04	331.27	0.69
O-045	11/22/78	0.802	0.08	367.39	1.02
O-046	11/22/78	0.655	0.05	298.88	0.81
O-052	12/20/78	0.930	0.06	436.39	0.89
O-084	01/17/80	0.745	0.05	301.69	0.50
O-086	01/21/80	1.008	0.06	302.09	0.84
O-089	02/07/80	0.908	0.04	302.07	0.67
O-090	02/08/80	0.925	0.05	301.41	0.87
O-091	03/25/80	0.873	0.05	303.30	0.61
O-093	04/15/80	0.851	0.06	308.78	0.80
O-096	04/15/80	0.863	0.04	302.77	0.82
O-099	04/18/80	0.868	0.04	302.76	0.73
O-102	04/22/80	0.873	0.05	301.31	0.69
O-087	04/29/80	0.795	0.07	302.22	0.80
O-104	04/29/80	0.903	0.09	301.92	0.62
O-110	06/10/80	0.823	0.03	301.68	0.58
O-114	07/08/80	0.845	0.04	301.44	0.64
O-115	07/17/80	0.844	0.05	300.27	0.58
O-109	10/01/80	0.910	0.06	301.19	0.79
O-124	10/15/80	0.899	0.06	301.93	0.65
O-127	11/12/80	0.989	0.08	301.66	0.62
O-132	12/31/80	0.875	0.08	301.98	0.55
O-133	01/15/81	0.962	0.05	303.45	0.70

O-136	02/25/81	0.913	0.05	302.22	0.45
O-138	03/11/81	1.051	0.03	301.75	0.81
O-140	03/18/81	1.005	0.06	302.75	0.65
O-158	04/17/81	0.943	0.07	301.06	0.72
O-160	04/29/81	1.022	0.06	301.92	0.63
O-163	05/13/81	0.944	0.06	302.33	0.61
O-170	07/15/81	0.974	0.04	304.64	0.78
O-171	07/29/81	0.872	0.07	302.84	0.75
O-174	08/19/81	1.365	0.06	310.40	0.65
O-176	09/02/81	0.668	0.07	301.84	0.55
O-179	09/16/81	1.030	0.05	300.97	0.76
O-183	10/14/81	1.125	0.06	303.53	0.79
O-184	10/14/81	1.178	0.05	303.80	0.52
O-185	10/28/81	0.999	0.04	302.91	0.73
O-190	12/02/81	0.956	0.05	301.75	0.62
O-194	12/30/81	1.066	0.06	303.38	0.89
O-196	01/13/82	1.065	0.02	304.26	0.75
O-199	02/03/82	1.087	0.05	303.64	0.54
O-200	02/03/82	1.117	0.08	303.41	0.68
O-205	03/24/82	1.051	0.05	301.35	0.88
O-206	03/24/82	1.070	0.09	302.41	0.85
O-207	04/07/82	1.056	0.05	303.45	0.69
O-210	04/21/82	1.053	0.06	303.07	0.54
O-215	06/02/82	1.050	0.06	303.80	0.81
O-218	06/30/82	1.109	0.05	304.01	0.76
O-220	07/14/82	1.074	0.06	303.25	0.61
O-222	07/28/82	1.168	0.07	302.25	0.66
O-223	08/11/82	1.069	0.04	303.72	0.72
O-228	09/08/82	1.497	0.08	305.48	0.58
O-235	11/30/82	1.269	0.08	302.44	0.57
O-236	11/30/82	1.018	0.07	299.37	0.84
O-238	12/08/82	1.174	0.06	302.18	0.52
O-239	12/29/82	1.244	0.07	302.35	0.85
O-243	01/31/83	1.139	0.05	303.77	0.76
O-246	02/11/83	1.292	0.08	303.12	0.59
O-249	03/09/83	1.116	0.06	304.19	0.66
O-253	04/06/83	1.222	0.08	303.73	0.88
O-254	04/06/83	1.234	0.04	305.43	0.70
O-256	04/20/83	1.262	0.06	303.93	0.77
O-258	05/24/83	1.153	0.04	303.33	0.56
O-261	06/01/83	1.235	0.08	302.73	0.46
O-262	06/01/83	1.256	0.08	304.26	0.85

O-265	06/29/83	1.226	0.09	301.24	0.44
O-269	08/03/83	1.149	0.06	302.48	0.72
O-270	08/03/83	1.308	0.07	303.67	0.84
O-272	08/31/83	1.186	0.03	303.49	0.93
O-274	09/14/83	1.170	0.06	303.87	0.70
O-277	10/12/83	1.357	0.05	302.26	0.70
O-279	10/26/83	1.285	0.09	302.83	0.80
O-285	12/14/83	1.306	0.06	304.56	0.86
O-286	12/14/83	1.693	0.10	305.06	0.74
O-287	01/25/84	1.108	0.05	303.30	0.73
O-288	01/25/84	1.277	0.09	304.86	0.74
O-289	02/10/84	1.495	0.08	305.09	0.49
O-302	06/27/84	1.367	0.07	304.88	0.73
O-303	07/11/84	1.374	0.03	304.10	0.92
O-308	09/26/84	1.322	0.10	291.69	0.62
O-316	01/17/85	1.467	0.11	305.46	0.67
O-317	01/17/85	1.795	0.08	305.09	0.82
O-323	10/24/85	1.553	0.10	305.84	0.64
O-330	08/04/86	1.613	0.04	304.79	0.48
O-331	10/14/86	1.668	0.03	310.10	0.85
O-332	10/28/86	1.815	0.08	307.09	1.12
O-333	12/04/86	2.143	0.06	310.36	0.72
O-335	01/23/87	2.013	0.07	307.58	0.70
O-338	04/23/87	1.890	0.07	307.69	0.71
O-339	04/23/87	1.800	0.04	307.61	0.39
O-340	04/28/87	1.928	0.06	307.74	0.62
O-341	04/28/87	1.948	0.11	306.60	0.65
O-344	06/16/87	1.927	0.08	306.56	0.82
CORSP 355	09/16/87	2.136	0.10	307.35	0.61
O-361	03/17/88	2.124	0.08	307.54	0.89
O-369	08/29/88	2.125	0.08	308.49	0.69
R-348B	12/28/88	2.462	0.12	307.62	0.56
R-346B	01/17/89	2.222	0.05	309.00	0.58
RSP 371	03/21/89	2.181	0.08	305.07	0.70
RSP 373	03/29/89	2.218	0.08	308.61	0.85
RSP 379	04/11/89	2.166	0.09	309.78	0.75
RSP 380	04/12/89	2.429	0.11	309.05	0.61
RSP 381	04/12/89	2.419	0.07	308.86	0.88
RSP 383	05/03/89	2.193	0.06	310.08	0.55
RSP 384	05/03/89	2.285	0.05	309.73	0.88
RSP 386	06/06/89	2.273	0.08	309.10	0.66
CORSP 387	08/04/89	2.353	0.08	309.08	0.74

CORSP 388	08/25/89	2.376	0.08	308.77	0.41
CORSP 389	09/01/89	2.217	0.07	308.45	0.50
RSP 390	09/14/89	2.496	0.10	313.99	0.94
CORSP 391	09/29/89	2.502	0.15	309.69	0.73
RSP 392	10/06/89	2.261	0.06	308.41	0.79
RSP 393	10/12/89	2.340	0.10	308.70	0.43
CORSP 397	11/10/89	2.360	0.08	310.70	0.61
CORSP 399	11/21/89	2.301	0.12	307.26	0.65
CORSP 402	03/20/90	2.342	0.06	309.85	0.61
CORSP 403	03/27/90	2.531	0.05	310.05	0.67
CORSP 405	04/14/90	2.382	0.08	310.07	0.78
CORSP 406	08/09/90	2.478	0.08	309.63	0.70
CORSP 407	08/15/90	2.461	0.12	309.89	0.87
CORSP 408	09/25/90	2.578	0.05	306.95	0.79
CORSP 409	04/22/91	2.741	0.08	310.31	0.80
CORSP 417	04/02/92	2.811	0.10	311.07	1.01
SPO 298	06/02/92	17.14	0.24	311.11	0.67
CO 420	12/29/92	3.077	0.08	311.48	0.85
CO 426	05/06/93	3.040	0.07	311.79	0.74
CO 427	05/21/93	3.176	0.08	312.45	0.66
CO 428	06/17/93	3.107	0.06	311.80	0.68
CO 433	10/08/93	3.224	0.08	311.66	0.52
CO 434	10/15/93	3.238	0.07	312.36	0.69
CO 435	10/25/93	3.320	0.13	312.17	0.55
CO 438	12/08/93	3.261	0.10	310.11	0.80
CO 442	05/10/94	3.520	0.12	314.79	0.59
CORSP 443	06/22/94	3.421	0.08	311.33	0.61
CORSP 444	07/20/94	3.357	0.09	313.64	0.82
CO 445	08/12/94	3.491	0.08	312.26	0.92
CO 447	11/11/94	4.233	0.08	314.59	0.89
CO 448	11/14/94	3.618	0.12	312.41	0.72
CO 450	03/30/95	3.663	0.11	313.23	0.64
CO 452	06/16/95	3.707	0.11	314.06	0.78
O-027	07/25/95	4.140	0.11	314.61	0.79
CO 453	10/11/95	3.652	0.09	312.77	0.73
CO 454	12/28/95	4.013	0.11	313.32	1.14
CO 455	01/10/96	3.846	0.12	312.85	0.58
CO 456	02/16/96	5.07	0.08	313.31	0.66
CO 457	02/29/96	4.018	0.12	313.49	0.71
CO 459	04/29/96	3.829	0.08	313.41	0.61
CO 460	05/31/96	3.839	0.08	313.98	0.70
CO 462	07/31/96	3.912	0.09	313.76	0.83

CO 463	09/05/96	3.905	0.08	314.16	0.73
O-051	12/17/96	4.036	0.11	334.75	0.90

Table A.2. Raw OHSU-PSU air archive N_2O IRMS measured isotopic compositions. Values are relative to N_2 in air for nitrogen and VSMOW for oxygen with units in per mille (‰).

Sample	*Collected*	δ^{31}	δ^{31} 1σ	δ^{45}	δ^{45} 1σ	δ^{46}	δ^{46} 1σ
O-031	04/03/78	16.10	0.57	8.41	0.06	44.75	0.11
O-029	04/04/78	15.75	0.56	8.62	0.07	44.61	0.25
O-026	04/06/78	15.41	0.36	8.58	0.05	44.49	0.13
O-017	04/07/78	15.97	0.57	8.44	0.07	44.40	0.13
O-020	04/07/78	16.01	0.30	8.94	0.05	45.54	0.11
O-021	10/05/78	15.26	0.30	8.41	0.09	44.50	0.15
O-022	10/05/78	15.85	0.48	8.59	0.07	44.88	0.10
O-041	11/03/78	17.08	0.35	8.91	0.08	52.37	0.17
O-044	11/03/78	15.41	0.31	8.51	0.06	46.75	0.21
O-045	11/22/78	15.03	0.64	7.38	0.06	45.98	0.10
O-046	11/22/78	15.53	0.35	8.30	0.07	44.70	0.10
O-052	12/20/78	15.34	0.48	7.92	0.05	51.39	0.11
O-084	01/17/80	16.26	0.41	8.43	0.11	44.38	0.11
O-086	01/21/80	15.14	0.48	8.30	0.05	44.28	0.12
O-089	02/07/80	15.94	0.30	8.49	0.07	44.42	0.14
O-090	02/08/80	15.41	0.31	8.28	0.05	44.36	0.18
O-091	03/25/80	16.26	0.37	8.29	0.05	44.49	0.18
O-093	04/15/80	15.21	0.31	8.10	0.08	44.15	0.10
O-096	04/15/80	15.63	0.32	8.42	0.11	44.44	0.13
O-099	04/18/80	16.01	0.33	8.30	0.07	44.40	0.10
O-102	04/22/80	16.06	0.58	8.48	0.06	44.45	0.13
O-087	04/29/80	15.43	0.31	8.40	0.06	44.93	0.14
O-104	04/29/80	15.80	0.39	8.45	0.07	44.48	0.10
O-110	06/10/80	15.93	0.44	8.39	0.09	44.48	0.10
O-114	07/08/80	14.73	0.52	8.27	0.07	44.47	0.11
O-115	07/17/80	15.49	0.44	8.33	0.08	44.55	0.10
O-109	10/01/80	15.48	0.38	8.32	0.06	44.39	0.11
O-124	10/15/80	15.21	0.55	8.41	0.08	44.42	0.20
O-127	11/12/80	15.14	0.33	8.31	0.07	44.32	0.11
O-132	12/31/80	15.71	0.38	8.41	0.06	44.44	0.14
O-133	01/15/81	15.24	0.43	8.46	0.05	44.34	0.15
O-136	02/25/81	15.60	0.34	8.42	0.08	44.33	0.21
O-138	03/11/81	15.77	0.36	8.21	0.08	44.39	0.12
O-140	03/18/81	15.10	0.49	8.29	0.07	44.30	0.10
O-158	04/17/81	16.08	0.46	8.31	0.05	44.33	0.10

O-160	04/29/81	15.41	0.33	8.38	0.05	44.34	0.17
O-163	05/13/81	16.29	0.31	8.32	0.12	44.43	0.23
O-170	07/15/81	15.84	0.34	8.36	0.10	44.31	0.12
O-171	07/29/81	15.38	0.53	8.31	0.05	44.76	0.15
O-174	08/19/81	18.18	0.40	9.81	0.07	46.19	0.15
O-176	09/02/81	15.19	0.35	8.34	0.06	44.67	0.30
O-179	09/16/81	16.02	0.30	8.07	0.09	44.24	0.13
O-183	10/14/81	15.50	0.33	8.27	0.09	44.24	0.13
O-184	10/14/81	15.38	0.38	8.13	0.10	44.24	0.10
O-185	10/28/81	15.26	0.36	8.24	0.06	44.28	0.10
O-190	12/02/81	16.40	0.51	8.40	0.06	44.48	0.14
O-194	12/30/81	15.74	0.30	8.30	0.10	44.08	0.16
O-196	01/13/82	15.39	0.52	8.28	0.05	44.53	0.10
O-199	02/03/82	16.31	0.42	8.32	0.05	44.34	0.11
O-200	02/03/82	14.62	0.40	8.20	0.05	44.25	0.15
O-205	03/24/82	15.66	0.39	8.38	0.10	44.45	0.18
O-206	03/24/82	14.70	0.38	8.19	0.05	44.47	0.11
O-207	04/07/82	15.99	0.32	8.14	0.06	44.08	0.23
O-210	04/21/82	15.91	0.34	8.30	0.07	44.45	0.19
O-215	06/02/82	15.75	0.40	8.26	0.05	44.68	0.20
O-218	06/30/82	15.47	0.34	8.27	0.05	44.30	0.17
O-220	07/14/82	15.31	0.35	8.21	0.05	44.21	0.11
O-222	07/28/82	15.46	0.51	8.17	0.10	44.33	0.11
O-223	08/11/82	15.42	0.30	8.46	0.07	44.58	0.18
O-228	09/08/82	15.53	0.38	8.36	0.06	44.54	0.15
O-235	11/30/82	16.48	0.34	8.23	0.08	44.59	0.23
O-236	11/30/82	15.61	0.35	8.26	0.06	44.40	0.13
O-238	12/08/82	15.04	0.50	8.17	0.08	44.34	0.17
O-239	12/29/82	15.46	0.36	8.36	0.05	44.42	0.23
O-243	01/31/83	15.29	0.30	8.36	0.06	44.35	0.13
O-246	02/11/83	15.23	0.37	8.22	0.09	44.15	0.12
O-249	03/09/83	15.54	0.34	8.28	0.05	44.37	0.15
O-253	04/06/83	15.69	0.35	8.34	0.06	44.47	0.36
O-254	04/06/83	16.11	0.41	8.36	0.06	44.30	0.13
O-256	04/20/83	16.03	0.31	8.17	0.07	44.37	0.18
O-258	05/24/83	14.90	0.39	8.26	0.05	44.50	0.25
O-261	06/01/83	15.74	0.34	8.25	0.05	44.12	0.10
O-262	06/01/83	15.71	0.31	8.24	0.05	44.18	0.10
O-265	06/29/83	16.44	0.31	8.33	0.06	44.33	0.21
O-269	08/03/83	15.74	0.43	8.30	0.05	44.34	0.10
O-270	08/03/83	15.60	0.37	8.34	0.07	44.34	0.13
O-272	08/31/83	15.33	0.30	8.28	0.05	44.48	0.14

O-274	09/14/83	16.07	0.43	8.22	0.05	44.58	0.35
O-277	10/12/83	14.77	0.45	8.18	0.12	44.39	0.20
O-279	10/26/83	15.54	0.33	8.29	0.05	44.78	0.19
O-285	12/14/83	15.35	0.32	8.24	0.05	44.47	0.10
O-286	12/14/83	15.46	0.36	8.16	0.05	44.37	0.19
O-287	01/25/84	15.70	0.30	8.30	0.08	44.51	0.25
O-288	01/25/84	15.39	0.31	8.26	0.08	44.16	0.12
O-289	02/10/84	14.92	0.34	8.30	0.07	44.31	0.10
O-302	06/27/84	15.55	0.30	8.25	0.05	44.34	0.10
O-303	07/11/84	15.20	0.34	8.16	0.08	44.24	0.12
O-308	09/26/84	15.29	0.32	8.36	0.05	44.38	0.26
O-316	01/17/85	16.02	0.40	8.35	0.08	44.33	0.10
O-317	01/17/85	15.31	0.31	8.26	0.05	44.25	0.27
O-323	10/24/85	14.90	0.60	8.20	0.05	44.20	0.12
O-330	08/04/86	15.30	0.40	8.18	0.10	44.27	0.11
O-331	10/14/86	15.28	0.48	8.13	0.08	44.91	0.14
O-332	10/28/86	14.94	0.38	8.05	0.06	44.13	0.15
O-333	12/04/86	15.06	0.30	8.21	0.05	44.39	0.17
O-335	01/23/87	14.99	0.30	8.03	0.09	44.33	0.13
O-338	04/23/87	15.50	0.57	8.22	0.07	44.31	0.14
O-339	04/23/87	14.89	0.53	8.11	0.08	44.41	0.11
O-340	04/28/87	14.90	0.46	8.15	0.05	44.18	0.17
O-341	04/28/87	15.64	0.38	8.06	0.05	44.36	0.17
O-344	06/16/87	15.76	0.41	8.05	0.07	44.42	0.16
CORSP 355	09/16/87	14.60	0.52	8.02	0.06	44.17	0.10
O-361	03/17/88	15.37	0.39	7.93	0.07	44.23	0.13
O-369	08/29/88	15.26	0.30	8.14	0.05	44.27	0.11
R-348B	12/28/88	14.89	0.42	8.10	0.06	44.17	0.10
R-346B	01/17/89	14.93	0.34	7.97	0.06	44.32	0.20
RSP 371	03/21/89	15.50	0.55	7.97	0.05	44.16	0.11
RSP 373	03/29/89	15.44	0.45	7.97	0.08	44.38	0.24
RSP 379	04/11/89	15.05	0.54	7.97	0.06	44.08	0.10
RSP 380	04/12/89	15.24	0.45	7.93	0.05	44.16	0.11
RSP 381	04/12/89	15.33	0.40	8.10	0.08	44.24	0.21
RSP 383	05/03/89	14.66	0.32	7.99	0.13	44.24	0.18
RSP 384	05/03/89	15.27	0.39	7.87	0.07	44.20	0.18
RSP 386	06/06/89	15.02	0.35	8.02	0.07	44.13	0.15
CORSP 387	08/04/89	15.34	0.30	8.07	0.08	44.29	0.10
CORSP 388	08/25/89	14.31	0.43	7.98	0.09	44.19	0.10
CORSP 389	09/01/89	15.49	0.46	7.89	0.05	44.33	0.16
RSP 390	09/14/89	14.97	0.31	7.85	0.09	44.39	0.11
CORSP 391	09/29/89	14.84	0.35	7.86	0.09	44.43	0.17

RSP 392	10/06/89	14.53	0.37	7.97	0.08	43.98	0.12
RSP 393	10/12/89	14.41	0.33	8.01	0.08	44.15	0.12
CORSP 397	11/10/89	15.28	0.55	8.13	0.08	44.42	0.23
CORSP 399	11/21/89	14.90	0.41	7.93	0.06	44.16	0.13
CORSP 402	03/20/90	14.78	0.36	7.97	0.06	44.35	0.20
CORSP 403	03/27/90	14.48	0.42	8.06	0.06	44.24	0.19
CORSP 405	04/14/90	15.38	0.45	7.86	0.05	44.33	0.15
CORSP 406	08/09/90	14.57	0.45	7.97	0.06	44.24	0.16
CORSP 407	08/15/90	14.99	0.63	7.99	0.09	44.28	0.15
CORSP 408	09/25/90	15.17	0.30	7.98	0.11	44.28	0.11
CORSP 409	04/22/91	14.52	0.40	7.93	0.08	44.07	0.10
CORSP 417	04/02/92	15.12	0.58	7.86	0.07	44.17	0.10
SPO 298	06/02/92	14.78	0.56	7.87	0.05	44.05	0.11
CO 420	12/29/92	15.56	0.30	7.88	0.05	44.08	0.24
CO 426	05/06/93	14.98	0.39	7.97	0.08	44.05	0.10
CO 427	05/21/93	15.28	0.30	7.79	0.05	44.12	0.24
CO 428	06/17/93	14.87	0.41	7.84	0.09	44.15	0.15
CO 433	10/08/93	15.15	0.33	7.99	0.06	44.25	0.12
CO 434	10/15/93	14.67	0.56	7.86	0.09	44.13	0.16
CO 435	10/25/93	15.05	0.39	7.88	0.06	44.11	0.10
CO 438	12/08/93	14.56	0.32	7.84	0.09	44.22	0.11
CO 442	05/10/94	15.19	0.32	8.05	0.09	44.59	0.13
CORSP 443	06/22/94	15.17	0.43	7.82	0.08	44.05	0.13
CORSP 444	07/20/94	14.63	0.36	7.75	0.05	44.13	0.17
CO 445	08/12/94	14.78	0.56	7.95	0.06	44.35	0.11
CO 447	11/11/94	14.37	0.54	7.81	0.05	44.27	0.19
CO 448	11/14/94	14.40	0.38	7.70	0.06	44.19	0.10
CO 450	03/30/95	15.16	0.57	7.76	0.06	44.15	0.23
CO 452	06/16/95	14.65	0.30	7.74	0.05	44.12	0.24
O-027	07/25/95	14.56	0.51	7.74	0.11	44.14	0.19
CO 453	10/11/95	14.79	0.49	7.89	0.06	43.97	0.10
CO 454	12/28/95	14.43	0.30	7.66	0.07	44.13	0.16
CO 455	01/10/96	14.97	0.69	7.85	0.07	44.10	0.29
CO 456	02/16/96	14.86	0.33	7.69	0.10	44.19	0.10
CO 457	02/29/96	15.00	0.31	7.80	0.10	44.07	0.17
CO 459	04/29/96	14.83	0.31	7.79	0.08	44.20	0.13
CO 460	05/31/96	14.47	0.41	7.72	0.09	44.31	0.17
CO 462	07/31/96	14.02	0.56	7.73	0.10	44.10	0.10
CO 463	09/05/96	14.93	0.55	7.68	0.06	44.11	0.12
O-051	12/17/96	14.67	0.74	7.73	0.13	46.39	0.11

Table A.3. OHSU-PSU air archive isotopic N_2O composition after numerically solving for intramolecular composition. Nitrogen values ($\delta^{15}N$, $\delta^{15}N^{\alpha}$, and $\delta^{15}N^{\beta}$) are relative to N_2 in air, $\delta^{18}O$ is relative to VSMOW. Units are in per mille (‰).

Sample	*Collected*	$\delta^{15}N$	$\delta^{15}N$ 1σ	$\delta^{15}N^{\alpha}$	$\delta^{15}N^{\alpha}$ 1σ	$\delta^{15}N^{\beta}$	$\delta^{15}N^{\beta}$ 1σ	$\delta^{18}O$	$\delta^{18}O$ 1σ
O-031	04/03/78	7.66	0.06	17.57	0.76	-2.25	0.77	44.96	0.11
O-029	04/04/78	7.84	0.05	16.57	0.53	-0.88	0.53	44.70	0.13
O-026	04/06/78	7.88	0.07	17.02	0.79	-1.26	0.80	44.82	0.25
O-017	04/07/78	7.70	0.07	17.40	0.79	-2.00	0.80	44.62	0.13
O-020	04/07/78	8.20	0.05	17.26	0.42	-0.86	0.43	45.76	0.11
O-021	10/05/78	7.67	0.09	16.39	0.45	-1.05	0.50	44.72	0.15
O-022	10/05/78	7.85	0.07	17.17	0.66	-1.47	0.69	45.09	0.10
O-041	11/03/78	7.98	0.08	18.34	0.51	-2.38	0.55	52.65	0.17
O-044	11/03/78	7.71	0.06	16.45	0.45	-1.02	0.47	46.97	0.21
O-045	11/22/78	6.54	0.06	16.29	0.88	-3.21	0.89	46.23	0.10
O-046	11/22/78	7.54	0.07	16.79	0.50	-1.71	0.54	44.93	0.10
O-052	12/20/78	6.97	0.05	16.23	0.68	-2.30	0.68	51.67	0.11
O-084	01/17/80	7.69	0.11	17.78	0.60	-2.40	0.65	44.59	0.11
O-086	01/21/80	7.56	0.05	16.27	0.68	-1.15	0.69	44.49	0.12
O-089	02/07/80	7.75	0.07	17.33	0.43	-1.84	0.47	44.64	0.14
O-090	02/08/80	7.53	0.05	16.64	0.44	-1.58	0.45	44.59	0.19
O-091	03/25/80	7.54	0.05	17.87	0.53	-2.79	0.54	44.70	0.18
O-093	04/15/80	7.35	0.08	16.45	0.47	-1.74	0.51	44.37	0.10
O-096	04/15/80	7.67	0.11	16.92	0.46	-1.57	0.54	44.65	0.13
O-099	04/18/80	7.55	0.08	17.49	0.48	-2.39	0.50	44.61	0.10
O-102	04/22/80	7.74	0.06	17.53	0.82	-2.05	0.83	44.67	0.13
O-087	04/29/80	7.64	0.06	16.61	0.43	-1.33	0.45	45.15	0.15
O-104	04/29/80	7.71	0.07	17.16	0.57	-1.74	0.60	44.70	0.10
O-110	06/10/80	7.64	0.09	17.36	0.62	-2.08	0.65	44.69	0.10
O-114	07/08/80	7.52	0.07	15.69	0.73	-0.65	0.75	44.69	0.11
O-115	07/17/80	7.58	0.08	16.75	0.63	-1.60	0.66	44.77	0.11
O-109	10/01/80	7.57	0.06	16.76	0.55	-1.62	0.57	44.61	0.11
O-124	10/15/80	7.67	0.08	16.34	0.78	-1.01	0.80	44.64	0.19
O-127	11/12/80	7.56	0.08	16.27	0.46	-1.15	0.49	44.53	0.12
O-132	12/31/80	7.67	0.06	17.07	0.52	-1.74	0.54	44.66	0.14
O-133	01/15/81	7.72	0.05	16.39	0.60	-0.94	0.61	44.55	0.15
O-136	02/25/81	7.68	0.09	16.90	0.50	-1.54	0.55	44.54	0.21
O-138	03/11/81	7.46	0.08	17.19	0.51	-2.27	0.55	44.61	0.12
O-140	03/18/81	7.54	0.07	16.21	0.71	-1.12	0.73	44.52	0.10
O-158	04/17/81	7.57	0.05	17.58	0.65	-2.45	0.66	44.55	0.10

O-160	04/29/81	7.64	0.05	16.60	0.49	-1.33	0.50	44.56	0.17
O-163	05/13/81	7.57	0.13	17.88	0.45	-2.74	0.54	44.64	0.23
O-170	07/15/81	7.62	0.11	17.25	0.49	-2.02	0.55	44.53	0.12
O-171	07/29/81	7.55	0.05	16.56	0.77	-1.45	0.77	44.98	0.15
O-174	08/19/81	9.10	0.07	19.99	0.57	-1.79	0.58	46.39	0.16
O-176	09/02/81	7.59	0.06	16.32	0.51	-1.15	0.52	44.88	0.31
O-179	09/16/81	7.31	0.09	17.58	0.42	-2.95	0.48	44.47	0.13
O-183	10/14/81	7.52	0.10	16.80	0.47	-1.76	0.52	44.46	0.13
O-184	10/14/81	7.38	0.11	16.68	0.52	-1.92	0.57	44.46	0.10
O-185	10/28/81	7.49	0.06	16.46	0.52	-1.48	0.55	44.50	0.10
O-190	12/02/81	7.66	0.06	17.99	0.72	-2.68	0.74	44.69	0.14
O-194	12/30/81	7.56	0.11	17.13	0.42	-2.02	0.49	44.29	0.16
O-196	01/13/82	7.53	0.05	16.64	0.75	-1.59	0.76	44.75	0.10
O-199	02/03/82	7.57	0.05	17.92	0.59	-2.78	0.60	44.56	0.11
O-200	02/03/82	7.45	0.05	15.56	0.55	-0.66	0.57	44.47	0.15
O-205	03/24/82	7.63	0.10	16.95	0.56	-1.69	0.61	44.66	0.18
O-206	03/24/82	7.43	0.05	15.62	0.52	-0.76	0.54	44.69	0.11
O-207	04/07/82	7.39	0.06	17.52	0.45	-2.74	0.47	44.28	0.23
O-210	04/21/82	7.55	0.07	17.34	0.49	-2.23	0.51	44.67	0.19
O-215	06/02/82	7.50	0.05	17.12	0.57	-2.12	0.59	44.90	0.21
O-218	06/30/82	7.52	0.05	16.75	0.48	-1.71	0.49	44.51	0.17
O-220	07/14/82	7.46	0.05	16.49	0.49	-1.57	0.50	44.43	0.11
O-222	07/28/82	7.41	0.10	16.76	0.73	-1.93	0.78	44.55	0.11
O-223	08/11/82	7.72	0.07	16.61	0.42	-1.18	0.45	44.79	0.18
O-228	09/08/82	7.61	0.06	16.80	0.54	-1.58	0.56	44.75	0.16
O-235	11/30/82	7.47	0.08	18.18	0.49	-3.23	0.53	44.81	0.24
O-236	11/30/82	7.51	0.06	16.93	0.49	-1.92	0.50	44.62	0.13
O-238	12/08/82	7.41	0.09	16.17	0.74	-1.34	0.76	44.55	0.17
O-239	12/29/82	7.61	0.05	16.71	0.52	-1.48	0.54	44.64	0.23
O-243	01/31/83	7.62	0.06	16.46	0.42	-1.23	0.44	44.56	0.13
O-246	02/11/83	7.47	0.10	16.44	0.51	-1.50	0.56	44.38	0.12
O-249	03/09/83	7.53	0.05	16.84	0.48	-1.78	0.50	44.59	0.15
O-253	04/06/83	7.59	0.07	17.04	0.50	-1.85	0.51	44.68	0.35
O-254	04/06/83	7.61	0.06	17.63	0.60	-2.40	0.62	44.52	0.13
O-256	04/20/83	7.41	0.07	17.56	0.43	-2.73	0.45	44.59	0.18
O-258	05/24/83	7.51	0.05	15.93	0.55	-0.92	0.55	44.74	0.25
O-261	06/01/83	7.51	0.05	17.16	0.50	-2.15	0.51	44.33	0.10
O-262	06/01/83	7.50	0.05	17.10	0.45	-2.11	0.46	44.40	0.10
O-265	06/29/83	7.59	0.07	18.10	0.43	-2.93	0.46	44.55	0.21
O-269	08/03/83	7.55	0.05	17.12	0.60	-2.01	0.62	44.55	0.10
O-270	08/03/83	7.59	0.07	16.91	0.53	-1.73	0.56	44.55	0.13
O-272	08/31/83	7.53	0.05	16.51	0.43	-1.45	0.45	44.70	0.14

O-274	09/14/83	7.46	0.05	17.59	0.60	-2.66	0.61	44.80	0.37
O-277	10/12/83	7.42	0.13	15.78	0.65	-0.93	0.71	44.61	0.20
O-279	10/26/83	7.53	0.05	16.81	0.49	-1.74	0.51	45.01	0.19
O-285	12/14/83	7.49	0.05	16.56	0.46	-1.58	0.48	44.69	0.10
O-286	12/14/83	7.41	0.05	16.75	0.50	-1.94	0.52	44.58	0.19
O-287	01/25/84	7.55	0.09	17.05	0.42	-1.96	0.46	44.74	0.25
O-288	01/25/84	7.52	0.08	16.62	0.44	-1.59	0.47	44.37	0.12
O-289	02/10/84	7.56	0.07	15.94	0.48	-0.83	0.51	44.52	0.10
O-302	06/27/84	7.50	0.05	16.85	0.43	-1.85	0.45	44.56	0.10
O-303	07/11/84	7.41	0.08	16.38	0.48	-1.56	0.51	44.45	0.12
O-308	09/26/84	7.62	0.05	16.48	0.45	-1.24	0.47	44.60	0.26
O-316	01/17/85	7.61	0.08	17.47	0.57	-2.26	0.60	44.54	0.10
O-317	01/17/85	7.51	0.05	16.54	0.44	-1.52	0.45	44.47	0.27
O-323	10/24/85	7.45	0.05	15.93	0.85	-1.03	0.86	44.42	0.13
O-330	08/04/86	7.43	0.11	16.53	0.55	-1.68	0.60	44.49	0.11
O-331	10/14/86	7.36	0.08	16.49	0.69	-1.76	0.72	45.14	0.14
O-332	10/28/86	7.30	0.06	16.08	0.53	-1.49	0.54	44.35	0.15
O-333	12/04/86	7.46	0.05	16.16	0.41	-1.24	0.43	44.61	0.18
O-335	01/23/87	7.27	0.09	16.13	0.41	-1.60	0.46	44.55	0.14
O-338	04/23/87	7.47	0.07	16.78	0.77	-1.84	0.79	44.53	0.14
O-339	04/23/87	7.35	0.08	15.95	0.75	-1.25	0.77	44.63	0.11
O-340	04/28/87	7.40	0.05	15.98	0.67	-1.18	0.68	44.40	0.17
O-341	04/28/87	7.30	0.05	17.03	0.53	-2.44	0.55	44.59	0.17
O-344	06/16/87	7.29	0.07	17.21	0.57	-2.63	0.59	44.64	0.16
CORSP 355	09/16/87	7.26	0.06	15.62	0.74	-1.09	0.76	44.39	0.10
O-361	03/17/88	7.17	0.08	16.72	0.56	-2.39	0.58	44.45	0.13
O-369	08/29/88	7.39	0.05	16.50	0.44	-1.72	0.45	44.49	0.11
R-348B	12/28/88	7.35	0.06	15.98	0.57	-1.28	0.59	44.39	0.11
R-346B	01/17/89	7.21	0.06	16.07	0.49	-1.66	0.50	44.53	0.19
RSP 371	03/21/89	7.21	0.05	16.89	0.77	-2.46	0.78	44.38	0.11
RSP 373	03/29/89	7.21	0.09	16.82	0.64	-2.40	0.68	44.59	0.25
RSP 379	04/11/89	7.21	0.06	16.30	0.75	-1.87	0.77	44.29	0.10
RSP 380	04/12/89	7.17	0.05	16.52	0.64	-2.18	0.65	44.38	0.11
RSP 381	04/12/89	7.35	0.08	16.59	0.55	-1.90	0.59	44.46	0.21
RSP 383	05/03/89	7.23	0.13	15.68	0.47	-1.22	0.56	44.46	0.18
RSP 384	05/03/89	7.11	0.07	16.61	0.54	-2.40	0.57	44.41	0.18
RSP 386	06/06/89	7.26	0.07	16.20	0.48	-1.68	0.51	44.35	0.15
CORSP 387	08/04/89	7.31	0.08	16.62	0.42	-2.00	0.46	44.51	0.10
CORSP 388	08/25/89	7.22	0.09	15.19	0.61	-0.74	0.65	44.41	0.10
CORSP 389	09/01/89	7.12	0.05	16.89	0.65	-2.65	0.66	44.55	0.16
RSP 390	09/14/89	7.08	0.09	16.18	0.44	-2.02	0.49	44.61	0.11
CORSP 391	09/29/89	7.09	0.09	15.98	0.48	-1.81	0.52	44.65	0.17

RSP 392	10/06/89	7.22	0.08	15.50	0.52	-1.06	0.56	44.20	0.12
RSP 393	10/12/89	7.25	0.09	15.34	0.46	-0.84	0.50	44.36	0.12
CORSP 397	11/10/89	7.37	0.08	16.52	0.77	-1.77	0.80	44.63	0.24
CORSP 399	11/21/89	7.17	0.06	16.04	0.59	-1.70	0.60	44.38	0.13
CORSP 402	03/20/90	7.21	0.06	15.85	0.52	-1.44	0.53	44.57	0.21
CORSP 403	03/27/90	7.31	0.06	15.40	0.56	-0.79	0.58	44.46	0.20
CORSP 405	04/14/90	7.09	0.05	16.74	0.64	-2.56	0.65	44.56	0.15
CORSP 406	08/09/90	7.21	0.06	15.58	0.64	-1.16	0.66	44.45	0.16
CORSP 407	08/15/90	7.23	0.09	16.15	0.89	-1.68	0.92	44.51	0.15
CORSP 408	09/25/90	7.22	0.12	16.41	0.43	-1.97	0.51	44.50	0.11
CORSP 409	04/22/91	7.17	0.09	15.52	0.58	-1.18	0.60	44.29	0.10
CORSP 417	04/02/92	7.10	0.07	16.38	0.84	-2.18	0.86	44.39	0.10
SPO 298	06/02/92	7.11	0.05	15.93	0.80	-1.71	0.81	44.27	0.11
CO 420	12/29/92	7.12	0.05	16.98	0.43	-2.75	0.45	44.31	0.23
CO 426	05/06/93	7.21	0.08	16.14	0.54	-1.71	0.58	44.27	0.10
CO 427	05/21/93	7.02	0.05	16.64	0.42	-2.59	0.44	44.34	0.24
CO 428	06/17/93	7.07	0.09	16.02	0.57	-1.88	0.60	44.38	0.15
CO 433	10/08/93	7.23	0.06	16.37	0.47	-1.92	0.49	44.47	0.12
CO 434	10/15/93	7.10	0.09	15.72	0.77	-1.53	0.80	44.35	0.16
CO 435	10/25/93	7.12	0.06	16.30	0.56	-2.06	0.58	44.33	0.10
CO 438	12/08/93	7.07	0.09	15.58	0.47	-1.44	0.52	44.44	0.12
CO 442	05/10/94	7.28	0.09	16.41	0.45	-1.84	0.50	44.82	0.14
CORSP 443	06/22/94	7.06	0.09	16.49	0.61	-2.37	0.65	44.27	0.13
CORSP 444	07/20/94	6.98	0.05	15.72	0.52	-1.76	0.53	44.36	0.18
CO 445	08/12/94	7.19	0.06	15.90	0.81	-1.52	0.83	44.57	0.11
CO 447	11/11/94	7.04	0.05	15.31	0.78	-1.23	0.80	44.50	0.20
CO 448	11/14/94	6.92	0.06	15.43	0.55	-1.58	0.57	44.42	0.10
CO 450	03/30/95	6.99	0.06	16.48	0.82	-2.50	0.84	44.36	0.24
CO 452	06/16/95	6.97	0.05	15.72	0.42	-1.78	0.43	44.35	0.23
O-027	07/25/95	6.97	0.12	15.65	0.75	-1.70	0.79	44.36	0.19
CO 453	10/11/95	7.13	0.06	15.91	0.70	-1.64	0.72	44.20	0.10
CO 454	12/28/95	6.89	0.07	15.48	0.43	-1.71	0.45	44.36	0.16
CO 455	01/10/96	7.09	0.08	16.19	0.99	-2.02	1.00	44.33	0.29
CO 456	02/16/96	6.91	0.11	16.06	0.47	-2.24	0.53	44.42	0.10
CO 457	02/29/96	7.03	0.10	16.23	0.43	-2.17	0.49	44.29	0.17
CO 459	04/29/96	7.02	0.09	16.00	0.41	-1.97	0.46	44.42	0.13
CO 460	05/31/96	6.94	0.09	15.50	0.59	-1.62	0.62	44.53	0.17
CO 462	07/31/96	6.96	0.11	14.82	0.78	-0.90	0.80	44.32	0.10
CO 463	09/05/96	6.91	0.07	16.17	0.76	-2.35	0.78	44.33	0.12
O-051	12/17/96	6.89	0.14	15.69	1.04	-1.91	1.09	46.63	0.11

Table A.4. Total annual N_2O anthropogenic source in TgN yr^{-1} between 1978 and 1996 for EDGAR v4.3.2 and the results of the 2-box model.

Year	EDGAR v4.3.2	2-Box Model
1978	6.63	3.81
1979	6.8	3.88
1980	6.81	3.96
1981	6.81	4.03
1982	6.75	4.10
1983	6.88	4.18
1984	7.06	4.26
1985	7.04	4.34
1986	7.09	4.42
1987	7.19	4.50
1988	7.26	4.58
1989	7.35	4.66
1990	7.21	4.75
1991	7.17	4.84
1992	7.22	4.93
1993	7.19	5.02
1994	7.33	5.11
1995	7.56	5.21
1996	7.71	5.30

Appendix B

Matlab Scripts

B.1. Sub-routine to solve for N_2O isotopic composition from measured isotope ratios.

```
% Initial processing script for n2o isotopic results
%

%
% We are beginning with the values in iVals brought in from Excel
% iVals columns are:
% Col 1 = ddate,    Col 2 = fdate,      Col 3 = N2O mole fraction (ppb)
% Col 4 = N2O +/-   Col 5 = d31,        Col 6 = d31 1sig,
% Col 7 = d45,      Col 8 = d45 1sig,   Col 9 = d46,
% Col 10 = d46 1sig
%

%
% First step is to transform d values into R values
%
% The equation for d:
% d = [(R_sample / R_std) -1] * 1000
%
% So, solving for R_sample:
% R_sample = [(d/1000)+1] * R_std

% R_std values are derived from the exact known R values in the 15N Air
% and 17O and 18O VSMOW standards
% R31_std = R15 + R17
% R45_std = 2(R15) + R 17
% R46_std = R18 + 2*(R17+R15) + (R15)^2
% where R15 = 0.0036765, R17 = 0.0003799, R18 = 0.0020052

% We define R_std as:
R15_std = 0.0036765;
R17_std = 0.0003799;
R18_std = 0.0020052;
R31_std = 0.00405640;
R45_std = 0.00773290;
R46_std = 0.00202151;

% Now define arrays for the values to go into

D_31 = zeros(length(iVals(:,1)),1);
D_45 = zeros(length(iVals(:,1)),1);
D_46 = zeros(length(iVals(:,1)),1);

% Loop to solve for R values (Col 1) along with 1-sigma in R (Col 2)
for i = 1:length(iVals(:,1))
   D_31(i,1) = ((iVals(i,5)/1000)+1)*R31_std;
   D_31(i,2) = ((((iVals(i,5)+iVals(i,6))/1000)+1)*R31_std)-D_31(i,1);
```

```
   D_45(i,1) = ((iVals(i,7)/1000)+1)*R45_std;
   D_45(i,2) = ((((iVals(i,7)+iVals(i,8))/1000)+1)*R45_std)-D_45(i,1);

   D_46(i,1) = ((iVals(i,9)/1000)+1)*R46_std;
   D_46(i,2) = ((((iVals(i,9)+iVals(i,10))/1000)+1)*R46_std)-D_46(i,1);
end

% From here, we need to calculate 1000 values for each data
% point, using Col 1 as the mean and Col 2 as the stdev

r1 = zeros(length(iVals(:,1)),1000);
r2 = zeros(length(iVals(:,1)),1000);
r3 = zeros(length(iVals(:,1)),1000);

for i = 1:length(iVals(:,1))
   r1(i,:) = normrnd(D_45(i,1),D_45(i,2),[1,1000]); %45R
   r2(i,:) = normrnd(D_46(i,1),D_46(i,2),[1,1000]); %46R
   r3(i,:) = normrnd(D_31(i,1),D_31(i,2),[1,1000]); %31R
end

%
% Define initial guess points for the variable fsolve is to solve for
% x0 = [15Ra; 15Rb; 17R; 18R];
%

x0 = [0.0037416; 0.0036661; 0.0003868; 0.0020762];

%
% Create vectors for solved values to be placed in
%

R15a = zeros(length(iVals),1000);
R15b = zeros(length(iVals),1000);
R17 = zeros(length(iVals),1000);
R18 = zeros(length(iVals),1000);

%
% Loop that will solve the equations for R15a, R15b, R17, and R18
%

for j = 1:length(iVals(:,1))
   for i = 1:1000 % solve equations 1000 times

      x = fsolve(@(x)root4d(x,r1(j,i),r2(j,i),r3(j,i)),x0); % Call fsolve

      R15a(j,i) = x(1); % Places solved values in their correct vector
      R15b(j,i) = x(2); % without overwriting previous solution
      R17(j,i) = x(3);
      R18(j,i) = x(4);
   end
end
%%

%
% From here, we need to find the mean and stdev of each row for each
```

```
% variable, then convert to d values
%

d15Na = zeros(length(iVals(:,1)),2);
d15Nb = zeros(length(iVals(:,1)),2);
d17O = zeros(length(iVals(:,1)),2);
d18O = zeros(length(iVals(:,1)),2);

for i = 1:length(iVals(:,1))
   x(1,1) = mean(R15a(i,:));
   x(1,2) = std(R15a(i,:));
   d15Na(i,1) = ((x(1,1)/R15_std)-1)*1000;
   d15Na(i,2) = ((((x(1,1)+x(1,2))/R15_std)-1)*1000)-d15Na(i,1);

   x(1,1) = mean(R15b(i,:));
   x(1,2) = std(R15b(i,:));
   d15Nb(i,1) = ((x(1,1)/R15_std)-1)*1000;
   d15Nb(i,2) = ((((x(1,1)+x(1,2))/R15_std)-1)*1000)-d15Nb(i,1);

   x(1,1) = mean(R17(i,:));
   x(1,2) = std(R17(i,:));
   d17O(i,1) = ((x(1,1)/R17_std)-1)*1000;
   d17O(i,2) = ((((x(1,1)+x(1,2))/R17_std)-1)*1000)-d17O(i,1);

   x(1,1) = mean(R18(i,:));
   x(1,2) = std(R18(i,:));
   d18O(i,1) = ((x(1,1)/R18_std)-1)*1000;
   d18O(i,2) = ((((x(1,1)+x(1,2))/R18_std)-1)*1000)-d18O(i,1);
end

%%

% Now we need to find 15R-bulk

% Define initial guess points for the variable fsolve is to solve for
% x0 = [R15-bulk; R17; R18];


x0 = [0.0037022; 0.0003868; 0.0020762];

%
% Create vectors for solved values to be placed in
%

R15_bulk = zeros(length(iVals),1000);

%
% Loop that will solve the equations for 15R-bulk, R17, and R18
%

for j = 1:length(iVals(:,1))
   for i = 1:1000 % solve equations 1000 times

      x = fsolve(@(x)root3d(x,r1(j,i),r2(j,i)),x0); % Call fsolve
```

```
        R15_bulk(j,i) = x(1);

    end
end

%%

d15N_bulk = zeros(length(iVals(:,1)),2);
y = zeros(1,1000);

for i = 1:length(iVals(:,1))
    x(1,1) = mean(R15_bulk(i,:));
    x(1,2) = std(R15_bulk(i,:));
    d15N_bulk(i,1) = ((x(1,1)/R15_std)-1)*1000;
    d15N_bulk(i,2) = ((((x(1,1)+x(1,2))/R15_std)-1)*1000)-d15N_bulk(i,1);
end

% Now, we create an array for all of our important values to go in

fVals(:,1) = iVals(:,1);
fVals(:,2) = iVals(:,2);
fVals(:,3) = iVals(:,3);
fVals(:,4) = iVals(:,4);
fVals(:,5) = d15N_bulk(:,1);
fVals(:,6) = d15N_bulk(:,2);
fVals(:,7) = d15Na(:,1);
fVals(:,8) = d15Na(:,2);
fVals(:,9) = d15Nb(:,1);
fVals(:,10) = d15Nb(:,2);
fVals(:,11) = d17O(:,1);
fVals(:,12) = d17O(:,2);
fVals(:,13) = d18O(:,1);
fVals(:,14) = d18O(:,2);
fVals(:,15) = iVals(:,5);
fVals(:,16) = iVals(:,6);
fVals(:,17) = iVals(:,7);
fVals(:,18) = iVals(:,8);
fVals(:,19) = iVals(:,9);
fVals(:,20) = iVals(:,10);
```

B.2. 2-box model for N_2O concentration.

```
% Start by defining the change in concentration in time within each box
%
% d/dt C_T = S_T + F_S-T - F_T-S    Troposphere
% d/dt C_S = F_T-S - F_S-T - L      Stratosphere
%
% C is the concentration in each box defined by
% C = [N2O]
% Let X_S and X_T represent the ratio of the mass within each box
% Using Kaiser 2002, and Rockmann 2003, we can say
% X_S = 0.15 and X_T = 0.85
%
% F represents the flux of air between the boxes
% F_S-T = flux FROM the Strat TO the Trop
% F_T-S = flux FROM the Trop TO the Strat
%
% Assume that the Total Flux in Tg/yr is the same in both directions
% Fx = 1.4 to 2.8 * 10^8 Tg/yr      % Warneck, 1988 and Holton, 1995
% F_S-T = Fx*[N2O]_S
% F_T-S = Fx*[N2O]_T
%
% L = total sink, which we define as:
% L = (M_T*[N2O]_T + M_S*[N2O]_S) / tau
% where tau = lifetime
%
% Troposphere equation is:
% d/dt M_T*[N2O]_T = S_T + Fx*[N2O]_S - Fx*[N2O]_T
%
% Stratosphere equation is:
% d/dt M_S*[N2O]_S = Fx*[N2O]_T - Fx*[N2O]_S - ...
%   (M_T*[N2O]_T + M_S*[N2O]_S)/tau

% Define the constants and variables
M = 1.77*10^8;  % Total mol of the atmosphere (Tmol)
X_S = 0.15;     % Fraction of mass in Stratosphere (Rockmann et al. 2003)
X_T = 0.85;     % Fraction of mass in Troposphere
M_S = M*X_S;    % Mass in Stratosphere (Tmol)
M_T = M*X_T;    % Mass in Troposphere (Tmol)
Fx = 6937920;       % Avg-Estimate of Trop-Strat Flux (Tmol/yr)
tau = 120;      % Lifetime of N2O (yr)

% We need to have initial conditions, then perturb the system from there
% We do not have [N2O]_S values, so we will need to initially solve for it
% Define what the Steady-State concentration is and the supposed S_nat

% pre-industrial sources

% S_oce in TgN/yr
S_oce = 4.2;
S_oce = S_oce/28;    % convert TgN to Tmol

% S_terr in TgN/yr
S_terr = 6.6;
```

```
S_terr = S_terr/28;  % convert TgN to Tmol

% name a1 and a2 the ocean and terr source
a1 = S_oce;
a2 = S_terr;

% set the dates to solve between
tspan = (0:10:3000);

% set the initial concentrations
x0 = [0 0];

% exponential parameters
b = 0.0202;
s = 0;

% solve system using ode23s
[t,x] = ode23s(@(t,x) Box_Model_Eq1_Revised(t,x,Fx,M_T,M_S,a1,a2,s,b,tau),tspan,x0);

% plot figure
figure
plot(t(:,1),x(:,1),'k-');

% take the last values in x as pre-industrial natural concentrations
N2O_Ti = x(end,1);
N2O_Si = x(end,2);
%%
% using these values, solve Box_Model_Eq2

% set the dates to solve between 0 and 150 (really 1750 to 2000)
tspan = (0:1:250);

% set the initial concentrations
x0 = [N2O_Ti N2O_Si];

% exponential parameters
% These are mannually adjusted for the moment, should try to find a better
% way to define these values in the future
b = 0.0183;          % High = 0.0185, Mid = 0.0183, Low = 0.0186
s = 0.0021;          % High = 0.0020, Mid = 0.0021, Low = 0.0020

% solve system using ode23s
[t,x] = ode23s(@(t,x) Box_Model_Eq2_Revised(t,x,Fx,M_T,M_S,a1,a2,s,b,tau),tspan,x0);

% Create an array for year between 1750 and 2000 counting by 1
time = 1750:1:2000;
time = time';

% Create an array for the concentration between 1750 and 2000
concentration = zeros(251,2);
for i = 1:1
   concentration(i,1) = N2O_Ti;
   concentration(i,2) = N2O_Si;
end
for i = 1:250
```

```
    concentration(i+1,1) = x(i,1);
    concentration(i+1,2) = x(i,2);
end

% plot figure
figure
plot(time(:,1),concentration(:,1),'k-');
hold on

% include AR5 longterm N2O and CM measured values on plot
% Note: these need to be loaded in from excel
% AR5 = [];
% CM_N2O = [];
% CM_d15N = [];
% CM_d15Na = [];
% CM_d15Nb = [];
% CM_d18O = [];

% figure
plot(AR5(:,1),AR5(:,2),'bx');
% figure
% hold on
plot(CM_N2O(:,1),CM_N2O(:,2),'c+');
```

B.3. 2-box model, equation 1, for N_2O concentration.

```
% Start with our 2-Equations
% x(1) = [N2O]_T or troposphere N2O concentration
% x(2) = [N2O]_S or stratosphere N2O concentration
% X_T = Ratio of air in troposphere over total(Tg)
% X_S = Ratio of air in stratosphere over total (Tg)
% a1 = natural ocean sources
% a2 = natural terrestrial sources
% b = anthropogenic growth rate constant
% Fx = trop-strat mass exchange (Tg/yr)

function dxdt = Box_Model_Eq1_Revised(t,x,Fx,M_T,M_S,a1,a2,s,b,tau)

a3 = s*exp(b*t);      % exponential anthropogenic source

dxdt = zeros(2,1);

dxdt(1) = ((a1 + a2 + 0*a3)/M_T)*10^9 - ((Fx/(M_T))*(x(1) - x(2)));
dxdt(2) = ((Fx/M_S)*(x(1) - x(2))) - ((M_T)*x(1)...
   + (M_S)*x(2))/(M_S*tau);

end
```

B.4. 2-box model, equation 2, for N_2O concentration.

```
% We are going to use the same model as Box_Model_Eq, but we already have
% solved for the initial conditions and found N2O_Ti and N2O_Si
%
% Use these values as starting points when adding in anthropogenic
% emissions starting at the year 1750 = t(0)

%
% x(1) = [N2O]_T or troposphere N2O concentration
% x(2) = [N2O]_S or stratosphere N2O concentration
% X_T = Ratio of air in troposphere over total(Tg)
% X_S = Ratio of air in stratosphere over total (Tg)
% a1 = natural ocean sources
% a2 = natural terrestrial sources
% b = anthropogenic growth rate constant
% Fx = trop-strat mass exchange (Tg/yr)

function dxdt = Box_Model_Eq2_Revised(t,x,Fx,M_T,M_S,a1,a2,s,b,tau)

a3 = s*exp(b*t);      % exponential anthropogenic source

dxdt = zeros(2,1);

dxdt(1) = ((a1 + a2 + a3)/M_T)*10^9 - ((Fx/M_T)*(x(1) - x(2)));
dxdt(2) = ((Fx/M_S)*(x(1) - x(2))) - ((M_T)*x(1)...
   + (M_S)*x(2))/(M_S*tau);

end
```

B.5. 2-box model for N_2O isotopic composition.

```
% Iso Box Model Solve
%
% We start by assuming Box_Model_Solve has been run and values for modelled
% N2O concentration have been found and fit decently to observations
%
% Now we want to solve for the isotopic composition
%
% From Park et al. 2012, the pre-industrial background deltas are:
% d15N_nat = 9.3;    (‰)
% d15Na_nat = 18.8;   (‰)
% d15Nb_nat = -0.6;   (‰)
% d15Nsp_nat = 19.4;   (‰)
% d18O_nat = 45.5;    (‰)
%
% If the model work correctly, these are the values we want to get when
% solved in steady-state
%
% To solve our equation, we need to assume the mean pre-industrial deltas
% of the natural ocean and terrestrial sources

d15N_ocean = 4.0;   % Sowers 2002 used 5.8, Park 2004 ranges +2 to +10
d15Na_ocean = 3.0;           % 2.7
d15Nb_ocean = 5.0;           % 5.3
d18O_ocean = 31.9;  % Sowers 2002 used 38.9, Park 2004 ranges +14 to +32

d15N_terr = -12.3;    % Sowers 2002 used -15, Park 2004 ranges -34 to +2
d15Na_terr = -8.1;         % -7.3
d15Nb_terr = -17.4;        % -17.0
d18O_terr = 31.9;   % Sowers 2002 used 23.5, Park 2004 ranges -4 to +18

% these are initially adjusted manually to fit the observed data when
% plotted, then Chi2_Fit is used to optimize the fit to CM data
d15N_anth = -15.3;      % -15.6 , -15.3 , -15.0
d15Na_anth = -12.2;     % -13.6 , -12.2 , -10.8
d15Nb_anth = -15.2;     % -16.8 , -15.2 , -13.6
d18O_anth = 33.9;       %  33.5 ,  33.9 ,  34.3

% Standard R values to convert R values to deltas
R18_VSMOW = 0.0020052;
R15_N2 = 0.0036765;

% equation for delta is d = (R/Rst - 1)*1000, so
R15N_ocean = ((d15N_ocean/1000)+1)*R15_N2;
R15Na_ocean = ((d15Na_ocean/1000)+1)*R15_N2;
R15Nb_ocean = ((d15Nb_ocean/1000)+1)*R15_N2;
R18O_ocean = ((d18O_ocean/1000)+1)*R18_VSMOW;

R15N_terr = ((d15N_terr/1000)+1)*R15_N2;
R15Na_terr = ((d15Na_terr/1000)+1)*R15_N2;
R15Nb_terr = ((d15Nb_terr/1000)+1)*R15_N2;
R18O_terr = ((d18O_terr/1000)+1)*R18_VSMOW;
```

```
R15N_anth = ((d15N_anth/1000)+1)*R15_N2;
R15Na_anth = ((d15Na_anth/1000)+1)*R15_N2;
R15Nb_anth = ((d15Nb_anth/1000)+1)*R15_N2;
R18O_anth = ((d18O_anth/1000)+1)*R18_VSMOW;

% we need the fractionation factor (alpha) for each species
alpha_15N = 0.9838;     % Rahn and Wahlen 2000 used 0.9855
                        % Rockmann used 0.9829
                        % table in Park 2004 has 0.9851
                        % Prokopiou 2017 used 0.9838
alpha_15Na = 0.9770;    % Rockmann et al. 2003 used 0.9787
                        % table in Park 2004 has 0.9775
                        % Prokopiou 2017 used 0.9770
alpha_15Nb = 0.9906;    % Rockmann et al. 2003 used 0.9871
                        % Park 2012 1-box solution works with 0.9929
                        % Prokopiou 2017 used 0.9906
alpha_18O = 0.9866;     % Rahn and Wahlen 2000 used 0.9871
                        % Rockmann used 0.986
                        % table in Park 2004 has 0.9867
                        % Prokopiou 2017 used 0.9866

% Delta Sink alpha values reported in Toyoda 2001
% alpha_15N = 0.9767;     % 0.9767 in Rockmann, others have 0.9806 - 0.9577
% alpha_15Na = 0.9591;    % 0.9643 in Rockmann, others have 0.9429 - 0.9743
% alpha_15Nb = 0.9845;    % 0.9891 in Rockmann, others have 0.9686 - 0.9925
% alpha_18O = 0.9754;     % 0.9827 in Rockmann, others have 0.9540 - 0.9871

% Now we have enough info to plug into our model and solve for steady-state

% Define concentrations in each box during pre-industrial period
N2O_T = N2O_Ti;
N2O_S = N2O_Si;

% First solve for d15N
% define R1, R2, R3, and alpha to their d15N values
R1 = R15N_ocean;
R2 = R15N_terr;
R3 = R15N_anth;
alpha = alpha_15N;

% set the dates to solve between 0 and 5000
tspan = (0:100:5000);

% set the initial R values of the troposphere and stratosphere
x0 = [0 0];

% solve system using ode23s
[t,x] = ode23s(@(t,x) Iso_BM_Eq1_Revised(t,x,Fx,N2O_T,N2O_S,M_T,M_S,a1,a2,s,b,...
   R1,R2,R3,tau,alpha),tspan,x0);

% values in x are R values, we need to convert to deltas
% x(:,1) = ((x(:,1)/R15_N2)-1)*1000;
% x(:,2) = ((x(:,2)/R15_N2)-1)*1000;

% plot figure
```

```
% figure
% plot(t(:,1),x(:,1),'k-');

% Now assign the last values in x as the pre-industrial background
R15N_Ti = x(end,1);
R15N_Si = x(end,2);

% Solving the system while including the anthropogenic source has to be
% done in a loop. This is because each year, the concentration is
% different. The array "concentration" contains the N2O_T (col 1) and N2O_S
% values (col 2) from 1750 to 2000, with each row representing 1 year.

% Create array for solved values to go in
d15N_T = zeros(251,2);  % troposphere d15N
d15N_S = zeros(251,2);  % stratosphere d15N

for i = 1:251
   d15N_T(i,1) = R15N_Ti;
   d15N_S(i,1) = R15N_Si;
end

tspan = (1:1:251);

x0 = [R15N_Ti R15N_Si];

% The solver doesn't like that the concentration N2O_T and N2O_S changes in
% time when it isn't in an equation format, so we will need to fit the data
% and use the fit as a means around this problem
% The matrix "concentration" contains the N2O_T and N2O_S values matching
% the year in the array "time" - 1750

year = [];
year(:,1) = time(1:1:end,1) - 1750;
f1 = fit(year(:,1),concentration(1:1:end,1),'poly4');    % N2O_T function
coef_1 = coeffvalues(f1);   % values are a, b, c, and d from exp2 fit
f2 = fit(year(:,1),concentration(1:1:end,2),'poly4');    % N2O_S function
coef_2 = coeffvalues(f2);   % values are a, b, c, and d from exp2 fit

% solve Iso_BM_Eq3 using ode23s
[t,x] = ode23s(@(t,x) Iso_BM_Eq3_Revised(t,x,Fx,coef_1,coef_2,M_T,M_S,a1,a2,s,b,...
   R1,R2,R3,tau,alpha),tspan,x0);

d15N_T(1:1:251,1) = x(1:1:end,1);
d15N_S(1:1:251,1) = x(1:1:end,2);

% values in d15N_ are R values, we need to convert to deltas
d15N_T(:,1) = ((d15N_T(:,1)/R15_N2)-1)*1000;
d15N_S(:,1) = ((d15N_S(:,1)/R15_N2)-1)*1000;

% plot figure 1750 to 2000
figure
plot(time(:,1),d15N_T(:,1),'k-');
hold on
plot(CM_d15N(:,1),CM_d15N(:,2),'c+');
```

```
% plot figure 1975 to 2000
% figure
plot(time(226:1:251,1),d15N_T(226:1:251,1),'k-');
hold on
% plot(CM_d15N(:,1),CM_d15N(:,2),'c+');

%%
% Now repeat the process for d15Na
% define R1, R2, R3, and alpha to their d15Na values
R1 = R15Na_ocean;
R2 = R15Na_terr;
R3 = R15Na_anth;
alpha = alpha_15Na;

% set the dates to solve between 0 and 5000
tspan = (0:100:5000);

% set the initial R values of the troposphere and stratosphere
x0 = [0 0];

% solve system using ode23s
[t,x] = ode23s(@(t,x) Iso_BM_Eq1_Revised(t,x,Fx,N2O_T,N2O_S,M_T,M_S,a1,a2,s,b,...
   R1,R2,R3,tau,alpha),tspan,x0);

% values in x are R values, we need to convert to deltas
% x(:,1) = ((x(:,1)/R15_N2)-1)*1000;
% x(:,2) = ((x(:,2)/R15_N2)-1)*1000;

% plot figure
% figure
% plot(t(:,1),x(:,1),'k-');

% Now assign the last values in x as the pre-industrial background
R15Na_Ti = x(end,1);
R15Na_Si = x(end,2);

% Solving the system while including the anthropogenic source has to be
% done in a loop. This is because each year, the concentration is
% different. The array "concentration" contains the N2O_T (col 1) and N2O_S
% values (col 2) from 1750 to 2000, with each row representing 1 year.

% Create array for solved values to go in
d15Na_T = zeros(251,2);  % troposphere d15Na
d15Na_S = zeros(251,2);  % stratosphere d15Na

for i = 1:251
   d15Na_T(i,1) = R15Na_Ti;
   d15Na_S(i,1) = R15Na_Si;
end

tspan = (0:1:250);

x0 = [R15Na_Ti R15Na_Si];

% solve Iso_BM_Eq3 using ode23s
```

```
[t,x] = ode23s(@(t,x) Iso_BM_Eq3_Revised(t,x,Fx,coef_1,coef_2,M_T,M_S,a1,a2,s,b,...
   R1,R2,R3,tau,alpha),tspan,x0);

d15Na_T(1:1:251,1) = x(1:1:end,1);
d15Na_S(1:1:251,1) = x(1:1:end,2);

% values in d15N_ are R values, we need to convert to deltas
d15Na_T(:,1) = ((d15Na_T(:,1)/R15_N2)-1)*1000;
d15Na_S(:,1) = ((d15Na_S(:,1)/R15_N2)-1)*1000;

% plot figure 1750 to 2000
figure
plot(time(:,1),d15Na_T(:,1),'k-');
hold on
plot(CM_d15Na(:,1),CM_d15Na(:,2),'c+');

% plot figure 1975 to 2000
% figure
% plot(time(226:1:251,1),d15Na_T(226:1:251,1),'k-');
% hold on
% plot(CM_d15Na(:,1),CM_d15Na(:,2),'c+');

%%
% Repeat for d15Nb

% define R1, R2, R3, and alpha to their d15Nb values
R1 = R15Nb_ocean;
R2 = R15Nb_terr;
R3 = R15Nb_anth;
alpha = alpha_15Nb;

% set the dates to solve between 0 and 5000
tspan = (0:100:5000);

% set the initial R values of the troposphere and stratosphere
x0 = [0 0];

% solve system using ode23s
[t,x] = ode23s(@(t,x) Iso_BM_Eq1_Revised(t,x,Fx,N2O_T,N2O_S,M_T,M_S,a1,a2,s,b,...
   R1,R2,R3,tau,alpha),tspan,x0);

% values in x are R values, we need to convert to deltas
% x(:,1) = ((x(:,1)/R15_N2)-1)*1000;
% x(:,2) = ((x(:,2)/R15_N2)-1)*1000;

% plot figure
% figure
% plot(t(:,1),x(:,1),'k-');

% Now assign the last values in x as the pre-industrial background
R15Nb_Ti = x(end,1);
R15Nb_Si = x(end,2);

% Solving the system while including the anthropogenic source has to be
% done in a loop. This is because each year, the concentration is
```

```
% different. The array "concentration" contains the N2O_T (col 1) and N2O_S
% values (col 2) from 1750 to 2000, with each row representing 1 year.

% Create array for solved values to go in
d15Nb_T = zeros(251,2);  % troposphere d15Nb
d15Nb_S = zeros(251,2);  % stratosphere d15Nb

for i = 1:1
   d15Nb_T(i,1) = R15Nb_Ti;
   d15Nb_S(i,1) = R15Nb_Si;
end

tspan = (1:1:251);

x0 = [R15Nb_Ti R15Nb_Si];

% solve Iso_BM_Eq3 using ode23s
[t,x] = ode23s(@(t,x) Iso_BM_Eq3_Revised(t,x,Fx,coef_1,coef_2,M_T,M_S,a1,a2,s,b,...
   R1,R2,R3,tau,alpha),tspan,x0);

d15Nb_T(1:1:251,1) = x(1:1:end,1);
d15Nb_S(1:1:251,1) = x(1:1:end,2);

% values in d15N_ are R values, we need to convert to deltas
d15Nb_T(:,1) = ((d15Nb_T(:,1)/R15_N2)-1)*1000;
d15Nb_S(:,1) = ((d15Nb_S(:,1)/R15_N2)-1)*1000;

% plot figure 1750 to 2000
figure
plot(time(:,1),d15Nb_T(:,1),'k-');
hold on
plot(CM_d15Nb(:,1),CM_d15Nb(:,2),'c+');

% plot figure 1975 to 2000
% figure
% plot(time(226:1:251,1),d15Nb_T(226:1:251,1),'k-');
% hold on
% plot(CM_d15Nb(:,1),CM_d15Nb(:,2),'c+');

%%
% Repeat for d18O

% define R1, R2, R3, and alpha to their d18O values
R1 = R18O_ocean;
R2 = R18O_terr;
R3 = R18O_anth;
alpha = alpha_18O;

% set the dates to solve between 0 and 5000
tspan = (0:100:5000);

% set the initial R values of the troposphere and stratosphere
x0 = [0 0];

% solve system using ode23s
```

```
[t,x] = ode23s(@(t,x) Iso_BM_Eq1_Revised(t,x,Fx,N2O_T,N2O_S,M_T,M_S,a1,a2,s,b,...
   R1,R2,R3,tau,alpha),tspan,x0);

% values in x are R values, we need to convert to deltas
% x(:,1) = ((x(:,1)/R18_VSMOW)-1)*1000;
% x(:,2) = ((x(:,2)/R18_VSMOW)-1)*1000;

% plot figure
% figure
% plot(t(:,1),x(:,1),'k-');

% Now assign the last values in x as the pre-industrial background
R18O_Ti = x(end,1);
R18O_Si = x(end,2);

% Solving the system while including the anthropogenic source has to be
% done in a loop. This is because each year, the concentration is
% different. The array "concentration" contains the N2O_T (col 1) and N2O_S
% values (col 2) from 1750 to 2000, with each row representing 1 year.

% Create array for solved values to go in
d18O_T = zeros(251,2);  % troposphere d18O
d18O_S = zeros(251,2);  % stratosphere d18O

for i = 1:1
   d18O_T(i,1) = R18O_Ti;
   d18O_S(i,1) = R18O_Si;
end

tspan = (1:1:251);

x0 = [R18O_Ti R18O_Si];

% solve Iso_BM_Eq3 using ode23s
[t,x] = ode23s(@(t,x) Iso_BM_Eq3_Revised(t,x,Fx,coef_1,coef_2,M_T,M_S,a1,a2,s,b,...
   R1,R2,R3,tau,alpha),tspan,x0);

d18O_T(1:1:251,1) = x(1:1:end,1);
d18O_S(1:1:251,1) = x(1:1:end,2);

% values in d15N_ are R values, we need to convert to deltas
d18O_T(:,1) = ((d18O_T(:,1)/R18_VSMOW)-1)*1000;
d18O_S(:,1) = ((d18O_S(:,1)/R18_VSMOW)-1)*1000;

% plot figure 1750 to 2000
figure
plot(time(:,1),d18O_T(:,1),'k-');
hold on
plot(CM_d18O(:,1),CM_d18O(:,2),'c+');

% plot figure 1975 to 2000
figure
plot(time(226:1:251,1),d18O_T(226:1:251,1),'k-');
hold on
plot(CM_d18O(:,1),CM_d18O(:,2),'c+');
```

B.6. 2-box model, equation 1 for N_2O isotopic composition

```
% Start with our 2-Equations
% x(1) = R_T or troposphere isotope ratio
% x(2) = R_S or stratosphere isotope ratio
% N2O_T = troposphere N2O concentration (ppb)
% N2O_S = stratosphere N2O concentration (ppb)
% X_T = Ratio of air in troposphere over total
% X_S = Ratio of air in stratosphere over total
% a1 = natural ocean source (ppb/yr)
% a2 = natural terrestrial source (ppb/yr)
% s = anthropogenic exponential source parameter
% b = anthropogenic exponential source parameter
% R1 = natural ocean source isotope ratio
% R2 = natural terrestrial source isotope ratio
% R3 = anthropogenic source isotope ratio
% Fx = trop-strat mass exchange (Tg/yr)
% conv = Tg/yr to ppb/yr conversion for N2O
% tau = atmospheric lifetime of N2O (yr)
% alpha = fractionation factor for specific isotopomer
   % this is called Delta Sink in Sowers and they use values reported from
   % Toyoda 2001 and Rockmann 2001

% This equation is for solved for steady-state, so 0*anthropogenic source

function dxdt = Iso_BM_Eq1_Revised(t,x,Fx,N2O_T,N2O_S,M_T,M_S,a1,a2,s,b,...
   R1,R2,R3,tau,alpha)

a3 = s*exp(b*t);      % exponential anthropogenic source

dxdt = zeros(2,1);

dxdt(1) = ((a1/M_T)/N2O_T)*(R1 - x(1))*10^9 + ...
   ((a2/M_T)/N2O_T)*(R2 - x(1))*10^9 + ...
   0*((a3/M_T)*N2O_T)*(R3 - x(1))*10^9 + ...
   (Fx/M_T)*(N2O_S/N2O_T)*(x(2)-x(1));

dxdt(2) = (Fx/M_S)*(N2O_T/N2O_S)*(x(1) - x(2)) + ...
   (x(2)/N2O_S)*(1/(M_S*tau))*(M_T*N2O_T + M_S*N2O_S) - ...
   (alpha/(tau*N2O_S*M_S))*(M_T*N2O_T*x(1) + M_S*N2O_S*x(2));

end
```

B.7. 2-box model, equation 3 for N_2O isotopic composition

```
% Start with our 2-Equations
% x(1) = R_T or troposphere isotope ratio
% x(2) = R_S or stratosphere isotope ratio
% N2O_T = troposphere N2O concentration (ppb)
% N2O_S = stratosphere N2O concentration (ppb)
% X_T = Ratio of air in troposphere over total
% X_S = Ratio of air in stratosphere over total
% a1 = natural ocean source (ppb/yr)
% a2 = natural terrestrial source (ppb/yr)
% s = anthropogenic exponential source parameter
% b = anthropogenic exponential source parameter
% R1 = natural ocean source isotope ratio
% R2 = natural terrestrial source isotope ratio
% R3 = anthropogenic source isotope ratio
% Fx = trop-strat mass exchange (Tg/yr)
% conv = Tg/yr to ppb/yr conversion for N2O
% tau = atmospheric lifetime of N2O (yr)
% alpha = fractionation factor for specific isotopomer
   % this is called Delta Sink in Sowers and they use values reported from
   % Toyoda 2001 and Rockmann 2001

% This equation is for solved including the anthropogenic source

% We need to include the changing N2O_T and N2O_S concentration this time
% To do this we want to use the coefficients found by fitting the data to a
% 2 exponential fit where N2O = a*exp(b*t) + c*exp(d*t)

function dxdt = Iso_BM_Eq3_Revised(t,x,Fx,coef_1,coef_2,M_T,M_S,a1,a2,s,b,...
   R1,R2,R3,tau,alpha)

a3 = s*exp(b*t);      % exponential anthropogenic source

% N2O_T = coef_1(1,1)*exp(coef_1(1,2)*t) + coef_1(1,3)*exp(coef_1(1,4));
% N2O_S = coef_2(1,1)*exp(coef_2(1,2)*t) + coef_2(1,3)*exp(coef_2(1,4));

N2O_T = coef_1(1,1)*t^4 + coef_1(1,2)*t^3 + coef_1(1,3)*t^2 + ...
   coef_1(1,4)*t + coef_1(1,5);
N2O_S = coef_2(1,1)*t^4 + coef_2(1,2)*t^3 + coef_2(1,3)*t^2 + ...
   coef_2(1,4)*t + coef_2(1,5);

dxdt = zeros(2,1);

dxdt(1) = ((a1/M_T)/N2O_T)*(R1 - x(1))*10^9 + ...
   ((a2/M_T)/N2O_T)*(R2 - x(1))*10^9 + ...
   ((a3/M_T)/N2O_T)*(R3 - x(1))*10^9 + ...
   (Fx/M_T)*(N2O_S/N2O_T)*(x(2)-x(1));

dxdt(2) = (Fx/M_S)*(N2O_T/N2O_S)*(x(1) - x(2)) + ...
   (x(2)/N2O_S)*(1/(M_S*tau))*(M_T*N2O_T + M_S*N2O_S) - ...
   (alpha/(tau*N2O_S*M_S))*(M_T*N2O_T*x(1) + M_S*N2O_S*x(2));

end
```